

NASA/CR-97- 206678

FINAL
IN-08-CR
7CIT
045651

DEPARTMENT OF AEROSPACE ENGINEERING
COLLEGE OF ENGINEERING AND TECHNOLOGY
OLD DOMINION UNIVERSITY
NORFOLK, VIRGINIA 23529

**AEROELASTIC, CFD, AND DYNAMIC COMPUTATION AND
OPTIMIZATION FOR BUFFET AND FLUTTER APPLICATION**

By
Dr. Osama A. Kandil, Principal Investigator

Final Report
For the period of December 1, 1996 - November 30, 1997

Prepared for
National Aeronautics and Space Administration
Langley Research Center
Attn.: Joseph Murray, Grants Officer
Mail Stop 126
Hampton, VA 23681-0001

Under
Research Grant NAG-1-648
Dr. R. M. Bennett, Technical Monitor
ODURF #164069

DEPARTMENT OF AEROSPACE ENGINEERING
COLLEGE OF ENGINEERING AND TECHNOLOGY
OLD DOMINION UNIVERSITY
NORFOLK, VIRGINIA 23529

**AEROELASTIC, CFD, AND DYNAMIC COMPUTATION AND
OPTIMIZATION FOR BUFFET AND FLUTTER APPLICATION**

By
Dr. Osama A. Kandil, Principal Investigator

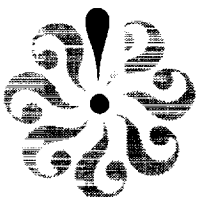
Final Report
For the period of December 1, 1996 - November 30, 1997

Prepared for
National Aeronautics and Space Administration
Langley Research Center
Attn.: Joseph Murray, Grants Officer
Mail Stop 126
Hampton, VA 23681-0001

Under
Research Grant NAG-1-648
Dr. R. M. Bennett, Technical Monitor
ODURF #164069

Submitted by
Old Dominion University Research Foundation
Norfolk, VA 23508

December 1997





**AEROELASTIC, CFD AND DYNAMICS COMPUTATION AND
OPTIMIZATION FOR BUFFET AND FLUTTER APPLICATIONS**

GRANT NO. NAG-1-648

Osama A. Kandil

Aerospace Engineering Department

Old Dominion University, Norfolk, VA 23529-0247

Accomplishments

In the period of December 1, 1996 to November 30, 1997, the Principal Investigator (PI) along with the assistance of two Ph.D. students have achieved the following accomplishments under this grant:

I. Publications

- I.1 Kandil, O. A. and Sheta, E. F., "Coupled and Uncoupled Bending-Torsion Responses of Twin-Tail Buffet," Accepted for publication in Journal of Fluids and Structures, Academic Press, to appear 1998.
- I.2 Kandil, O. A. and Sheta, E. F., "Coupled and Uncoupled Bending Torsion Responses of Twin Tail Buffet," Fourth International Symposium on Fluid/Structure, Aeroelasticity and Flow Induced Vibrations and Noise, ASME 97-129, 1997 ASME International Engineering Congress and Exposition, Dallas, Texas, November 1997, AD-Vol . 53-3, pp. 1-12 (A copy is attached).
- I.3 Kandil, O. A., Liu, C. H. and Sheta, E. F., "Effects of Coupled and Uncoupled Mode Responses on Tail Buffet Over a Wide Range of Angles of Attack," IUTAM-Symposium on Slender Vortex Dynamic, Aerodynamics Institute, Aachen, Germany, August 31-September 4, 1997. Invited keynote paper.
- I.4 Kandil, O. A., and Abdelhamid, Y. A., "Computation and Validation of Delta Wing Pitching up to 90° Amplitude," AIAA 97-3573-CP, AIAA Atmospheric Flight Mechanics Conference, New Orleans, LA, August 11-13, 1997, pp. 221-231.
- I.5 Kandil, O. A., Sheta, E. F., Massey, S. J., "Fluid/Structure Twin Tail Buffet Responses Over a Wide Range of Angles of Attack," AIAA 97-2261, AIAA Applied Aerodynamics Conference, Atlanta, GA, June 23-25, 1997, pp. 373-386. (A copy is attached).
- I.6 Kandil, O. A. and Menzies, M. A., "Effective Control of computationally Simulated Wing Rock in Subsonic Flow," AIAA 97-0831, AIAA 35th ASM, Reno, Nevada, January 1997.
- I.7 Kandil, O. A., "Recent Advances in Multidisciplinary Aeronautical Problems of Fluid/Structures/Dynamics Interaction," International Seminar Series II Proceedings, Institute of Aeronautics and Applied Mechanics, Warsaw University of Technology, November 1996. Invited paper, pp. 15-34. (A copy is attached).

II. Papers Accepted for Conference Presentation

- II.1. Essam, E. F. and Kandil, O. A., "Effect of Configuration Pitching Motion on Twin Tail Buffet Response," AIAA 98-0520, AIAA 36th ASM, Reno, NV, January 1998.
- II.2. Abdelhamid, Y. A. and Kandil, O. A., "Effect of Reduced Frequency on Super-Manuever Delta Wing," AIAA 98-0414, AIAA 36th ASM, Reno, NV, January 1998.
- II.3. Massey, S. J. and Kandil, O. A., "Effect of Apex Flap Deflection on Vertical Tail Buffet," AIAA 98-0762, AIAA 36th ASM Reno, NV, January 1998.

III. Proposal Submitted for CRAY-C-90 Usage

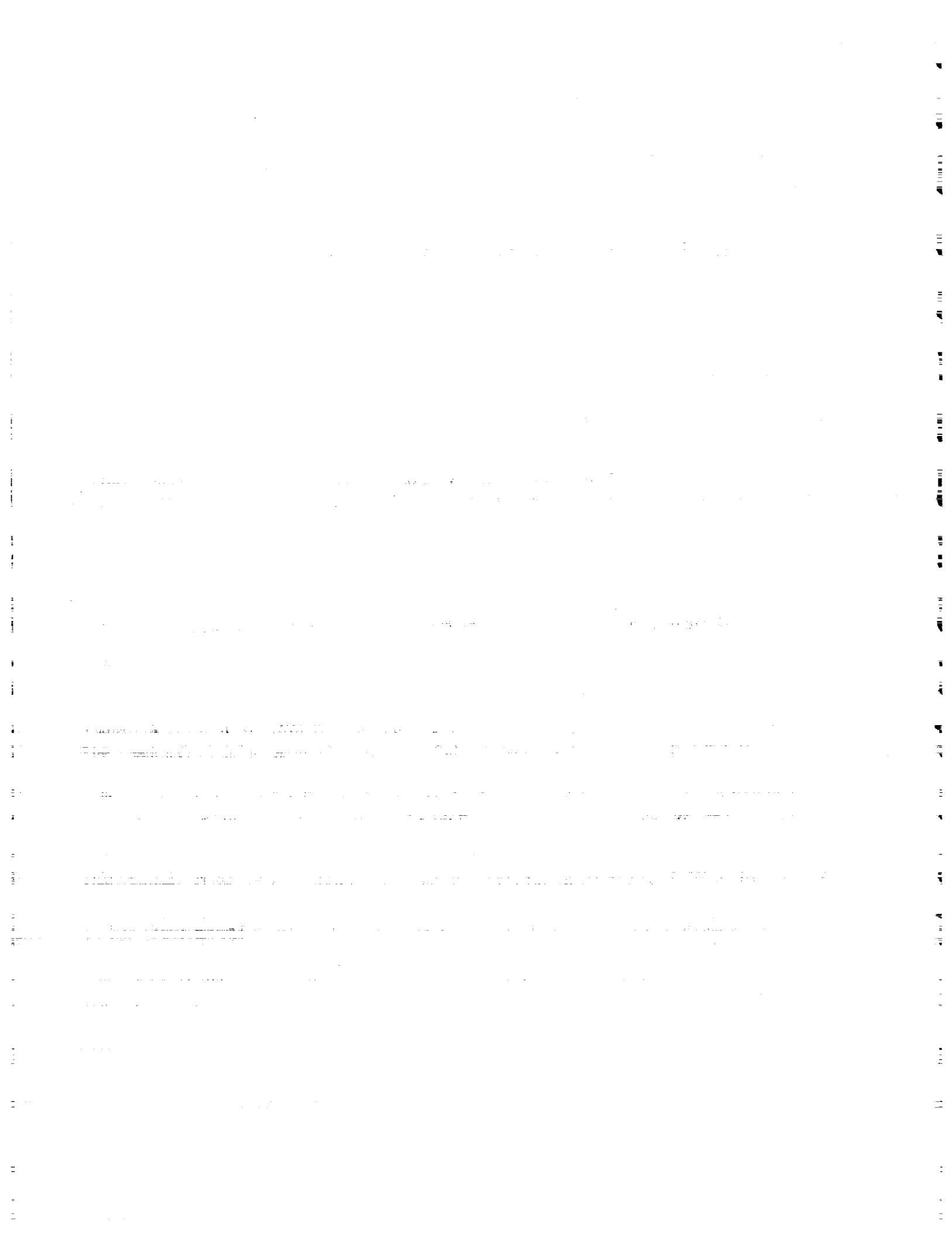
A proposal has been submitted for usage of the National Aerodynamic Simulation (NAS) Facilities at NASA Ames Research Center, CA, on May 1, 1997. A total of 200 hrs. of C-90 CPU time has been requested.

A technical summary has also been submitted to NAS on November 26, 1997. It summarized the achievements, goals, approach and recent results of effects of coupled and uncoupled bending and torsion buffet responses of a typical twin-tail configuration. Comparison of these results is shown with the available experimental data.

IV. Graduate Students

Two Ph.D. students have been assisting the P.I. to carry out the tasks of this grant and write their Ph.D. dissertations. The status of the students is given below:

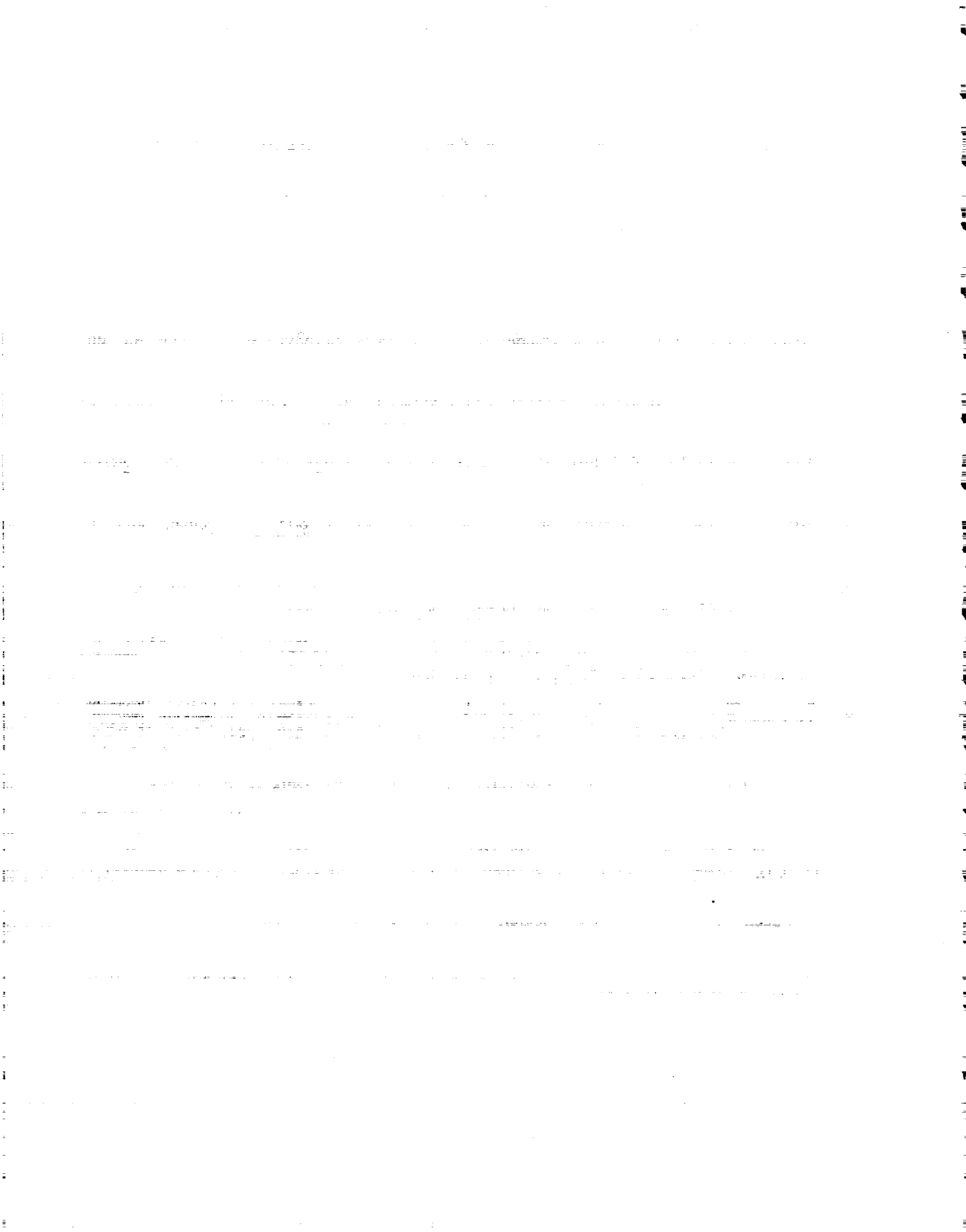
- VI. Mr. Steven J. Massey (U.S. Citizen): He has been working on his Ph.D. degree since May 1994, and has been supported under this grant and a fellowship from the Aerospace Engineering Department. He successfully defended his Ph.D. dissertation in October, 1997 and is graduating this semester. His Ph.D. dissertation is titled, "Development of A Coupled Fluid/Structure Aeroelastic Solver with Applications to Vortex Breakdown Induced Twin Tail Buffet." Drs. Woodrow Whitlow, Jr. and Robert Bennett served on his Ph.D. committee. A copy of his dissertation abstract is attached.
- VII. Mr. Mark W. Flanagan (U.S. Citizen): He has been working on his Ph.D. degree since January 1994. He has been supported under a fellowship from the AE Dept. and work at Dynamic Engineering Inc. Currently, he is a Ph.D. candidate (since Spring 1996) and he is expected to finish his Ph.D. degree in December 1998. His Ph.D. dissertation focuses on simulation and optimization control of tail buffet in supersonic internal vortex breakdown flows in a configured duct. Drs. Woodrow Whitlow, Jr. and Robert Bennett are serving on his Ph.D. committee.



A third Student, Mr. Essam Sheta, who is supported by the Aerospace Engineering Department, is also writing his Ph.D. Dissertation on Flow Turbulence and Control Effects on Coupled and Uncoupled Bending Torsion Modes of Twin Tail Response. He is expected to finish his Ph.D. dissertation in May 1998.

V. Technical Group Participations and Conference Presentations: The past year (12/1/96–11/30/97) was a very productive one for technical group participations and conference presentations by the P.I. and his students. These are listed below:

1. "Coupled and Uncoupled Bending torsion Responses of Twin Tail Buffet," ASME 97-129, 1997 ASME International Engineering Congress and Exposition, Dallas, Texas, November 1997.
2. "Effects of Coupled and Uncoupled Modes on Tail Buffet Over a Wide Range of Angles of Attack," IUTAM Colloquim on Slender Vortex Dynamics, Aerodynamics Institute, Aachen, Germany, August 31 — September 3, 1997. (Invited)
3. "Computation and Validation of Delta wing Pitching up to 90° Amplitude," AIAA Atmospheric Flight Mechanics Conference, New Orleans, LA, August 11–13, 1997.
4. "Fluid/Structure Twin Tail Buffet Responses Over a Wide Range of Angles of Attack," AIAA Applied Aerodynamics Conference, Atlanta, GA, June 23–25, 1997.
5. "Effect of Turbulence on Twin Tail-Buffer Response," VCES Spring Conference, Hampton, VA, June 10, 1997.
6. "Computation and Validation of Delta Wing Pitching Response for very high Angles of Attack," VCES Spring Conference, Hampton, VA, June 10, 1997.
7. "Effective Control of computationally Simulated Wing Rock in Subsonic Flow," AIAA 35th Aerospace Sciences Meeting, Reno, Nevada, January 9–12, 1997.
8. General Chairman and Organizer of AIAA Applied Aerodynamics (APA) Program, Aerospace Sciences Meeting, Reno, NV, January 1998. Two new special sessions which are related to the current grant work have been introduced in the APA program for the first time. These are Aero/Structures Interaction and Flow control using oscillating jets.
9. The P.I. was invited by the Ohio Aerospace Institute to serve on the National Committee of Fixed Wing Vehicle Initiative for Aerodynamics, Structures and Control Integration (ASCI), initiated by Industry/Government/Academia Technical Leaders, also a member of the Unsteady Flow Team and Academia Team, May-July 1997. A major report has been produced for the next 15 year research needs in this important area.
10. The P.I. is planning to participate in the coming workshop at NASA Langley Research on the Nonlinear Aeroservoelasticity, organized by the Branch in the period of January 20–22, 1998.



COUPLED AND UNCOUPLED BENDING-TORSION RESPONSES OF TWIN-TAIL BUFFET

**Osama A. Kandil and Essam F. Sheta
Aerospace Engineering Department
Old Dominion University, Norfolk, VA 23529**

**FSI, AE & FIV+N Symposium
1997 ASME International Engineering
Congress and Exposition
November 16-19, 1997, Dallas, TX**

COUPLED AND UNCOUPLED BENDING-TORSION RESPONSES OF TWIN-TAIL BUFFET

Osama A. Kandil and Essam F. Sheta

Aerospace Engineering Department
Old Dominion University
Norfolk, VA 23529, USA

ABSTRACT

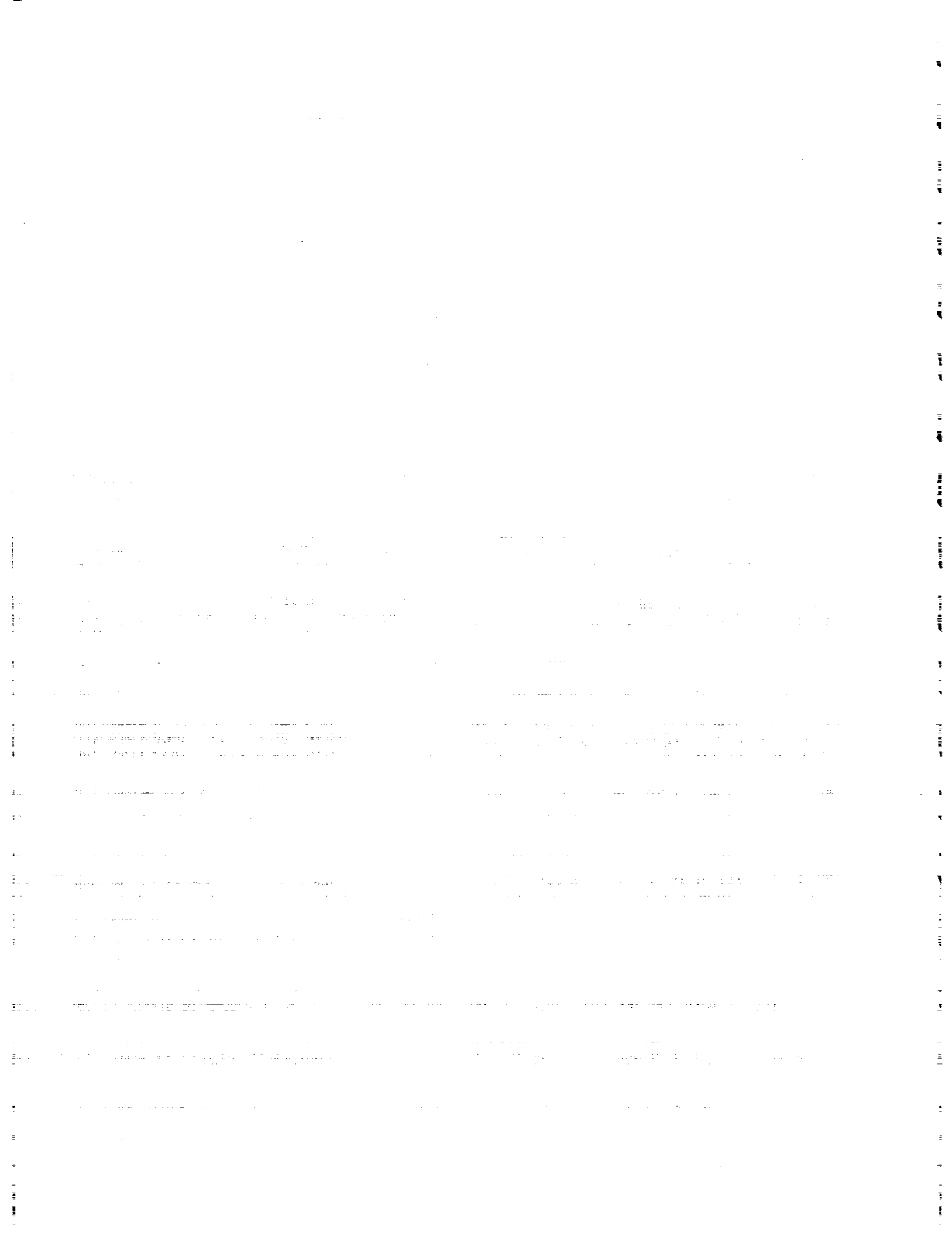
The effect of coupled and uncoupled bending and torsion modes on flexible twin-tail buffet is considered. This multidisciplinary problem is investigated using three sets of equations on a multi-block grid structure. The first set is the unsteady, compressible, full Navier-Stokes equations which are used for obtaining the flow-field vector and the aerodynamic loads on the twin tails. The second set is the coupled aeroelastic equations which are used for obtaining the bending and torsional deflections of the twin tails. The third set is the grid-displacement equations which are used for updating the grid coordinates due to the tail deflections. The configuration is pitched at 30° angle of attack and the freestream Mach number and Reynolds number are 0.3 and 1.25 million, respectively. Keeping the twin tails as rigid surfaces, the problem is solved for the initial flow conditions. Next, the problem is solved for the flexible twin tails responses due to the unsteady loads produced by the vortex breakdown flow of the delta-wing leading-edge vortex cores. The configuration is investigated for the effect of coupled and uncoupled bending and torsion modes using two different separation distances of the twin-tail; the inboard and the outboard positions.

1 INTRODUCTION

In order to maximize the effectiveness of the fighter aircraft that operate well beyond the buffet onset boundary, the design of the new generation of fighter aircraft should account for both high maneuver capabilities and the aeroelastic buffet characteristics at high and wide range of angles of attack. The maneuver capabilities are achieved, for example in the F/A-18 fighter, through the

combination of the leading-edge extension (LEX) with a delta wing and the use of vertical tails. The LEX maintains lift at high angles of attack by generating a pair of vortices that trail aft over the top of the aircraft. The vortex entrains air over the vertical tails to maintain stability of the aircraft. At some flight conditions, the vortices emanating from the highly-swept LEX of the delta wing breakdown before reaching the vertical tails which get bathed in a wake of unsteady highly-turbulent, swirling flow. The vortex-breakdown flow produces unsteady, unbalanced loads on the vertical tails and causes a peak in the pressure spectrum that may be tuned to different structural modes depending on the angle of attack and dynamic pressure. This in turn produces severe buffet on the tails and has led to their premature fatigue failure. If the power spectrum of the turbulence is accurately predicted, the intensity of the buffeting motion can be computed and the structural components of the aircraft can be designed accordingly.

Experimental investigation of the vertical tail buffet of the F/A-18 models have been conducted by several investigators such as Sellers, et al. (1988), Erickson, et al. (1989), Wentz (1987), Lee and Brown (1990), and Cole, et al. (1990). These experiments showed that the vortex produced by the LEX of the wing breaks down ahead of the vertical tails at angles of attack of 25° and higher producing unsteady loads on the vertical tails, and the buffet response occurs in the first bending mode, increases with increasing dynamic pressure and is larger at $M = 0.3$ than that at higher Mach numbers. Bean and Lee (1994) showed that buffeting in the torsional mode occurred at a lower angle of attack and at larger lev-



els compared to the fundamental bending mode. An extensive experimental investigation has been conducted to study vortex-tail interaction on a 76° sharp-edged delta wing with vertical twin-tail configuration by Washburn, Jenkins and Ferman (1993). The vertical tails were placed at nine locations behind the wing. The experimental data showed that the aerodynamic loads are more sensitive to the chordwise tail location than its spanwise location. As the tails were moved laterally toward the vortex core, the buffeting response and excitation were reduced.

Kandil, Kandil and Massey (1993) presented the first successful computational simulation of the vertical tail buffet using a delta wing-single flexible vertical tail configuration. The tail was allowed to oscillate in bending modes. Unsteady vortex breakdown of leading-edge vortex cores was captured, and unsteady pressure forces were obtained on the tail. Later on, Kandil, et al. (1994-1995) allowed the vertical tail to oscillate in both bending and torsional modes. The total deflections and frequencies of deflections and loads of the coupled bending-torsion case were found to be one order of magnitude higher than those of the bending case only. Also, it has been shown that the tail oscillations change the vortex breakdown locations and the unsteady aerodynamic loads on the wing and tail.

The buffet responses of twin-tail model has been studied by Kandil, Sheta and Liu (1996). The twin tails were considered at $\alpha = 30^\circ$ and for three different spanwise positions of the twin tails. A multi-block grid structure was used to solve the problem. The loads, deflections, frequencies and root bending moments were reduced as the twin tails moved laterally toward the vortex core. The outboard position of the tails produced the least of these responses. In a recent paper by Kandil, Sheta and Massey (1997), the buffet response of twin-tail model in turbulent flow was considered at a wide range of angles of attack. The computational results were in good quantitative agreement with the experimental data of Washburn, et al (1993).

In this paper, we consider the effect of coupled and uncoupled bending and torsion modes on the flexible twin-tail buffet response for two different spanwise separation distance of the twin-tail; the inboard position (33% wing span) and the outboard position (78% wing span).

2 FORMULATION

The formulation consists of three sets of governing equations along with certain initial and boundary conditions. The first set is the un-

steady, compressible, Reynolds-averaged Navier-Stokes equations. The second set consists of the aeroelastic equations for coupled bending and torsional modes. For uncoupled bending-torsion modes, x_θ is set equals to zero in Eqs (4) and (5). The third set consists of equations for deforming the grid according to the twin tail deflections. Next, the governing equations of each set along with the initial and boundary conditions are given.

2.1 Fluid-Flow Equations:

The conservative form of the dimensionless, unsteady, compressible, full Navier-Stokes equations in terms of time-dependent, body-conformed coordinates ξ^1, ξ^2 and ξ^3 is given by

$$\frac{\partial \bar{Q}}{\partial t} + \frac{\partial \bar{E}_m}{\partial \xi^m} - \frac{\partial (\bar{E}_v)_s}{\partial \xi^s} = 0; m = 1-3, s = 1-3 \quad (1)$$

where

$$\xi^m = \xi^m(x_1, x_2, x_3, t) \quad (2)$$

$$\bar{Q} = \frac{1}{J}[\rho, \rho u_1, \rho u_2, \rho u_3, \rho e]^t, \quad (3)$$

\bar{E}_m and $(\bar{E}_v)_s$ are the ξ^m -inviscid flux and ξ^s -viscous and heat conduction flux, respectively. Details of these fluxes are given by Kandil, Kandil and Massey (1993).

2.2 Aeroelastic Equations:

The dimensionless, linearized governing equations for the coupled bending and torsional vibrations of a vertical tail that is treated as a cantilevered beam are considered. The tail bending and torsional deflections occur about an elastic axis that is displaced from the inertial axis. These equations for the bending deflection, w , and the twist angle, θ , are given by

$$\begin{aligned} \frac{\partial^2}{\partial z^2} \left[EI(z) \frac{\partial^2 w}{\partial z^2}(z, t) \right] + m(z) \frac{\partial^2 w}{\partial t^2}(z, t) \\ + m(z) x_\theta(z) \frac{\partial^2 \theta}{\partial t^2}(z, t) = N(z, t) \end{aligned} \quad (4)$$

$$\begin{aligned} \frac{\partial}{\partial z} \left[GJ(z) \frac{\partial \theta}{\partial z} \right] - m(z) x_\theta(z) \frac{\partial^2 w}{\partial t^2}(z, t) \\ - I_\theta(z) \frac{\partial^2 \theta}{\partial t^2}(z, t) = -M_t(z, t) \end{aligned} \quad (5)$$

where z is the vertical distance from the fixed support along the tail length, l_t , EI and GJ

the bending and torsional stiffness of the tail section, m the mass per unit length, I_θ the mass-moment of inertia per unit length about the elastic axis, N the normal force per unit length, M_t the twisting moment per unit length and x_θ the distance between the elastic axis and inertia axis. When $x_\theta = 0.0$ the bending and torsion modes are dynamically decoupled. The characteristic parameters for the dimensionless equations are c^* , a_∞^* , ρ_∞^* and c^*/a_∞^* for the length, speed, density and time; where c^* is the delta wing root-chord length, a_∞^* the freestream speed of sound and ρ_∞^* the freestream air density. The details of the solution method are given in Kandil, Sheta and Massey (1997).

2.3 Grid Displacement Equations:

Once w and θ are obtained at the $n + 1$ time step, the new grid coordinates are obtained using simple interpolation equations. In these equations, the twin tail bending displacements, $w_{i,j,k}^{n+1}$, and their displacement through the torsion angle, $\theta_{i,j,k}^{n+1}$ are interpolated through cosine functions.

2.4 Boundary and Initial Conditions:

Boundary conditions consist of conditions for the fluid flow and conditions for the aeroelastic bending and torsional deflections of the twin tail. For the fluid flow, the Riemann-invariant boundary conditions are enforced at the inflow and outflow boundaries of the computational domain. At the plane of geometric symmetry, periodic boundary conditions are specified. On the wing surface, the no-slip and no-penetration conditions are enforced and $\frac{\partial p}{\partial n} = 0$. On the tail surface, the no-slip and no-penetration conditions for the relative velocity components are enforced (points on the tail surface are moving). The normal pressure gradient is no longer equal to zero due to the acceleration of the grid points on the tail surface. This equation becomes $\frac{\partial p}{\partial n} = -\rho \bar{a}_t \cdot \hat{n}$, where \bar{a}_t is the acceleration of a point on the tail and \hat{n} is the unit normal.

The initial conditions of the fluid flow correspond to the freestream conditions with no-slip and no-penetration conditions on the wing and tail. For the aeroelastic deflections of the tail, the initial conditions for any point on the tail are that the displacement and velocity are zero, $w(z, 0) = 0$, $\frac{\partial w}{\partial t}(z, 0) = 0$, $\theta(z, 0) = 0$ and $\frac{\partial \theta}{\partial t}(z, 0) = 0$.

3 METHOD OF SOLUTION

The first step is to solve for the fluid flow problem using the vortex-breakdown conditions and keeping the tail as a rigid beam. Navier-Stokes equations are solved using the implicit, flux-difference splitting finite-volume scheme. The grid speed $\frac{\partial \xi^m}{\partial t}$ is set equal to zero in this step. This step provides the flow field solution along with the pressure differences across the tails. The pressure differences are used to generate the normal force and twisting moment per unit length of each tail. Next, the aeroelastic equations are used to obtain the twin tail deflections, $w_{i,j,k}$ and $\theta_{i,j,k}$. The grid displacement equations are then used to compute the new grid coordinates. The metric coefficient of the coordinate Jacobian matrix are updated as well as the grid speed, $\frac{\partial \xi^m}{\partial t}$. This computational cycle is repeated every time step.

4 COMPUTATIONAL APPLICATIONS AND DISCUSSION

4.1 Twin Tail-Delta Wing Configuration:

The twin tail-delta wing configuration consists of a 76°-swept back, sharp-edged delta wing (aspect ratio of one) and dynamically scaled flexible twin tails similar to those used by Washburn, et. al. (1993). The vertical tails are oriented normal to the upper surface of the delta wing and have a centerline sweep of 53.5°. A multi-block grid consisting of 4 blocks is used for the solution of the problem. The first block is a O-H grid for the wing and upstream region, with 101X50X54 grid points in the wrap around, normal and axial directions, respectively. The second block is a H-H grid for the inboard region of the twin tails, with 23X50X13 grid points in the wrap around, normal and axial directions, respectively. The third block is a H-H grid for the outboard region of the twin tails, with 79X50X13 grid points in the wrap around, normal and axial directions, respectively. The fourth block is a O-H grid for the downstream region of the twin tails, with 101X50X25 grid points in the wrap around, normal and axial directions, respectively. Figure 1 shows the three dimensional grid topology and a front view blow-up of the twin tail-delta wing configuration.

Each tail is made of a single Aluminum spar and Balsa wood covering. The Aluminum spar has a taper ratio of 0.3 and a constant thickness of 0.001736. The chord length at the root is 0.03889 and at the tip is 0.011667, with a span length of 0.2223. The Aluminum spar is constructed from 6061-T6 alloy with density, ρ , moduli of elasticity and rigidity, E and G , of 2693 kg/m³, 6.896X10¹⁰ N/m² and 2.5925X10¹⁰ N/m²; respectively. The corresponding dimensionless

1
2
3
4
5
6
7
8
9
10
11
12
13
14
15
16
17
18
19
20
21
22
23
24
25
26
27
28
29
30
31
32
33
34
35
36
37
38
39
40
41
42
43
44
45
46
47
48
49
50
51
52
53
54
55
56
57
58
59
60
61
62
63
64
65
66
67
68
69
70
71
72
73
74
75
76
77
78
79
80
81
82
83
84
85
86
87
88
89
90
91
92
93
94
95
96
97
98
99
100
101
102
103
104
105
106
107
108
109
110
111
112
113
114
115
116
117
118
119
120
121
122
123
124
125
126
127
128
129
130
131
132
133
134
135
136
137
138
139
140
141
142
143
144
145
146
147
148
149
150
151
152
153
154
155
156
157
158
159
160
161
162
163
164
165
166
167
168
169
170
171
172
173
174
175
176
177
178
179
180
181
182
183
184
185
186
187
188
189
190
191
192
193
194
195
196
197
198
199
200
201
202
203
204
205
206
207
208
209
210
211
212
213
214
215
216
217
218
219
220
221
222
223
224
225
226
227
228
229
230
231
232
233
234
235
236
237
238
239
240
241
242
243
244
245
246
247
248
249
250
251
252
253
254
255
256
257
258
259
260
261
262
263
264
265
266
267
268
269
270
271
272
273
274
275
276
277
278
279
280
281
282
283
284
285
286
287
288
289
290
291
292
293
294
295
296
297
298
299
300
301
302
303
304
305
306
307
308
309
310
311
312
313
314
315
316
317
318
319
320
321
322
323
324
325
326
327
328
329
330
331
332
333
334
335
336
337
338
339
340
341
342
343
344
345
346
347
348
349
350
351
352
353
354
355
356
357
358
359
360
361
362
363
364
365
366
367
368
369
370
371
372
373
374
375
376
377
378
379
380
381
382
383
384
385
386
387
388
389
390
391
392
393
394
395
396
397
398
399
400
401
402
403
404
405
406
407
408
409
410
411
412
413
414
415
416
417
418
419
420
421
422
423
424
425
426
427
428
429
430
431
432
433
434
435
436
437
438
439
440
441
442
443
444
445
446
447
448
449
450
451
452
453
454
455
456
457
458
459
460
461
462
463
464
465
466
467
468
469
470
471
472
473
474
475
476
477
478
479
480
481
482
483
484
485
486
487
488
489
490
491
492
493
494
495
496
497
498
499
500
501
502
503
504
505
506
507
508
509
510
511
512
513
514
515
516
517
518
519
520
521
522
523
524
525
526
527
528
529
530
531
532
533
534
535
536
537
538
539
540
541
542
543
544
545
546
547
548
549
550
551
552
553
554
555
556
557
558
559
560
561
562
563
564
565
566
567
568
569
570
571
572
573
574
575
576
577
578
579
580
581
582
583
584
585
586
587
588
589
590
591
592
593
594
595
596
597
598
599
600
601
602
603
604
605
606
607
608
609
610
611
612
613
614
615
616
617
618
619
620
621
622
623
624
625
626
627
628
629
630
631
632
633
634
635
636
637
638
639
640
641
642
643
644
645
646
647
648
649
650
651
652
653
654
655
656
657
658
659
660
661
662
663
664
665
666
667
668
669
670
671
672
673
674
675
676
677
678
679
680
681
682
683
684
685
686
687
688
689
690
691
692
693
694
695
696
697
698
699
700
701
702
703
704
705
706
707
708
709
710
711
712
713
714
715
716
717
718
719
720
721
722
723
724
725
726
727
728
729
730
731
732
733
734
735
736
737
738
739
740
741
742
743
744
745
746
747
748
749
750
751
752
753
754
755
756
757
758
759
760
761
762
763
764
765
766
767
768
769
770
771
772
773
774
775
776
777
778
779
780
781
782
783
784
785
786
787
788
789
790
791
792
793
794
795
796
797
798
799
800
801
802
803
804
805
806
807
808
809
810
811
812
813
814
815
816
817
818
819
820
821
822
823
824
825
826
827
828
829
830
831
832
833
834
835
836
837
838
839
840
841
842
843
844
845
846
847
848
849
850
851
852
853
854
855
856
857
858
859
860
861
862
863
864
865
866
867
868
869
870
871
872
873
874
875
876
877
878
879
880
881
882
883
884
885
886
887
888
889
890
891
892
893
894
895
896
897
898
899
900
901
902
903
904
905
906
907
908
909
910
911
912
913
914
915
916
917
918
919
920
921
922
923
924
925
926
927
928
929
930
931
932
933
934
935
936
937
938
939
940
941
942
943
944
945
946
947
948
949
950
951
952
953
954
955
956
957
958
959
960
961
962
963
964
965
966
967
968
969
970
971
972
973
974
975
976
977
978
979
980
981
982
983
984
985
986
987
988
989
990
991
992
993
994
995
996
997
998
999
1000

quantities are 2198, 4.595×10^5 and 1.727×10^5 ; respectively.

The Balsa wood covering has a taper ratio of 0.23 and aspect ratio of 1.4. The chord length at the root is 0.2527 and at the tip is 0.058, with a span length of 0.2223. The Balsa thickness decreases gradually from 0.0211 at the tail root to 0.0111 at the tail midspan and then constant thickness of 0.0111 is maintained to the tail tip. The tail cross section is a semi-diamond shape with bevel angle of 20° . The Balsa density, moduli of elasticity and rigidity, E and G , are 179.7 kg/m^3 , $6.896 \times 10^8 \text{ N/m}^2$ and $2.5925 \times 10^8 \text{ N/m}^2$; respectively. The corresponding dimensionless quantities are 147, 4.595×10^3 and 1.727×10^3 ; respectively. The tails are assumed to be magnetically suspended and the leading edge of the tail root is positioned at $x/c = 1.0$, measured from the wing apex. The configuration is pitched at 30° angle of attack and the freestream Mach number and Reynolds number are 0.3 and 1.25×10^6 ; respectively. The configuration is investigated for two spanwise positions of the twin tails; the inboard position and the outboard position corresponding to a separation distance between the twin tails of 33% and 78% of the wing span; respectively.

Keeping the twin tail as rigid surfaces, the unsteady full Navier-Stokes equations are integrated time accurately using the implicit, flux-difference splitting scheme of Roe with Reynolds number of 1.25 million and angle of attack of 30° . The initial conditions are obtained after 10,000 time steps with $\Delta t = 0.001$. Next, the results of the coupled and uncoupled bending and torsion modes are presented. For the coupled bending and torsion case, the inertia axis is assumed downstream the elastic axis by $x_\theta = 0.003$. For the uncoupled case, $x_\theta = 0.0$.

4.2 Uncoupled Bending-Torsion Modes:

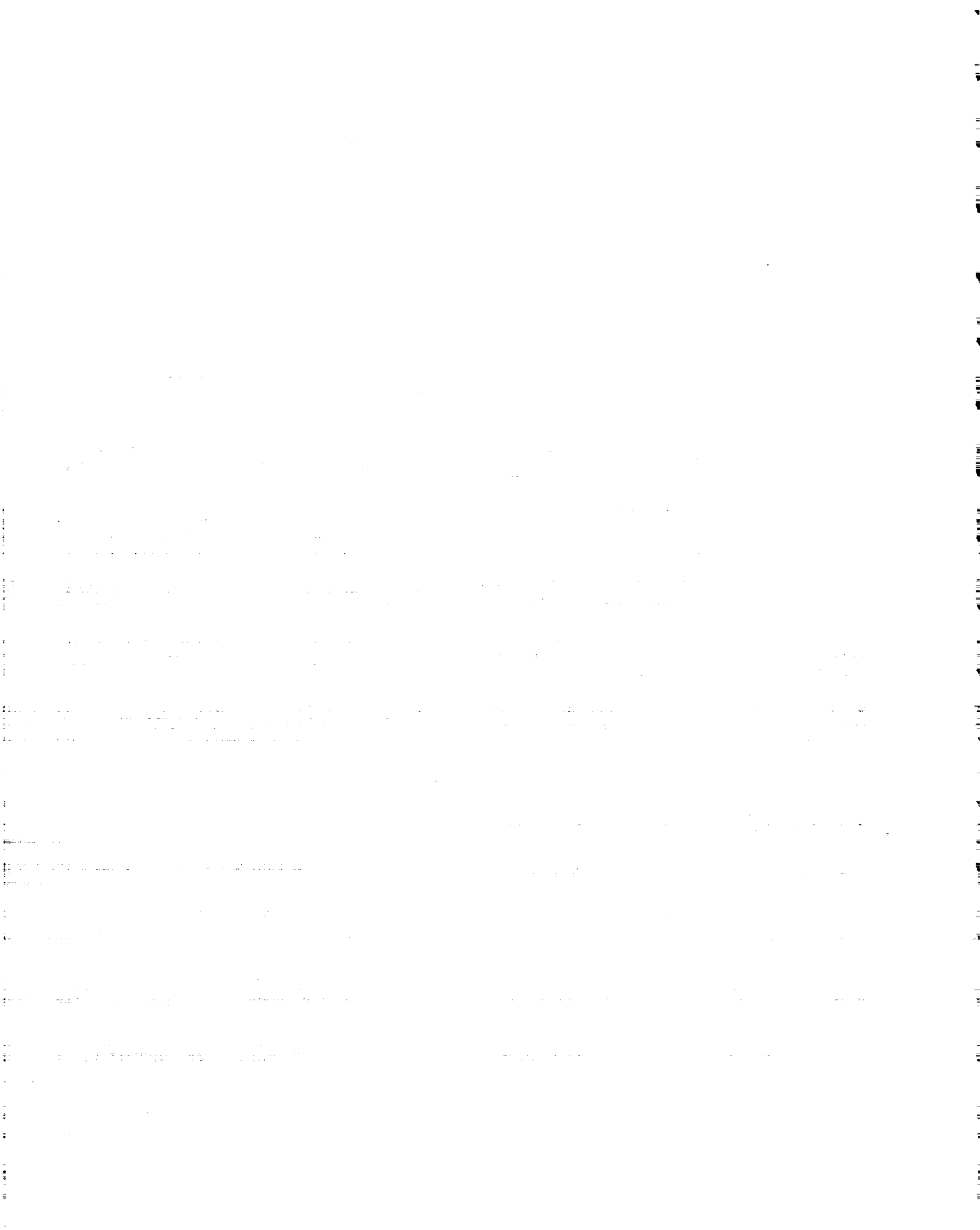
Figure 2 shows three-dimensional views of the leading-edge vortex cores particle traces and iso-total pressure surfaces. Figures 3 and 4 show front views for the total pressure contours on the wing surface and in cross flow planes at $x = 1.03$ and $x = 1.22$, and the instantaneous streamlines of the inboard tail position. The leading-edge vortex cores experience asymmetric breakdown upstream of the twin tail due to the upstream effect of the tails motion. The vortices are totally outboard of the twin tail. The cores are moved upward as the flow traveled downstream. Smaller size vortex cores appear underneath the primary wing vortex and it becomes larger in size as it travels downstream. These are the tail vortices observed by Washburn (1993). The tail vortices

exist at the outer surfaces of the tails and they are rotating in the opposite direction to those of the primary wing vortices. Figure 5 shows the distribution of the surface pressure coefficient covering the wing from $x = 0.3$ to $x = 1.0$. The largest suction peaks are pronounced at the position of the wing vortex cores, and the peaks values decreased as the flow travels downstream. Figure 6 shows the distribution of the leading-edge total structural deflection and the root bending moment for the left and right tails for 20 dimensionless time after the initial conditions. The tails deflections are in first, second and third mode shapes. The frequencies of the torsion deflections are almost twice those of the bending deflections.

Figure 7 shows three-dimensional views of the leading-edge vortex cores particle traces and iso-total pressure surfaces. Figures 8 and 9 show front views for the total pressure contours on the wing surface and in cross flow planes at $x = 1.03$ and $x = 1.22$, and the instantaneous streamlines of the outboard tail position. The tails cut through the vortex breakdown flow of the leading-edge vortex cores. The tail vortices are also outboard of the tails. The location of the vortex core with respect to the tail produces an increase in the aerodynamic damping, causing the tail deflection to decrease. The tail vortices are also shown to rotate in the opposite direction to those of the primary wing vortices. Figure 10 shows the distribution of the surface pressure coefficient covering the wing from $x = 0.3$ to $x = 1.0$. The suction peaks are less than those of the inboard twin-tail case. Figure 11 shows the distribution of the leading-edge total structural deflection and the root bending moment for the left and right tails for 20 dimensionless time after the initial conditions. The levels of loads and defections are much lower than those of the inboard twin-tail case. The tails are shown to oscillate in one direction only in first and second mode shapes.

4.3 Coupled Bending-Torsion Modes:

Figure 12 shows three-dimensional views of the leading-edge vortex cores particle traces and iso-total pressure surfaces. Figures 13 and 14 show front views for the total pressure contours on the wing surface and in cross flow planes at $x = 1.03$ and $x = 1.22$, and the instantaneous streamlines of the inboard tail position. Although, the vortex breakdown location is approximately at the same position as the uncoupled case, the shape and traces of the breakdown flow are different which show the upstream effect of the twin-tail motion. The vortex cores are moved more upward than that of the uncoupled case and continue moving upward as the flow travels downstream. Figure



15 shows the distribution of the surface pressure coefficient covering the wing from $x = 0.3$ to $x = 1.0$. Figure 16 shows the distribution of the leading-edge total structural deflection and the root bending moment for the left and right tails for 60 dimensionless time after the initial conditions. The tails deflections and levels of loads are higher than those of the uncoupled case. The tails deflections are in first, second and third mode shapes.

Figure 17 shows three-dimensional views of the leading-edge vortex cores particle traces and iso-total pressure surfaces. Figures 18 and 19 show front views for the total pressure contours on the wing surface and in cross flow planes at $x = 1.03$ and $x = 1.22$, and the instantaneous streamlines of the outboard tail position. The shape of the vortex breakdown is slightly different than that of the uncoupled case. This is because of the lower levels of the tail deflections which reduce the upstream effect on the flow. Figure 20 shows the distribution of the surface pressure coefficient covering the wing from $x = 0.3$ to $x = 1.0$. Figure 21 shows the distribution of the leading-edge total structural deflection and the root bending moment for the left and right tails for 60 dimensionless time after the initial conditions. The tails deflections and levels of loads are higher than those of the uncoupled case but still much lower than those of the uncoupled and coupled cases of the inboard twin-tail position. The tails are deflected in one direction only in first and second mode shapes.

5 CONCLUDING REMARKS

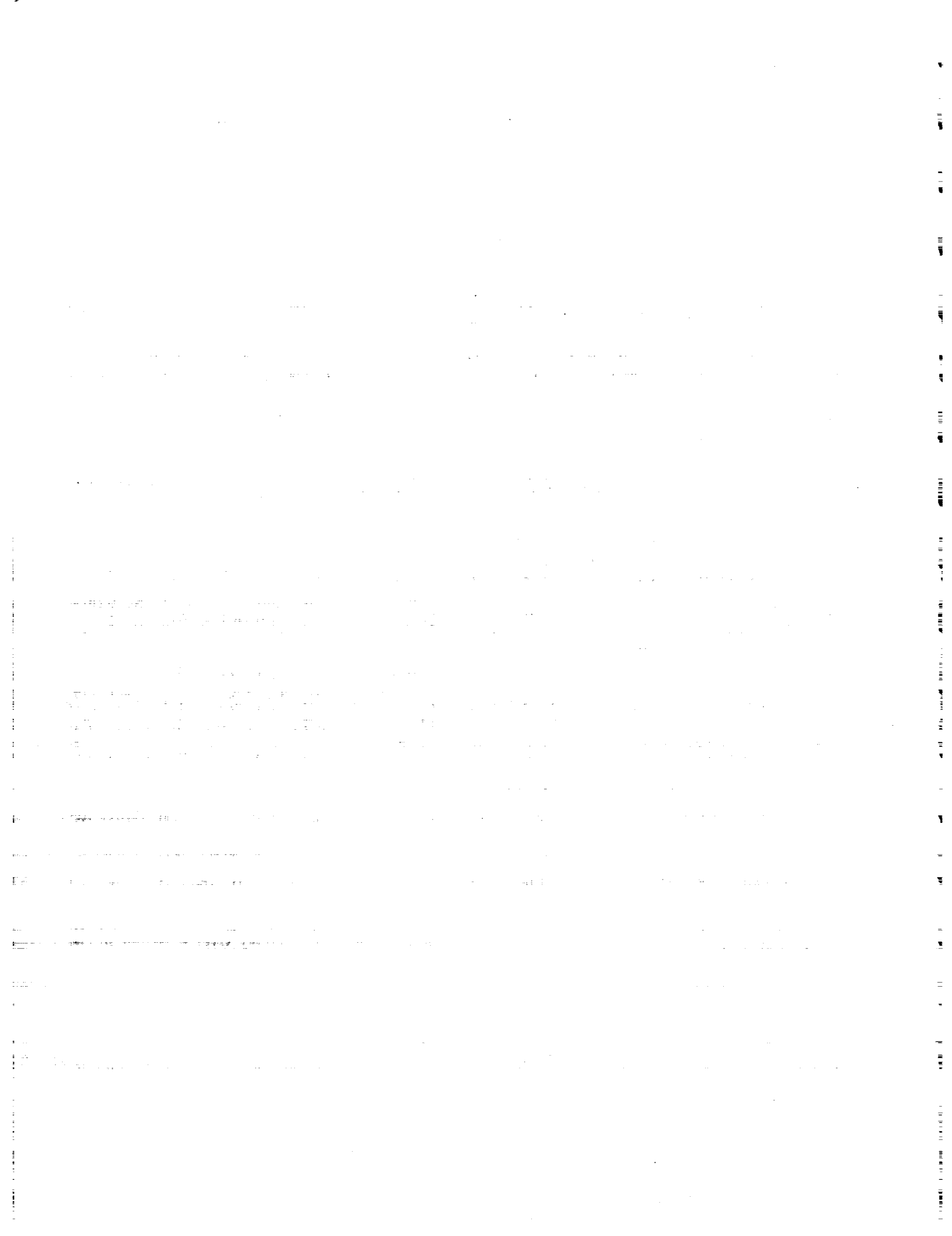
The effect of coupled and uncoupled bending and torsion modes on the twin-tail buffet response are investigated for different spanwise positions of the twin-tail. The coupled bending and torsion modes produce higher deflections and loads than those of the uncoupled modes cases. The inboard position of the twin-tail produces the largest bending and torsion loads and deflections when compared with the results of the outboard position. It has been shown that the larger the tail deflections are, the higher the upstream effect on the vortex breakdown flow upstream of the tails. The computational results presented are in good quantitative agreement with the experimental data of Washburn, et.al. (1993).

6 ACKNOWLEDGMENT

This research work is supported under Grant No. NAG-1-994 by the NASA Langley Research Center. The authors would like to recognize the computational resources provided by the NAS facilities at Ames Research Center and the NASA Langley Research Center.

7 REFERENCES

- Bean, D. E. and Lee, B. H. K., 1994, "Correlation of Wind Tunnel and Flight Test Data for F/A-18 Vertical Tail Buffet," AIAA 94-1800-CP.
- Cole, S. R., Moss, S. W. and Dogget, R. V., Jr., 1990, "Some Buffet Response Characteristics of a Twin-Vertical-Tail Configuration," NASA TM-102749.
- Erickson, G. E., Hall, R. M., Banks, D. W., Del Frate, J. H., Shreiner, J. A., Hanley, R. J. and Pulley, C. T., 1989, "Experimental Investigation of the F/A-18 Vortex Flows at Subsonic Through Transonic Speeds," AIAA 89-2222.
- Kandil, O. A., Kandil, H. A. and Massey, S. J., 1993, "Simulation of Tail Buffet Using Delta Wing-Vertical Tail Configuration," AIAA 93-3688-CP, AIAA Atmospheric Flight Mechanics Conference, Monterey, CA, pp. 566-577.
- Kandil, O. A., Massey, S. J., and Kandil, H. A., 1994, "Computations of Vortex-Breakdown Induced Tail Buffet Undergoing Bending and Torsional Vibrations," AIAA 94-1428-CP, AIAA/ASME/ASCE/ASC Structural, Structural Dynamics and Material Conference, SC, pp. 977-993.
- Kandil, O. A., Massey, S. J. and Sheta, E. F., 1995, "Structural Dynamics/CFD Interaction for Computation of Vertical Tail Buffet," International Forum on Aeroelasticity and Structural Dynamics, Royal Aeronautical Society, Manchester, U.K., June 26-28, pp. 52.1-52.14. Also published in Royal Aeronautical Journal, August/September 1996, pp. 297-303.
- Kandil, O. A., Sheta, E. F. and Liu, C. H., 1996, "Computation and Validation of Fluid/Structure Twin-Tail Buffet Response," Euro-mech Colloquium 349, Structure Fluid Interaction in Aeronautics, Institute Fur Aeroelastik, Gottingen, Germany.
- Kandil, O. A., Sheta, E. F. and Massey, S. J., 1997, "Fluid/Structure Twin Tail Buffet Response Over A Wide Range of Angles of Attack," AIAA 97-2261-CP, 15th AIAA Applied Aerodynamics Conference, Atlanta, GA.
- Lee, B. and Brown, D., 1990, "Wind Tunnel Studies of F/A-18 Tail Buffet," AIAA 90-1432.
- Sellers, W. L. III, Meyers, J. F. and Hepner, T. E., 1988, "LDV Survey Over a Fighter Model at Moderate to High Angle of Attack," SAE Paper 88-1448.
- Washburn, A. E., Jenkins, L. N. and Ferman, M. A., 1993, "Experimental Investigation of Vortex-Fin Interaction," AIAA 93-0050, AIAA 31st ASM, Reno, NV.
- Wentz, W. H., 1987, "Vortex-Fin Interaction on a Fighter Aircraft," AIAA 87-2474, AIAA Fifth Applied Aerodynamics Conference, Monterey, CA.



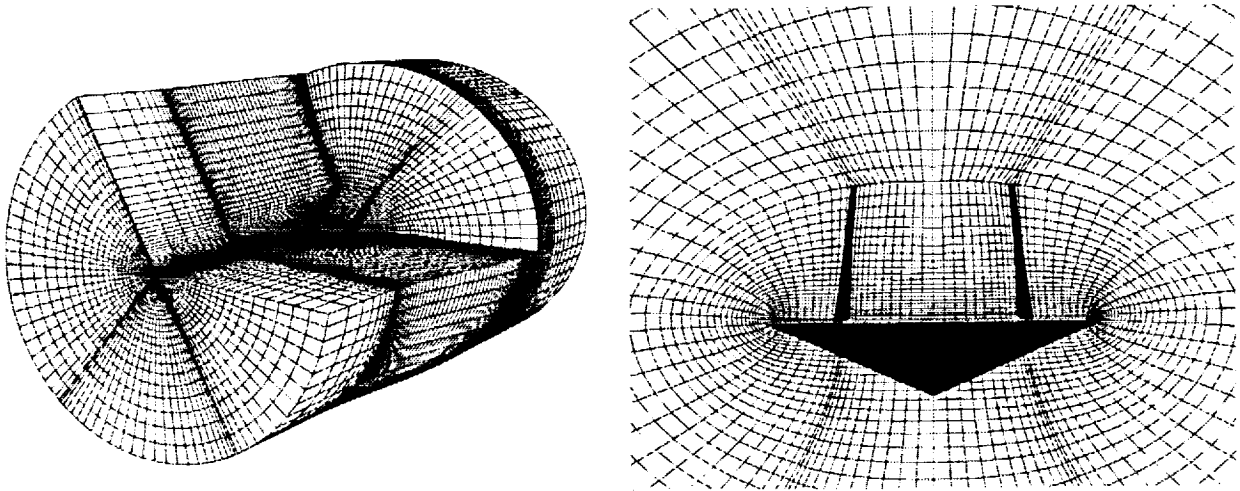


Figure 1: Three-dimensional grid topology and blow-up of the twin tail-delta wing configuration (the tails are in midspan position).

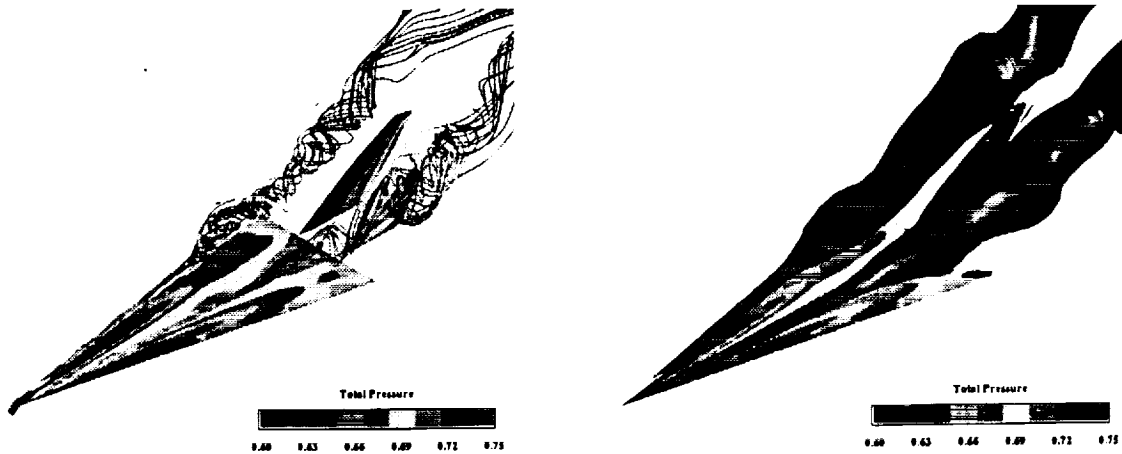


Figure 2: Three-dimensional views showing the total pressure on the surfaces, vortex core particle traces and iso-total pressure surfaces. Uncoupled case after $it = 9,600$, Inboard position.

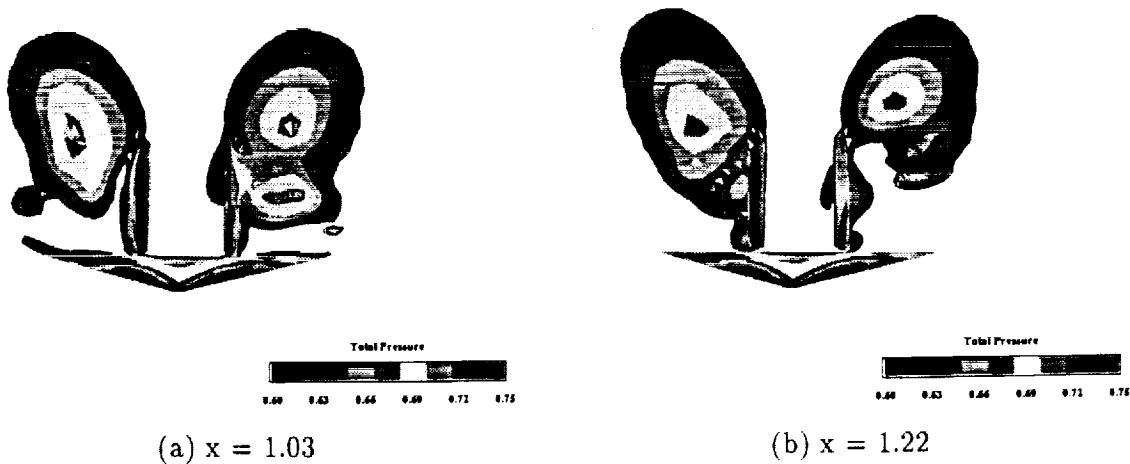
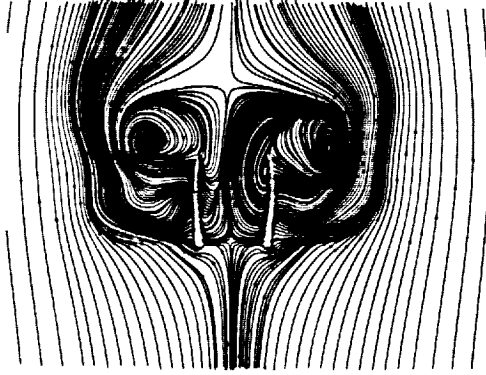
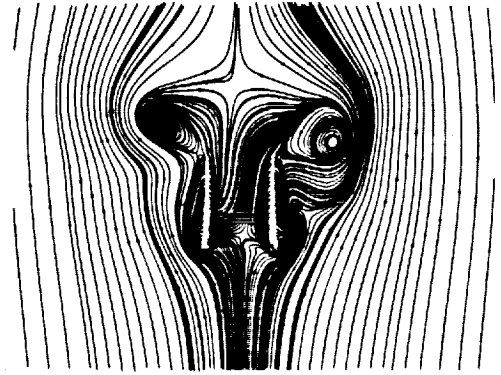


Figure 3: Snap shots of total pressure in a cross-flow planes. Uncoupled case after $it = 9,600$, Inboard position.



(a) $x = 1.03$



(b) $x = 1.22$

Figure 4: Snap shots of instantaneous streamlines in a cross-flow planes. Uncoupled case after $it = 9,600$, Inboard position..

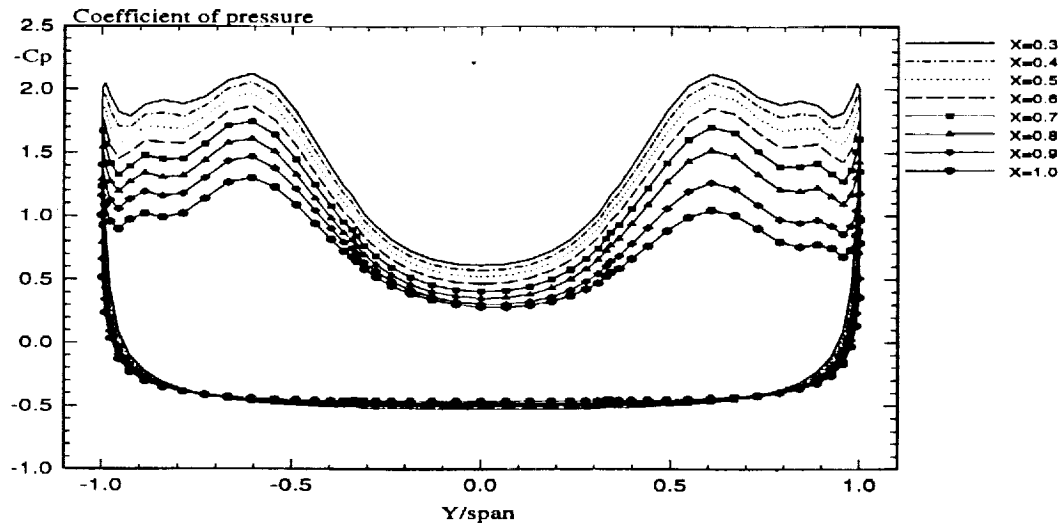
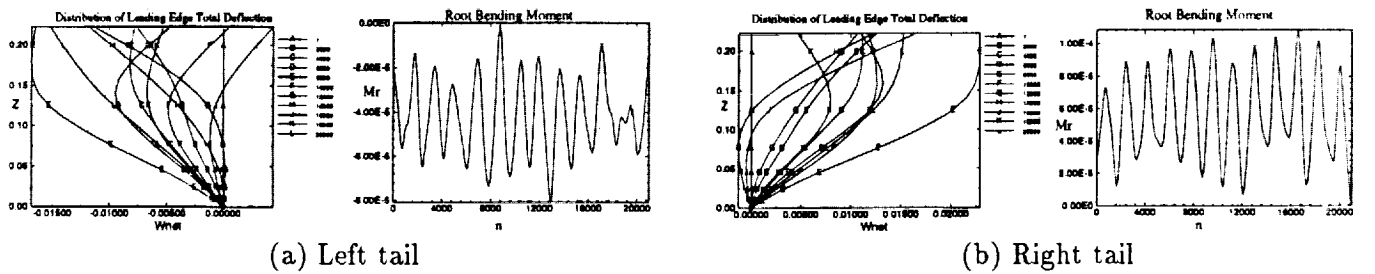


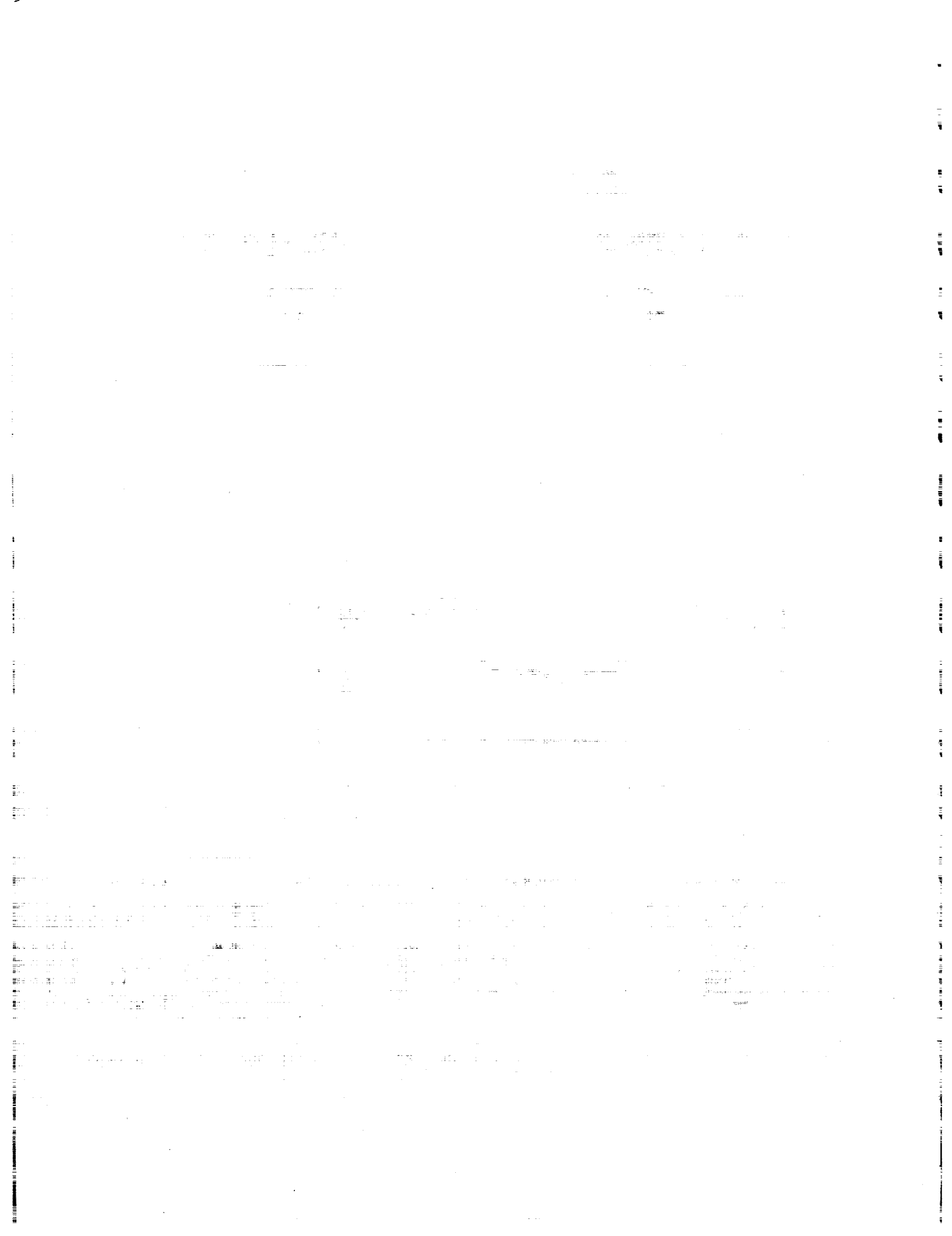
Figure 5: Distribution of Coefficient of pressure. Uncoupled case after $it = 9,600$, Inboard position.



(a) Left tail

(b) Right tail

Figure 6: Tail leading-edge total structural deflections and root bending moment for an uncoupled bending-torsion case. $M_\infty = 0.3$, $\alpha = 30^\circ$, $R_e = 1.25 \times 10^6$, Inboard position.



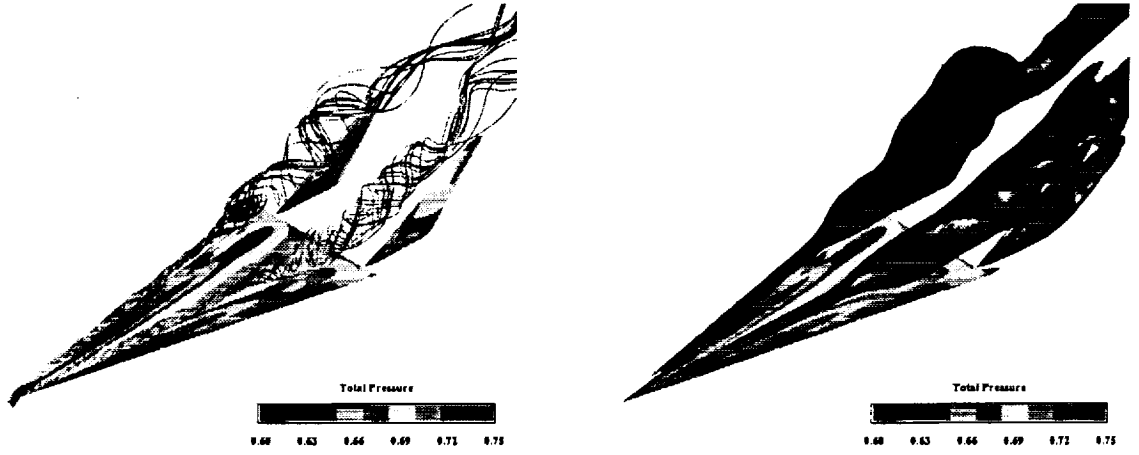


Figure 7: Three-dimensional views showing the total pressure on the surfaces, vortex core particle traces and iso-total pressure surfaces. Uncoupled case after $it = 9,600$, Outboard position.



Figure 8: Snap shots of total pressure in a cross-flow planes. Uncoupled case after $it = 9,600$, Outboard position.

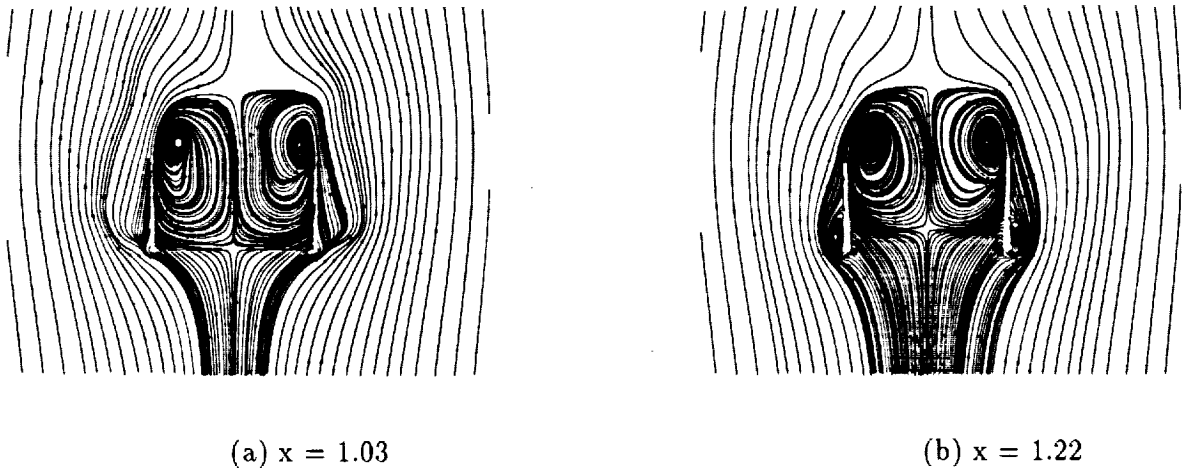


Figure 9: Snap shots of instantaneous streamlines in a cross-flow planes. Uncoupled case after $it = 9,600$, Outboard position.

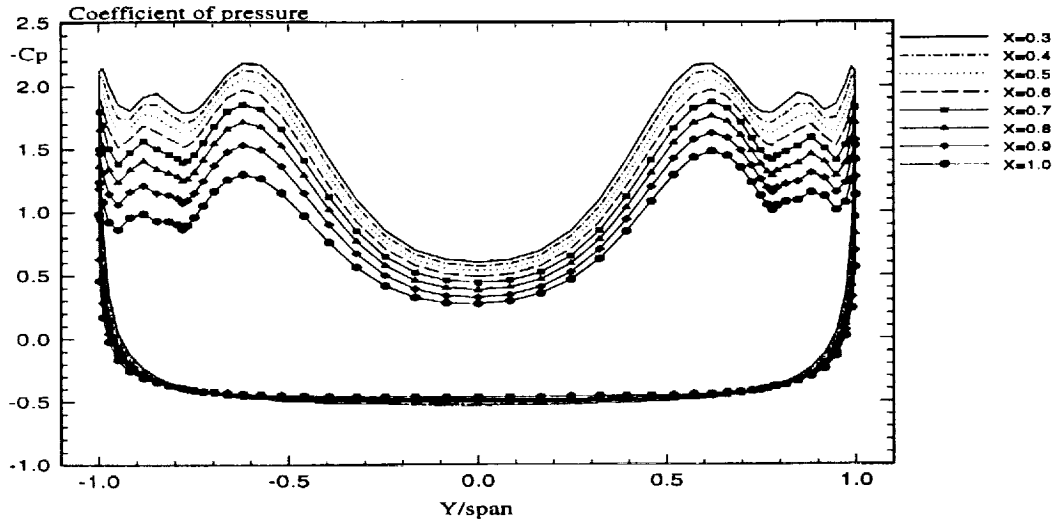


Figure 10: Distribution of Coefficient of pressure. Uncoupled case after $it = 9,600$, Outboard position.

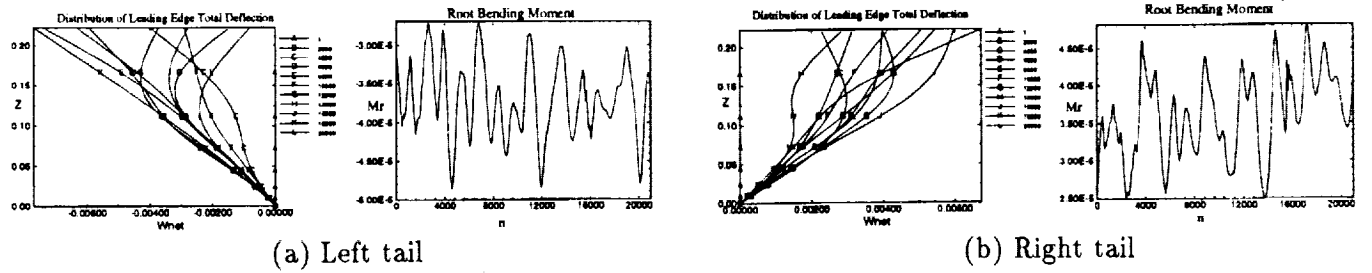


Figure 11: Tail leading-edge total structural deflections and root bending moment for an uncoupled bending-torsion case. $M_\infty = 0.3$, $\alpha = 30^\circ$, $R_e = 1.25 \times 10^6$, Outboard position.

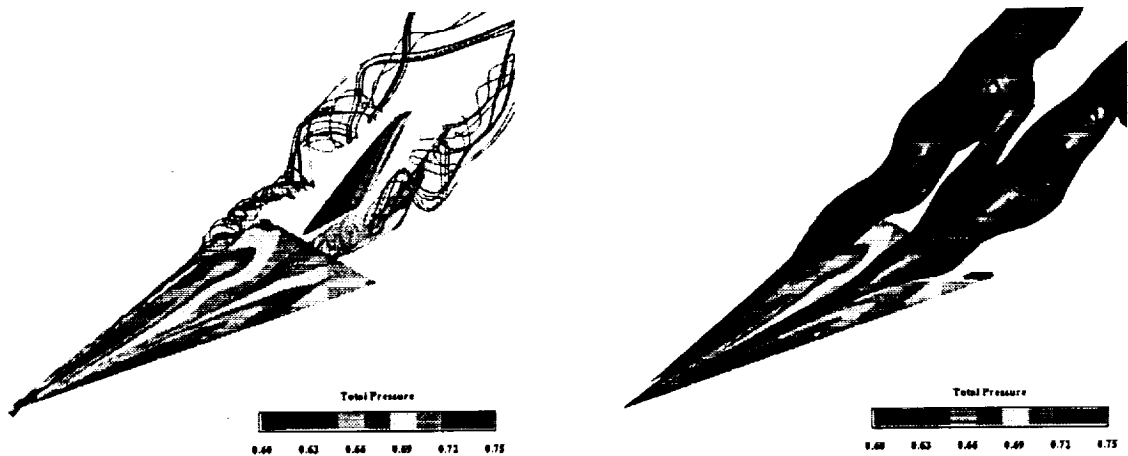
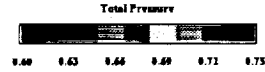
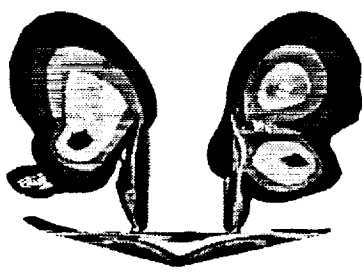
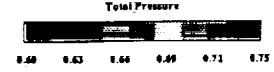
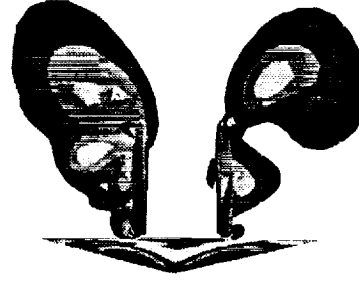


Figure 12: Three-dimensional views showing the total pressure on the surfaces, vortex core particle traces and iso-total pressure surfaces. Coupled case after $it = 9,600$, $x_\theta = 0.003$, Inboard position.

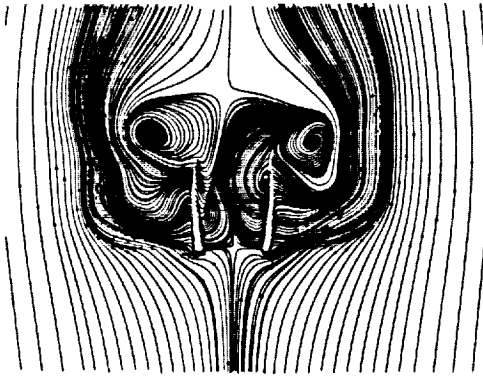


(a) $x = 1.03$

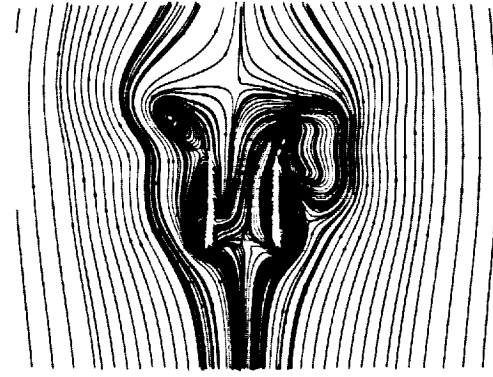


(b) $x = 1.22$

Figure 13: Snap shots of total pressure in a cross-flow planes. Coupled case after $it = 9,600$, $x_\theta = 0.003$, Inboard position.



(a) $x = 1.03$



(b) $x = 1.22$

Figure 14: Snap shots of instantaneous streamlines in a cross-flow planes. Coupled case after $it = 9,600$, $x_\theta = 0.003$, Inboard position.

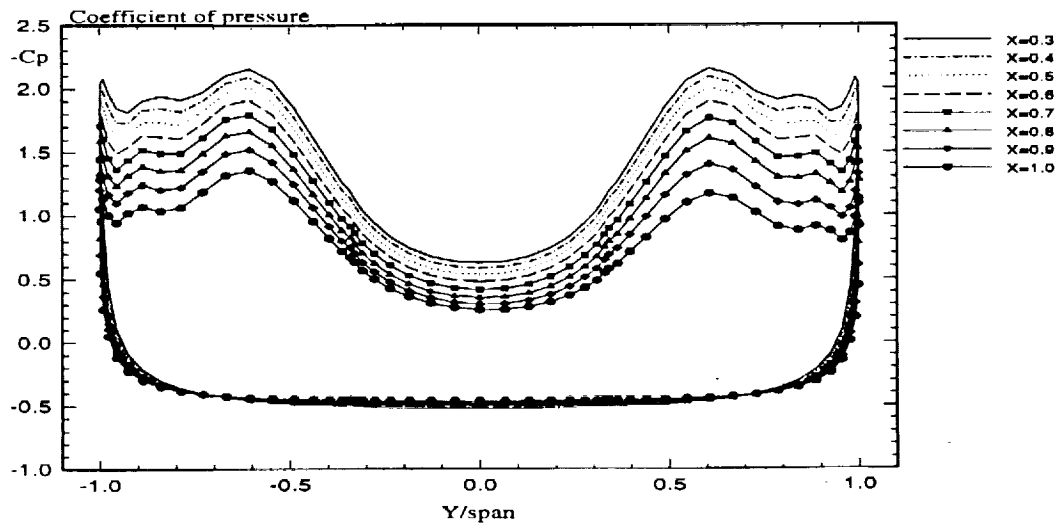


Figure 15: Distribution of Coefficient of pressure. Coupled case after $it = 9,600$, $x_\theta = 0.003$, Inboard position.

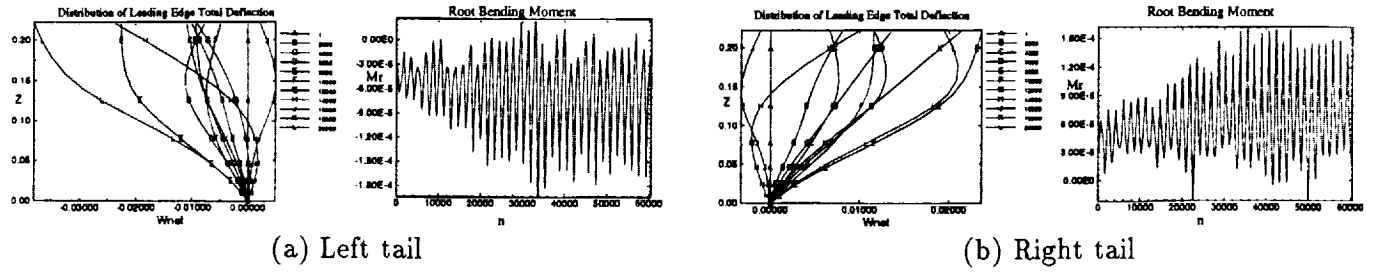


Figure 16: Tail leading-edge total structural deflections and root bending moment for coupled bending-torsion case, $x_\theta = 0.003$. $M_\infty = 0.3$, $\alpha = 30^\circ$, $R_e = 1.25 \times 10^6$, Inboard position.

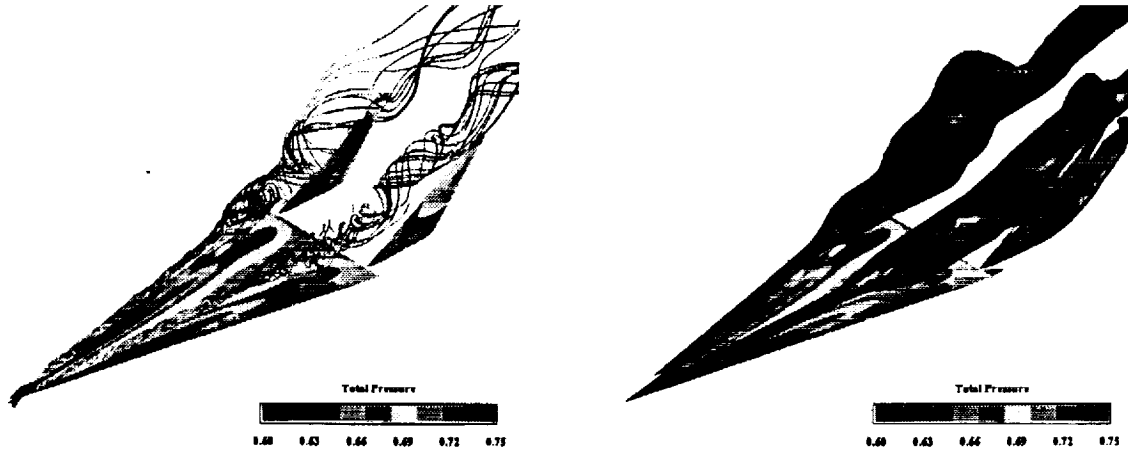


Figure 17: Three-dimensional views showing the total pressure on the surfaces, vortex core particle traces and iso-total pressure surfaces. Coupled case after $it = 9,600$, $x_\theta = 0.003$, Outboard position.

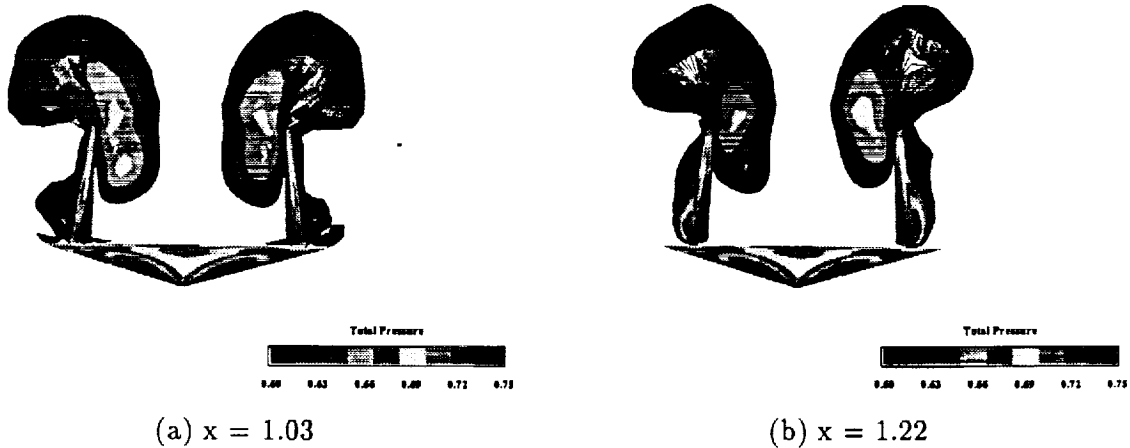
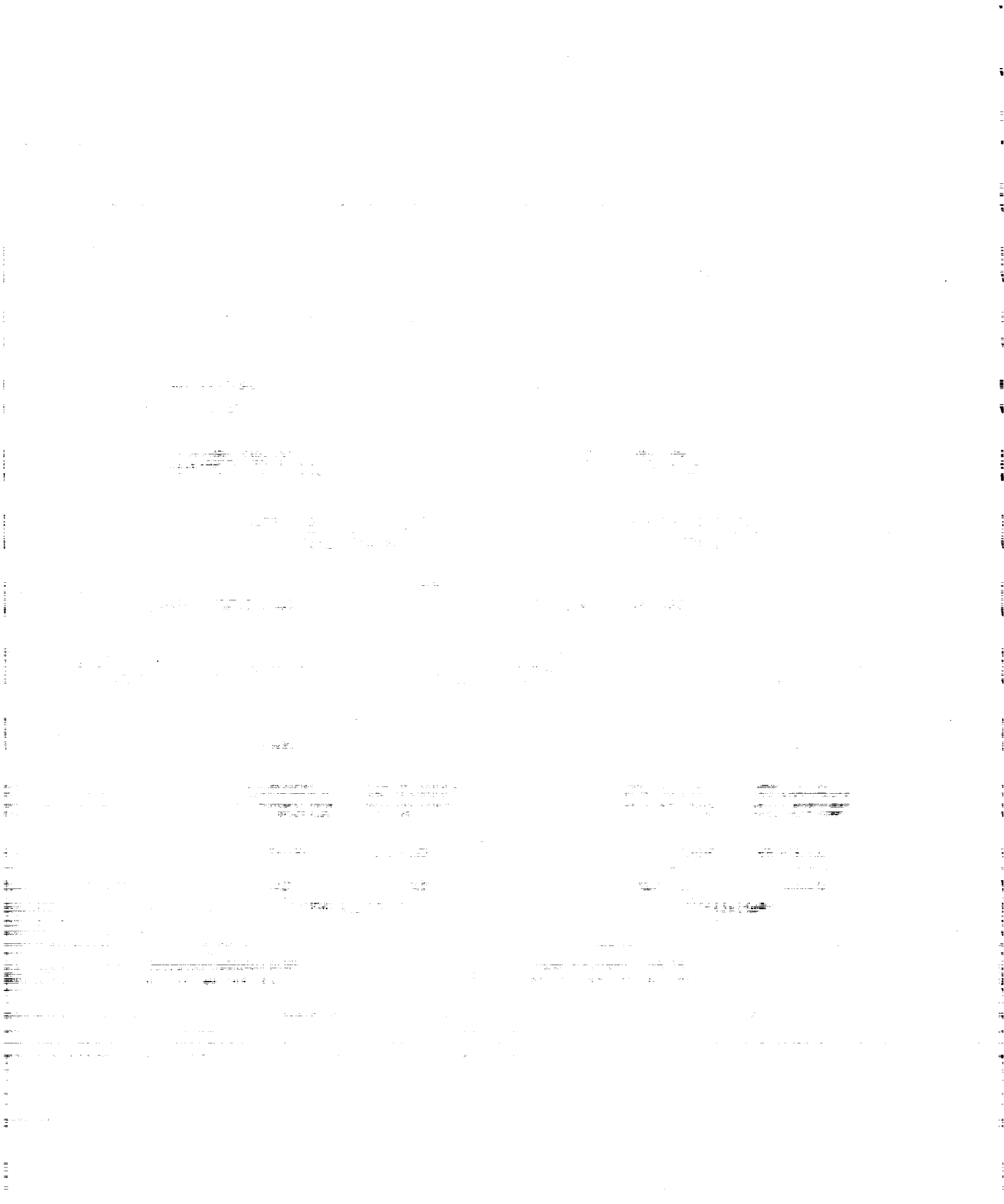
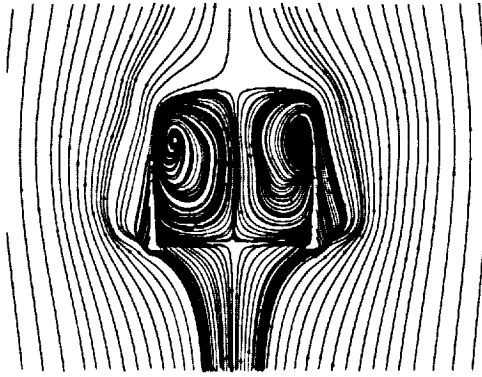
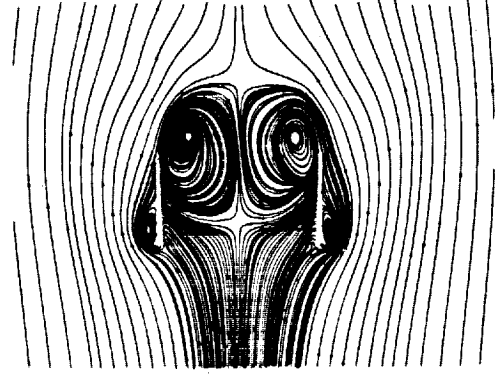


Figure 18: Snap shots of total pressure in a cross-flow planes. Coupled case after $it = 9,600$, $x_\theta = 0.003$, Outboard position.





(a) $x = 1.03$



(b) $x = 1.22$

Figure 19: Snap shots of instantaneous streamlines in a cross-flow planes. Coupled case after $it = 9,600$, $x_\theta = 0.003$, Outboard position.

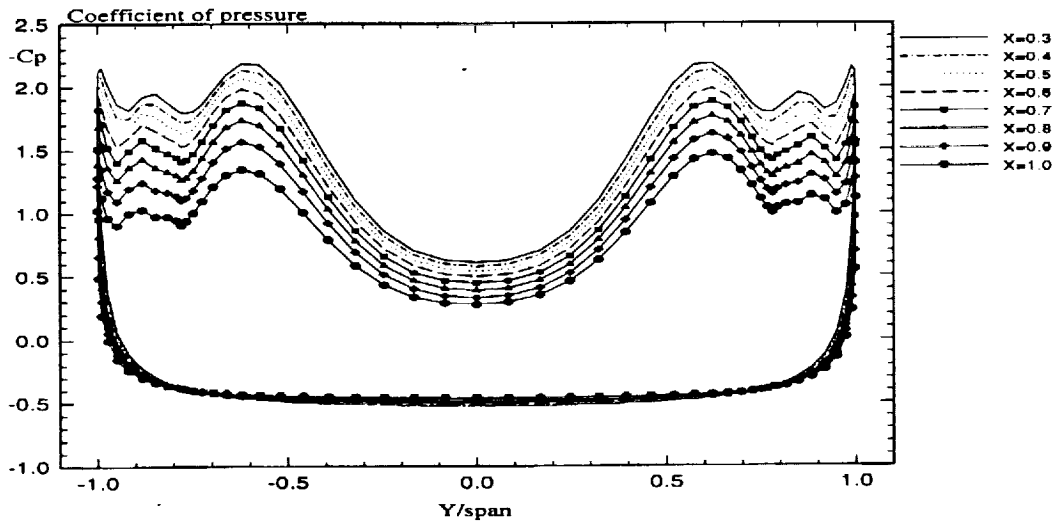
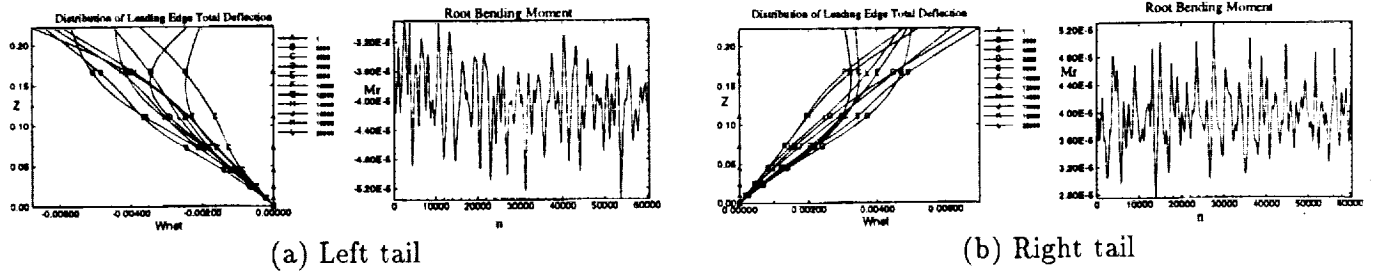


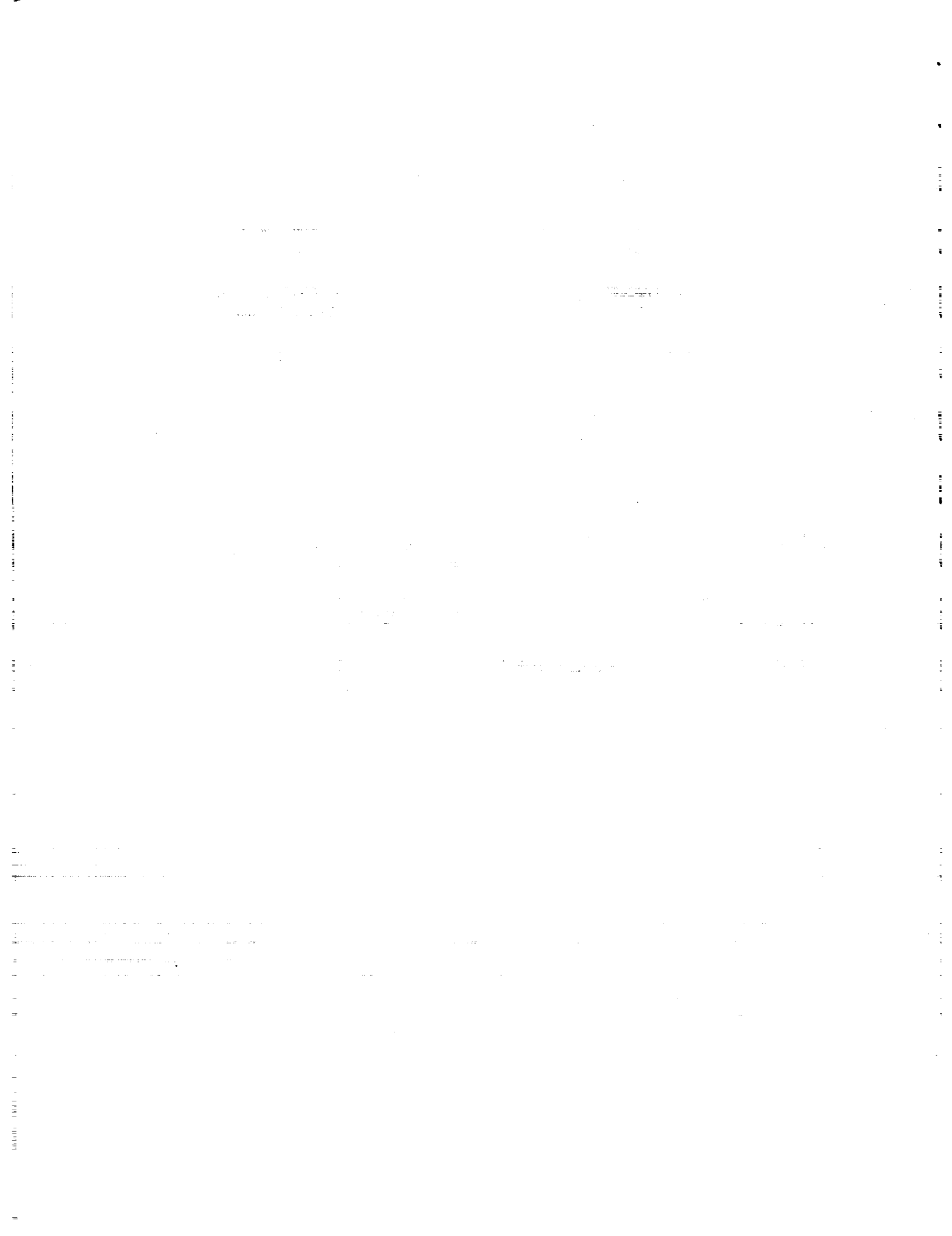
Figure 20: Distribution of Coefficient of pressure. Coupled case after $it = 9,600$, $x_\theta = 0.003$, Outboard position.



(a) Left tail

(b) Right tail

Figure 21: Tail leading-edge total structural deflections and root bending moment for coupled bending-torsion case, $x_\theta = 0.003$. $M_\infty = 0.3$, $\alpha = 30^\circ$, $R_e = 1.25 \times 10^6$, Outboard position.





AIAA 97-2261-CP

**FLUID/STRUCTURE TWIN TAIL BUFFET RESPONSE
OVER A WIDE RANGE OF ANGLES OF ATTACK**

**Osama A. Kandil, Essam F. Sheta
and Steven J. Massey**

**Aerospace Engineering Department
Old Dominion University
Norfolk, VA 23529**

**15th AIAA APPLIED AERODYNAMICS
CONFERENCE**

Atlanta, GA-June 23-25, 1997

Cover 2

FLUID/STRUCTURE TWIN TAIL BUFFET RESPONSE OVER A WIDE RANGE OF ANGLES OF ATTACK

Osama A. Kandil¹, Essam F. Sheta² and Steven J. Massey³

Aerospace Engineering Department
Old Dominion University, Norfolk, VA 23529, USA

ABSTRACT

The buffet response of the flexible twin-tail/delta wing configuration—a multidisciplinary problem is solved using three sets of equations on a multi-block grid structure. The first set is the unsteady, compressible, Reynolds-averaged Navier-Stokes equations which are used for obtaining the flow-field vector and the aerodynamic loads on the twin tails. The second set is the coupled aeroelastic equations which are used for obtaining the bending and torsional deflections of the twin tails. The third set is the grid-displacement equations which are used for updating the grid coordinates due to the tail deflections. The configuration is pitched at wide range of angles of attack; 15° to 40° , and the freestream Mach number and Reynolds number are 0.3 and 1.25 million, respectively. With the twin tails fixed as rigid surfaces, the problem is solved for the initial flow conditions. Next, the problem is solved for the twin tail response for uncoupled bending and torsional vibrations due to the unsteady loads produced by the vortex breakdown flow of the leading-edge vortex cores. The configuration is investigated for two spanwise positions of the twin tails; inboard and outboard locations. The computational results are validated and are in very good agreement with the experimental data of Washburn, et. al.

INTRODUCTION

In order to maximize the effectiveness of the fighter aircraft that operate well beyond the buffet onset boundary, the design of the new generation of fighter aircraft should account for both high maneuver capabilities at high and wide range of

angles of attack, and the aeroelastic buffet characteristics at high alpha. The maneuver capabilities are achieved, for example in the F/A-18 fighter, through the combination of the leading-edge extension (LEX) with a delta wing and the use of vertical tails. The LEX maintains lift at high angles of attack by generating a pair of vortices that trail aft over the top of the aircraft. The vortex entrains air over the vertical tails to maintain stability of the aircraft. At some flight conditions, the vortices emanating from the highly-swept LEX of the delta wing breakdown before reaching the vertical tails which get bathed in a wake of unsteady highly-turbulent, swirling flow. The vortex-breakdown flow produces unsteady, unbalanced loads on the vertical tails and causes a peak in the pressure spectrum that may be tuned to different structural modes depending on the angle of attack and dynamic pressure. This in turn produce severe buffet on the tails and has led to their premature fatigue failure. Therefore, the evaluation of the buffet characteristics must account for the turbulent characteristics of the oncoming flow. If the power spectrum of the turbulence is accurately predicted, the intensity of the buffeting motion can be computed and the structural components of the aircraft can be designed accordingly.

Experimental investigation of the vertical tail buffet of the F/A-18 models have been conducted by several investigators such as Sellers, et al.¹, Erickson, et al.², Wentz³, Lee and Brown⁴, and Cole, et al.⁵. These experiments showed that the vortex produced by the LEX of the wing breaks down ahead of the vertical tails at angles of attack of 25° and higher producing unsteady loads on the vertical tails, and the buffet

¹Professor, Eminent Scholar and Dept. Chair, Associate Fellow AIAA.

²Ph.D. Graduate Research Assistant, Member AIAA.

³Ph.D. Graduate Research Assistant, Member AIAA.

response occurs in the first bending mode, increases with increasing dynamic pressure and is larger at $M = 0.3$ than that at a higher Mach numbers. Bean and Lee⁶ showed that buffeting in the torsional mode occurred at a lower angle of attack and at larger levels compared to the fundamental bending mode.

An extensive experimental investigation has been conducted to study vortex-tail interaction on a 76° sharp-edged delta wing with vertical twin-tail configuration by Washburn, Jenkins and Ferman⁷. The vertical tails were placed at nine locations behind the wing. The experimental data showed that the aerodynamic loads are more sensitive to the chordwise tail location than its spanwise location. As the tails were moved laterally toward the vortex core, the buffeting response and excitation were reduced. Although the tail location did not affect the vortex core trajectories, it affected the location of vortex-core breakdown. Moreover, the investigation showed that the presence of a flexible tail can affect the unsteady pressures on the rigid tail on the opposite side of the model.

Kandil, Kandil and Massey⁸ presented the first successful computational simulation of the vertical tail buffet using a delta wing-single flexible vertical tail configuration. The tail was allowed to oscillate in bending modes. The flow conditions and wing angle of attack have been selected to produce an unsteady vortex-breakdown flow. Unsteady vortex breakdown of leading-edge vortex cores was captured, and unsteady pressure forces were obtained on the tail. Kandil, et al.⁹⁻¹¹ allowed the vertical tail to oscillate in both bending and torsional modes. The total deflections and the frequencies of deflections and loads of the coupled bending-torsion case were found to be one order of magnitude higher than those of the bending case only. The loads on the tail in the transonic flow regime were one order of magnitude lower than those of the subsonic flow. Also, it has been shown that the tail oscillations change the vortex breakdown locations and the unsteady aerodynamic loads on the wing and tail.

In recent papers by the present authors^{12,13}, the buffet response of the F/A-18 and a generic F-117 twin tails were considered at $\alpha = 30^\circ$ and for different spanwise locations of the twin tails. A multi-block grid structure was used to solve

the problem. The loads, deflections, frequencies and root bending moments were reduced as the twin tails moved laterally toward the vortex core. The outboard location of the tails produced the least of these responses. The computational results were in full qualitative agreement with the experimental data of Washburn, et al.⁷.

In this paper, we consider the buffet response of delta-wing/twin-tail configuration similar to the one used by Washburn, et. al.⁷. The Baldwin and Lomax two-layer turbulent algebraic model¹⁴ is used to model flow turbulence. A multi-block grid structure is used to solve the problem over a wide range of angles of attack from 15° to 40° , and for two spanwise locations of the twin tails. The computational results are compared with the experimental data of Washburn, et. al.

FORMULATION

The formulation consists of three sets of governing equations along with certain initial and boundary conditions. The first set is the unsteady, compressible, Reynolds-averaged Navier-Stokes equations. The second set consists of the aeroelastic equations for bending and torsional modes. The third set consists of equations for deforming the grid according to the twin tail deflections. Next, the governing equations of each set along with the initial and boundary conditions are given.

Fluid-Flow Equations:

The conservative form of the dimensionless, unsteady, compressible, full Navier-Stokes equations in terms of time-dependent, body-conformed coordinates ξ^1 , ξ^2 and ξ^3 is given by

$$\frac{\partial \bar{Q}}{\partial t} + \frac{\partial \bar{E}_m}{\partial \xi^m} - \frac{\partial (\bar{E}_v)_s}{\partial \xi^s} = 0; m = 1-3, s = 1-3 \quad (1)$$

where

$$\xi^m = \xi^m(x_1, x_2, x_3, t) \quad (2)$$

$$\bar{Q} = \frac{1}{J} [\rho, \rho u_1, \rho u_2, \rho u_3, \rho e]^t, \quad (3)$$

\bar{E}_m and $(\bar{E}_v)_s$ are the ξ^m -inviscid flux and ξ^s -viscous and heat conduction flux, respectively. Details of these fluxes are given in Ref. 8. The

details of the two-layer turbulent algebraic model are given in Ref. 14.

Aeroelastic Equations:

The dimensionless, linearized governing equations for the coupled bending and torsional vibrations of a vertical tail that is treated as a cantilevered beam are considered. The tail bending and torsional deflections occur about an elastic axis that is displaced from the inertial axis. These equations for the bending deflection, w , and the twist angle, θ , are given by

$$\frac{\partial^2}{\partial z^2} \left[EI(z) \frac{\partial^2 w}{\partial z^2}(z, t) \right] + m(z) \frac{\partial^2 w}{\partial t^2}(z, t) + m(z) x_\theta(z) \frac{\partial^2 \theta}{\partial t^2}(z, t) = N(z, t) \quad (4)$$

$$\frac{\partial}{\partial z} \left[GJ(z) \frac{\partial \theta}{\partial z} \right] - m(z) x_\theta(z) \frac{\partial^2 w}{\partial t^2}(z, t) - I_\theta(z) \frac{\partial^2 \theta}{\partial t^2}(z, t) = -M_t(z, t) \quad (5)$$

where z is the vertical distance from the fixed support along the tail length, l_t , EI and GJ the bending and torsional stiffness of the tail section, m the mass per unit length, I_θ the mass-moment of inertia per unit length about the elastic axis, x_θ the distance between the elastic axis and inertia axis, N the normal force per unit length and M_t the twisting moment per unit length. The characteristic parameters for the dimensionless equations are c^* , a_∞^* , ρ_∞^* and c^*/a_∞^* for the length, speed, density and time; where c^* is the delta wing root-chord length, a_∞^* the freestream speed of sound and ρ_∞^* the freestream air density. The geometrical and natural boundary conditions on w and θ are given by

$$w(0, t) = \frac{\partial w}{\partial z}(0, t) = \frac{\partial^2 w}{\partial z^2}(l_t, t) = \frac{\partial}{\partial z} \left[EI(l_t) \frac{\partial^2 w}{\partial z^2}(l_t, t) \right] = 0 \quad (6)$$

$$\theta(0, t) = \frac{\partial \theta}{\partial z}(l_t, t) = 0 \quad (7)$$

The solution of Eqs. (4) and (5) are given by

$$w(z, t) = \sum_{i=1}^{\bar{I}} \phi_i(z) q_i(t) \quad (8)$$

$$\theta(z, t) = \sum_{j=\bar{I}+1}^M \phi_j(z) q_j(t) \quad (9)$$

where ϕ_i and ϕ_j are comparison functions satisfying the free-vibration modes of bending and torsion, respectively, and q_i and q_j are generalized coordinates for bending and torsion, respectively. In this paper, the number of bending modes, \bar{I} , is six and the number of torsion modes, $M - \bar{I}$, is also six. Substituting Eqs. (8) and (9) into Eqs. (4) and (5) and using the Galerkin method along with integration by parts and the boundary conditions, Eqs (6) and (7), we get the following equation for the generalized coordinates q_i and q_j in matrix form:

$$\begin{bmatrix} M_{11} & M_{12} \\ M_{21} & M_{22} \end{bmatrix} \begin{pmatrix} \ddot{q}_i \\ \ddot{q}_j \end{pmatrix} + \begin{bmatrix} K_{11} & 0 \\ 0 & K_{22} \end{bmatrix} \begin{pmatrix} q_i \\ q_j \end{pmatrix} = \begin{pmatrix} \hat{N}_1 \\ \hat{N}_2 \end{pmatrix} ; i = 1, 2, \dots, \bar{I} ; j = \bar{I} + 1, \dots, M \quad (10)$$

where

$$\begin{aligned} M_{11} &= \int_0^{l_t} m \phi_r \phi_i dz \\ M_{12} &= M_{21} = \int_0^{l_t} m x_\theta \phi_r \phi_j dz \\ M_{22} &= \int_0^{l_t} I_\theta \phi_s \phi_j dz \end{aligned} \quad (11)$$

$$\begin{aligned} K_{11} &= \int_0^{l_t} EI \frac{d^2 \phi_r}{dz^2} \frac{d^2 \phi_i}{dz^2} dz \\ K_{22} &= \int_0^{l_t} GJ \frac{d \phi_s}{dz} \frac{d \phi_j}{dz} dz \end{aligned} \quad (12)$$

$$\begin{aligned} \hat{N}_1 &= \int_0^{l_t} \phi_r N dz \\ \hat{N}_2 &= \int_0^{l_t} \phi_s M_t dz \end{aligned} \quad (13)$$

Similar aeroelastic equations were developed for sonic analysis of wing flutter by Strganac¹⁵. The numerical integration of Eqs. (11)-(13) is obtained using the trapezoidal method with 125 points to improve the accuracy of integrations. The solution of Eq. (10), for q_i ; $i = 1, 2, \dots, \bar{I}$, and q_j ; $j = \bar{I} + 1, \dots, M$, is obtained using the Runge-Kutta scheme. Next, w , and θ are obtained from Eqs. (8) and (9).

Grid Displacement Equations:

Once w and θ are obtained at the $n + 1$ time step, the new grid coordinates are obtained using simple interpolation equations. In these equations, the twin tail bending displacements, $w_{i,j,k}^{n+1}$, and their displacement through the torsion angle, $\theta_{i,j,k}^{n+1}$ are interpolated through cosine functions.

Boundary and Initial Conditions:

Boundary conditions consist of conditions for the fluid flow and conditions for the aeroelastic bending and torsional deflections of the twin tail. For the fluid flow, the Riemann-invariant boundary conditions are enforced at the inflow and outflow boundaries of the computational domain. At the plane of geometric symmetry, periodic boundary conditions are specified with the exception of grid points on the tail. On the wing surface, the no-slip and no-penetration conditions are enforced and $\frac{\partial p}{\partial n} = 0$. On the tail surface, the no-slip and no-penetration conditions for the relative velocity components are enforced (points on the tail surface are moving). The normal pressure gradient is no longer equal to zero due to the acceleration of the grid points on the tail surface. This equation becomes $\frac{\partial p}{\partial n} = -\rho \bar{a}_t \cdot \hat{n}$, where \bar{a}_t is the acceleration of a point on the tail and \hat{n} is the unit normal.

Initial conditions consist of conditions for the fluid flow and conditions for the aeroelastic deflections of the twin tail. For the fluid flow, the initial conditions correspond to the freestream conditions with no-slip and no-penetration conditions on the wing and tail. For the aeroelastic deflections of the tail, the initial conditions for any point on the tail are that the displacement and velocity are zero, $w(z, 0) = 0$, $\frac{\partial w}{\partial t}(z, 0) = 0$, $\theta(z, 0) = 0$ and $\frac{\partial \theta}{\partial t}(z, 0) = 0$.

METHOD OF SOLUTION

The first step is to solve for the fluid flow problem using the vortex-breakdown conditions and keeping the tail as a rigid beam. Navier-Stokes equations are solved using the implicit, flux-difference splitting finite-volume scheme. The grid speed $\frac{\partial \xi^m}{\partial t}$ is set equal to zero in this step. This step provides the flow field solution along with the pressure differences across the tails. The pressure differences are used to generate the normal force and twisting moment per unit length of each tail. Next, the aeroelastic equations are used to obtain the twin tail deflections, $w_{i,j,k}$ and $\theta_{i,j,k}$. The grid displacement equations are then used to compute the new grid coordinates. The metric coefficient of the coordinate Jacobian matrix are updated as well as the grid speed, $\frac{\partial \xi^m}{\partial t}$. This computational cycle is repeated every time step.

COMPUTATIONAL APPLICATIONS AND DISCUSSION

Twin Tail-Delta Wing Configuration:

The twin tail-delta wing configuration consists of a 76°-swept back, sharp-edged delta wing (aspect ratio of one) and dynamically scaled flexible twin tails similar to those used by Washburn, et. al.⁷. The vertical tails are oriented normal to the upper surface of the delta wing and have a centerline sweep of 53.5°. A multi-block grid consisting of 4 blocks is used for the solution of the problem. The first block is a O-H grid for the wing and upstream region, with 101X50X54 grid points in the wrap around, normal and axial directions, respectively. The second block is a H-H grid for the inboard region of the twin tails, with 23X50X13 grid points in the wrap around, normal and axial directions, respectively. The third block is a H-H grid for the outboard region of the twin tails, with 79X50X13 grid points in the wrap around, normal and axial directions, respectively. The fourth block is a O-H grid for the downstream region of the twin tails, with 101X50X25 grid points in the wrap around, normal and axial directions, respectively. Figure 1 shows the grid topology and a front view blow-up of the twin tail-delta wing configuration.

Each tail is made of a single Aluminum spar and Balsa wood covering. The Aluminum spar has a taper ratio of 0.3 and a constant thickness of 0.001736. The chord length at the root is 0.03889 and at the tip is 0.011667, with a span length of 0.2223. The Aluminum spar is constructed from 6061-T6 alloy with density, ρ , moduli of elasticity and rigidity, E and G , of 2693 kg/m³, 6.896X10¹⁰ N/m² and 2.5925X10¹⁰ N/m²; respectively. The corresponding dimensionless quantities are 2198, 4.595 × 10⁵ and 1.727 × 10⁵; respectively.

The Balsa wood covering has a taper ratio of 0.23 and aspect ratio of 1.4. The chord length at the root is 0.2527 and at the tip is 0.058, with a span length of 0.2223. The Balsa thickness decreases gradually from 0.0211 at the tail root to 0.0111 at the tail midspan and then constant thickness of 0.0111 is maintained to the tail tip. The tail cross section is a semi-diamond shape with bevel angle of 20°. The Balsa density, moduli of elasticity and rigidity, E and G , are 179.7 kg/m³, 6.896X10⁸ N/m² and

$2.5925 \times 10^8 \text{ N/m}^2$; respectively. The corresponding dimensionless quantities are 147, 4.595×10^3 and 1.727×10^3 ; respectively. Figure 2 shows a schematic of the tail used in this study. The tails are assumed to be magnetically suspended and the leading edge of the tail root is positioned at $x/c = 1.0$, measured from the wing apex. The configuration is pitched at a wide range of angles of attack 15° to 40° , and the freestream Mach number and Reynolds number are 0.3 and 1.25×10^6 ; respectively.

The configuration is investigated for two spanwise positions of the twin tails; the inboard location and the outboard location corresponding to a separation distance between the twin tails of 33% and 78% of the wing span; respectively.

RESULTS AND DISCUSSION

Parametric Study:

Figure 3 shows the effect of the spanwise tail location on the configuration lift coefficient as a function of angle of attack. The lift coefficient is almost insensitive to the spanwise tail location. The figure also shows a very close agreement with the experimental results. Figures 4a and 4b show the mean root bending moments and the RMS root bending moments as a function of angle of attack, respectively. Positive moments correspond to an outward force on the tails. The mean value of the moment increases with the angle of attack and then reduces at high angles. The RMS value of the moment also increases with the angle of attack. The buffet loads in terms of the root bending moment are greatest with the tails in the inboard position; almost throughout the whole range of angle of attack. The agreement with the experimental data is good. The discrepancies in the results are attributed to the fact that the structural model of the tail is not fully identical to the experimental model. The additional Ballast weights in the tails of the experimental model is not modeled, and Washburn in his experimental work used one flexible tail and one rigid tail while we are using two flexible tails. In the experimental work, the presence of a flexible tail was found to affect the loads and pressures on the other rigid tail.

Figure 5 shows the normalized RMS of the surface pressures (p/q_∞) on the inner and outer

surfaces of the inboard tails at the specified five locations shown in Fig. 2. The experimental results of Washburn⁷ are also shown. The RMS surface pressures in all locations increases with the increase of angle of attack, where the vortex breakdown moves upstream of the tails. The outer surface of the tails experience larger RMS pressure levels than those of the inner surface. On the inner surface, the nearly tip point (location 1) experiences larger pressure levels than the nearly root point (location 5). On the outer surface, the nearly root point experiences larger pressure levels than those of the nearly tip point. Figure 6 shows the normalized RMS of the surface pressures on the inner and outer surfaces of the outboard tails at the specified five locations. The observations are similar to the case of inboard tails, except that the inner surface RMS pressure levels are larger than those of the outer surface levels of the outboard tail case. The inboard tails experience larger pressure levels than those of the outboard tails. These results are in good qualitative agreement with the experimental data. The discrepancies between the two results are, again, attributed to the reasons stated before.

Detailed Results at $\alpha = 25^\circ$:

Figures 7 and 8 show front views for the total pressure contours on the wing surface and in cross flow planes at $x = 1.03$ and $x = 1.22$, and the instantaneous streamlines of the inboard tail position. The vortex cores are almost symmetric at both locations, and they are totally outboard of the twin tail. The cores are moved upward as the flow traveled downstream. Smaller size vortex cores appear underneath the primary wing vortex and it becomes larger in size as it travels downstream. These are the tail vortices observed by Washburn⁷. The tail vortices exist at the outer surfaces of the tails and they are rotating in the opposite direction to those of the primary wing vortices. Figure 9 shows the distribution of the total structural deflection and the root bending moment for the left and right tails. The tails deflections are in first, second and third mode shapes. Both deflections and root bending moment increase rapidly and reach periodic response around $t^* = 20$.

Figures 10 and 11 show front views for the total pressure contours on the wing surface and in cross flow planes at $x = 1.03$ and $x = 1.22$, and the instantaneous streamlines of the outboard tail

position. The tails cut through the vortex breakdown flow of the leading-edge vortex cores. The flow is almost symmetric. The tail vortices are also outboard of the tails but larger in size than those of the inboard tails case. The location of the vortex core with respect to the tail produces an increase in the aerodynamic damping, causing the tail deflection to decrease. The tail vortices are also shown to rotate in the opposite direction to those of the primary wing vortices. Figure 12 shows the distribution of the total structural deflection and the root bending moment for the left and right tails. The levels of deflection are lower than those of the inboard tails position. The frequency of the root bending moment is higher than that of the inboard tail case, and the deflections seem to be damped and stable at this angle of attack. Figure 13 shows the distribution of the surface pressure coefficient covering the wing from $x = 0.3$ to $x = 1.0$. Typical turbulent flow distribution are observed, where the largest suction peaks are pronounced at the position of the wing vortex cores. It is obvious that the vortex breakdown does not occur over the wing surface at this angle of attack.

Detailed results at $\alpha = 40^\circ$:

Figures 14 and 15 show front views for the total pressure contours on the wing surface and in cross flow planes at $x = 1.03$ and $x = 1.22$, and the instantaneous streamlines for the inboard tail position. The primary leading-edge vortex cores experience a breakdown at about $x = 0.28$, and the vortex breakdown flow becomes large in size, and partially covers the region inboard the twin tails. The vertical position of the vortex cores is higher than that at $\alpha = 25^\circ$, and it moves upward as the flow travels downstream. The tail vortices are more distinct than those of $\alpha = 25^\circ$. Figure 16 shows the distribution of the total structural deflection and the root bending moment for the left and right tails. The two tails are deflected in one direction only in first, second and third mode shapes. The frequency of the root bending moment is lower than that of the case of $\alpha = 25^\circ$. Periodic responses have not been reached within the computational time covered.

Figures 17 and 18 show front views for the total pressure contours on the wing surface and in cross flow planes at $x = 1.03$ and $x = 1.22$, and the instantaneous streamlines for the outboard

tail position. The tails cut through the vortex breakdown flow of the leading-edge vortex cores, and the breakdown is larger in size than that of the case of $\alpha = 25^\circ$. The vortex cores are moved more upward than that of the case of $\alpha = 25^\circ$ and continue moving upward as the flow travels downstream. Also, the tail vortex is larger in size than that of the $\alpha = 25^\circ$ case. This also would increase the aerodynamic damping on the tails. The vortex breakdown flow is almost symmetric. Figure 19 shows the distribution of the total structural deflection and the root bending moment for the left and right tails. The two tails are deflected in one direction only in first and second mode shapes. The frequency of deflection is the same as that of the inboard tail case but lower than that of the case of $\alpha = 25^\circ$. The load levels are twice as high as those of the case of $\alpha = 25^\circ$. Figure 20 shows the distribution of the surface pressure coefficient covering the wing from $x = 0.3$ to $x = 1.0$. Suction peaks observed over the wing are higher than those of the case of $\alpha = 25^\circ$. It is indicated from the distribution that vortex breakdown covers most of the wing. After 9,600 time steps, the distribution changed completely due to the upstream effect of the tail deflections, and the vortex breakdown covers the whole wing.

Figures 21 and 22 show the tail surface flow on the inner and outer surfaces of the outboard tails, respectively, for $\alpha = 20^\circ, 30^\circ$ and 40° . The flow separation line is shown to start from the leading edge of the root to the middle of the tail tip. The separation line moves downstream as the angle of attack increases. The tail vortex attachment line is observed on the outer surface of the tail near and parallel to the tail root and along the tail root. This is more clear at higher angles of attack, $\alpha = 30^\circ$ and 40° . These results are in complete agreement with the experimental data of Washburn⁷.

CONCLUDING REMARKS

The computational results of the FTNS3D code of the present paper and the experimental data of Washburn, et. al. are in very good agreement. In general, the RMS levels of the loads increase as the angle of attack increases. However, the case of inboard tails at $\alpha = 25^\circ$ produces the largest buffet loads and deflections. The inboard location of the twin tails produces the

largest bending-torsion loads, deflections, frequencies and root bending moments when compared with the midspan and outboard locations. The frequencies of the loads and deflections of the tails decrease as the angle of attack increases.

ACKNOWLEDGMENT

This research work is supported under Grants No. NAG-1-994 and NAG-1-648 by the NASA Langley Research Center. The authors would like to recognize the computational resources provided by the NAS facilities at Ames Research Center and the NASA Langley Research Center.

REFERENCES

1. Sellers, W. L. III, Meyers, J. F. and Hepner, T. E., "LDV Survey Over a Fighter Model at Moderate to High Angle of Attack," SAE Paper 88-1448, 1988.
2. Erickson, G. E., Hall, R. M., Banks, D. W., Del Frate, J. H., Shreiner, J. A., Hanley, R. J. and Pulley, C. T., "Experimental Investigation of the F/A-18 Vortex Flows at Subsonic Through Transonic Speeds," AIAA 89-2222, 1989.
3. Wentz, W. H., "Vortex-Fin Interaction on a Fighter Aircraft," AIAA 87-2474, AIAA Fifth Applied Aerodynamics Conference, Monterey, CA August 1987.
4. Lee, B. and Brown, D., "Wind Tunnel Studies of F/A-18 Tail Buffet," AIAA 90-1432, 1990.
5. Cole, S. R., Moss, S. W. and Dogget, R. V., Jr., "Some Buffet Response Characteristics of a Twin-Vertical-Tail Configuration," NASA TM-102749, October 1990.
6. Bean, D. E. and Lee, B. H. K., "Correlation of Wind Tunnel and Flight Test Data for F/A-18 Vertical Tail Buffet," AIAA 94-1800-CP, 1994.
7. Washburn, A. E., Jenkins, L. N. and Ferman, M. A., "Experimental Investigation of Vortex-Fin Interaction," AIAA 93-0050, AIAA 31st ASM, Reno, NV, January 1993.
8. Kandil, O. A., Kandil, H. A. and Massey, S. J., "Simulation of Tail Buffet Using Delta Wing-Vertical Tail Configuration," AIAA 93-3688-CP, AIAA Atmospheric Flight Mechanics Conference, Monterey, CA August 1993, pp. 566-577.
9. Kandil, O. A., Massey, S. J., and Kandil, H. A., "Computations of Vortex-Breakdown Induced Tail Buffet Undergoing Bending and Torsional Vibrations," AIAA 94-1428-CP, AIAA/ASME/ASCE/ASC Structural, Structural Dynamics and Material Conference, SC April 1994, pp. 977-993.
10. Kandil, O. A., Massey, S. J. and Sheta, E. F., "Structural Dynamics/CFD Interaction for Computation of Vertical Tail Buffet," International Forum on Aeroelasticity and Structural Dynamics, Royal Aeronautical Society, Manchester, U.K., June 26-28, 1995, pp. 52.1-52.14. Also published in Royal Aeronautical Journal, August/September 1996, pp. 297-303.
11. Kandil, O. A., Sheta, E. F. and Massey, S. J., "Buffet Responses of a Vertical Tail in Vortex Breakdown Flows," AIAA 95-3464-CP, AIAA Atmospheric Flight Mechanics Conference, Baltimore, MD, August 7-9, 1995, pp. 345-360.
12. Kandil, O. A., Sheta, E. F. and Massey, S. J., "Twin Tail/Delta Wing Configuration Buffet Due to Unsteady Vortex Breakdown Flow," AIAA 96-2517-CP, 14th AIAA Applied Aerodynamics Conference, New Orleans, LA, June 18-20, 1996, pp. 1136-1150.
13. Kandil, O. A., Massey, S. J. and Sheta, E. F., "Aerostructural Vortical Flow Interactions With Applications to F/A-18 and F-117 Tail Buffet," High-Angle-of-Attack Technology Conference, NASA Langley Research Center, Hampton, VA, September 17-19, 1996.
14. Baldwin, B. and Lomax, H., "Thin-Layer Approximation and Algebraic Model for Separated Turbulent Flows," AIAA Paper 78-0257, January, 1978.
15. Straganac, T. W., "A Numerical Model of Unsteady, Subsonic Aeroelastic Behavior," NASA Technical Memorandum 100487, December 1987.

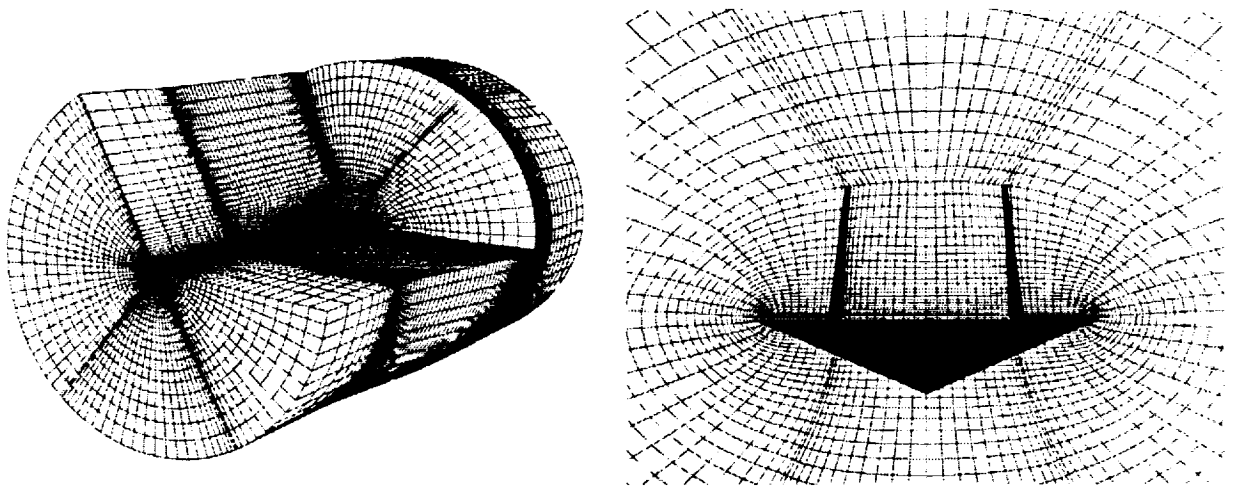


Figure 1: Three-dimensional grid topology and blow-up of the twin tail-delta wing configuration (the tails are in midspan position).

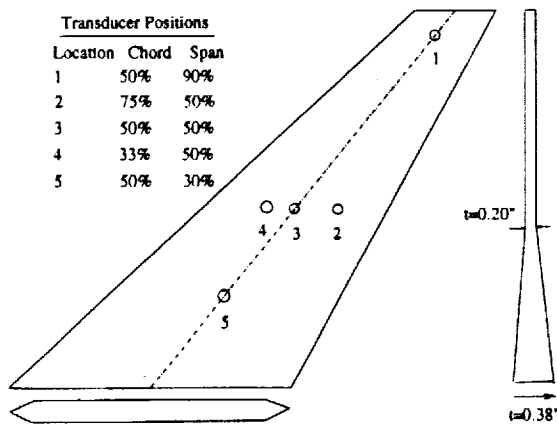


Figure 2: Schematic of the tail

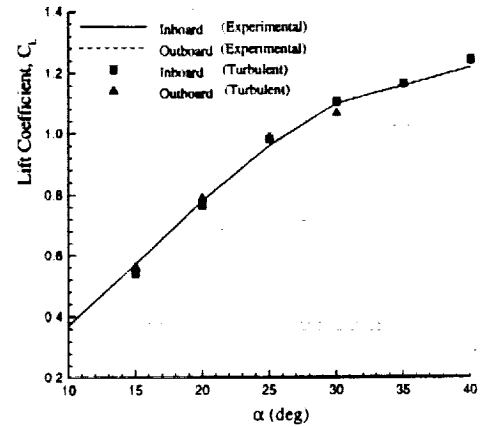
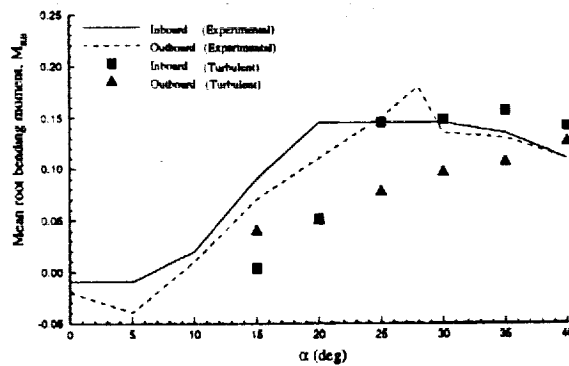
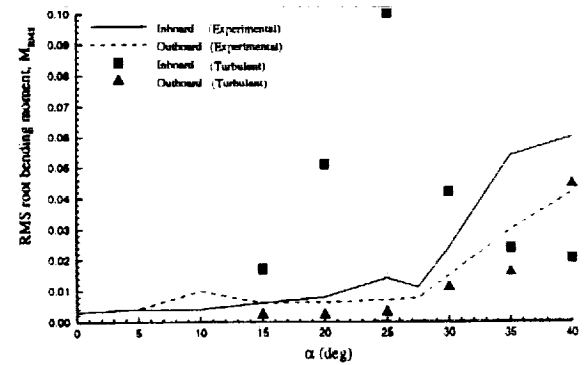


Figure 3: Effect of spanwise tail location on the lift coefficient curve.

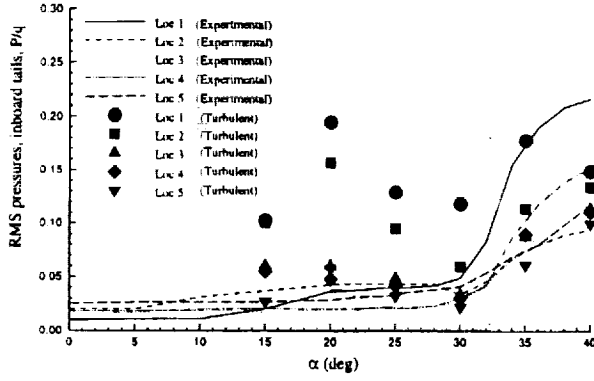


(a) Mean root bending moment

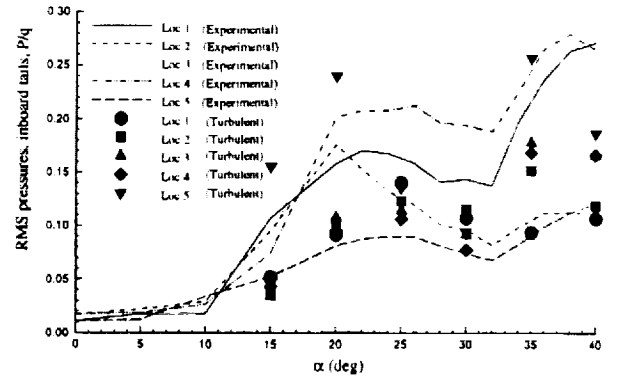


(b) RMS root bending moment

Figure 4: Mean and RMS root bending moment on the flexible tails.

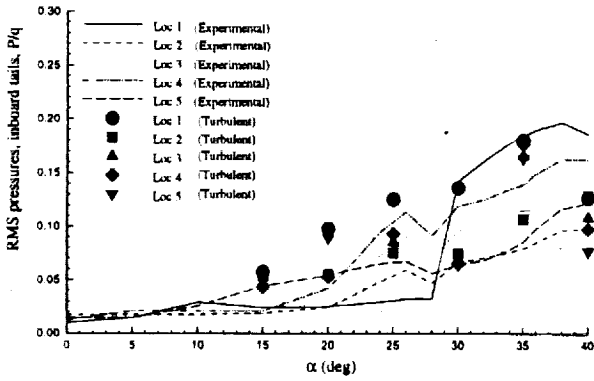


(a) Inner surface

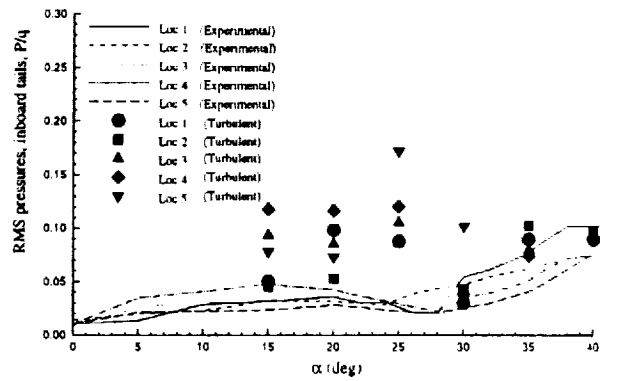


(b) Outer surface

Figure 5: RMS pressures at the specified five locations on the tail, inboard position.



(a) Inner surface

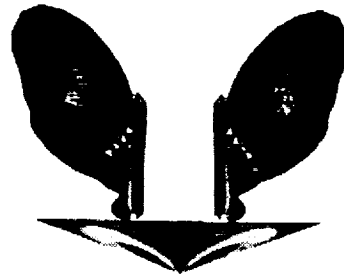


(b) Outer surface

Figure 6: RMS pressures at the specified five locations on the tail, outboard position.

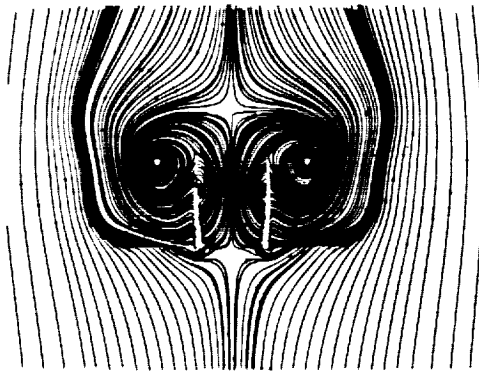


(a) $x = 1.03$

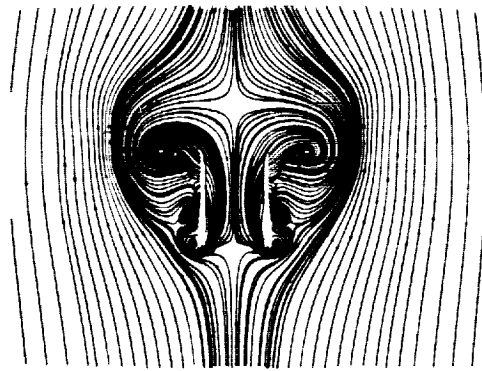


(b) $x = 1.22$

Figure 7: Snap shots of total pressure in a cross-flow planes, (Inboard position). $M_\infty = 0.3$, $\alpha = 25^\circ$, $R_e = 1.25 \times 10^6$.

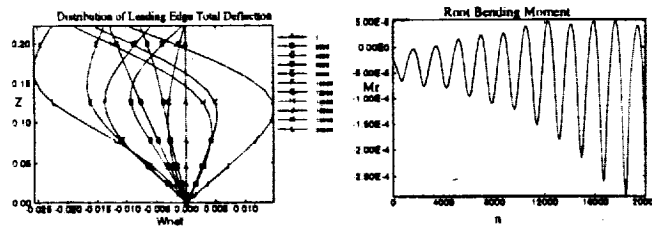


(a) $x = 1.03$

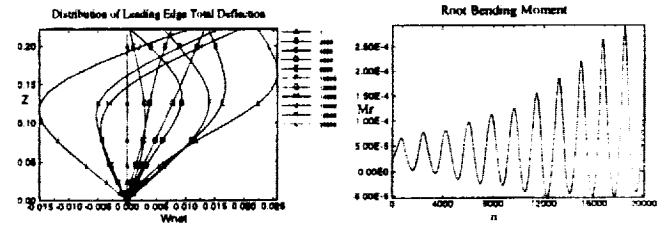


(b) $x = 1.22$

Figure 8: Snap shots of instantaneous streamlines in a cross-flow planes, (Inboard position). $M_\infty = 0.3$, $\alpha = 25^\circ$, $R_e = 1.25 \times 10^6$.

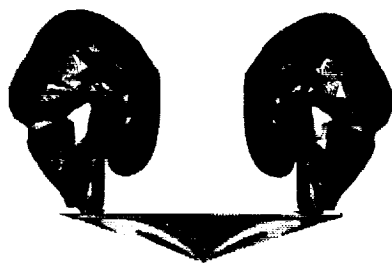


(a) Left tail

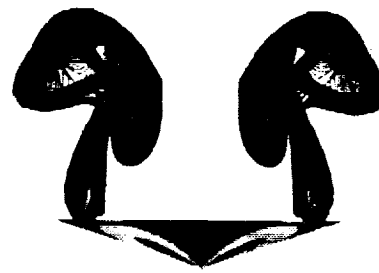


(b) Right tail

Figure 9: Total structural deflections and root bending moment for an uncoupled bending-torsion case. $M_\infty = 0.3$, $\alpha = 25^\circ$, $R_e = 1.25 \times 10^6$, (Inboard position).



(a) $x = 1.03$



(b) $x = 1.22$

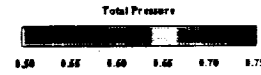
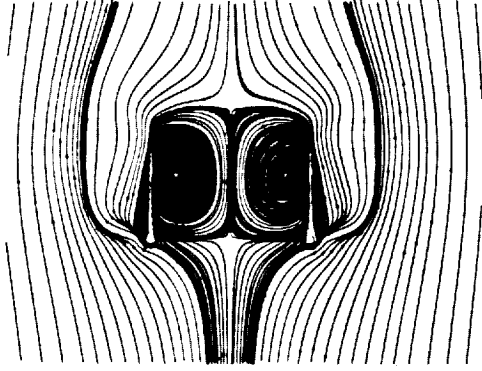
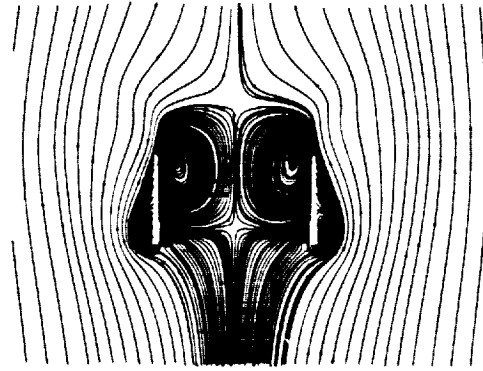


Figure 10: Snap shots of total pressure in a cross-flow planes, (Outboard position). $M_\infty = 0.3$, $\alpha = 25^\circ$, $R_e = 1.25 \times 10^6$.

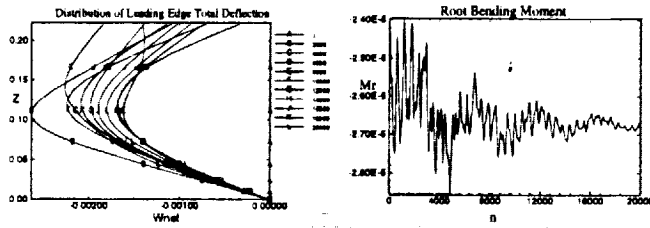


(a) $x = 1.03$

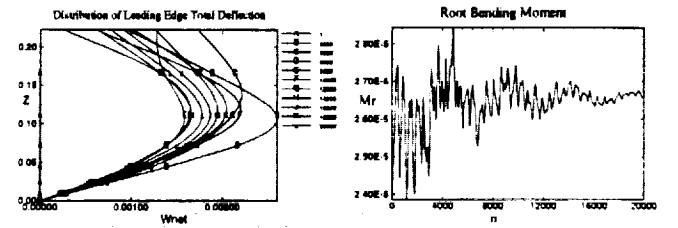


(b) $x = 1.22$

Figure 11: Snap shots of instantaneous streamlines in a cross-flow planes, (Outboard position). $M_\infty = 0.3$, $\alpha = 25^\circ$, $R_e = 1.25 \times 10^6$.

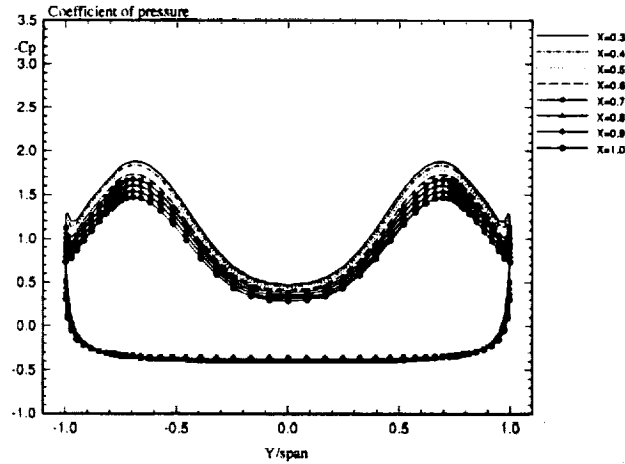


(a) Left tail

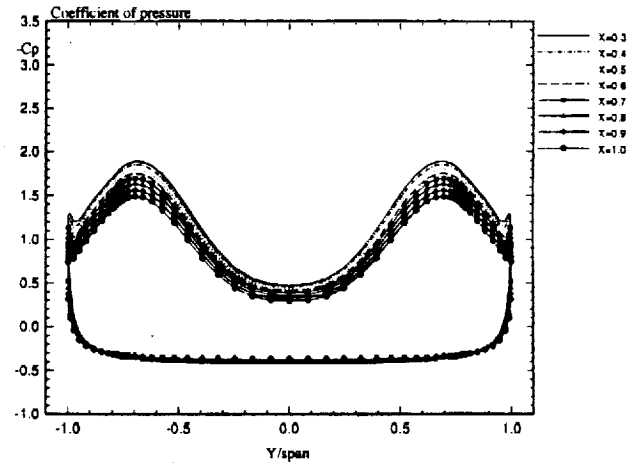


(b) Right tail

Figure 12: Total structural deflections and root bending moment for an uncoupled bending-torsion case. $M_\infty = 0.3$, $\alpha = 25^\circ$, $R_e = 1.25 \times 10^6$, (Outboard position).

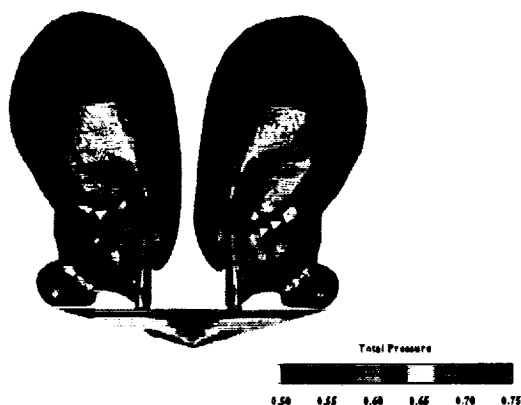


(a) Initial conditions

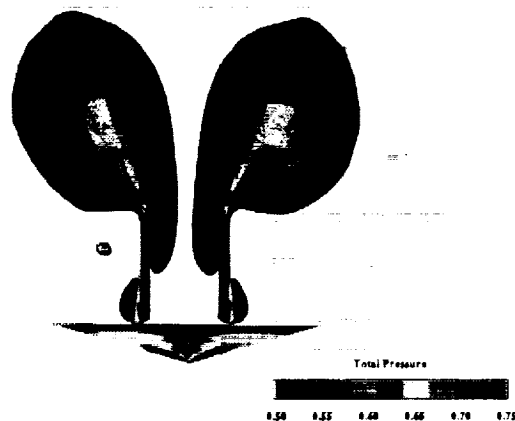


(b) Uncoupled case, after $it = 9,600$

Figure 13: Distribution of Coefficient of pressure. Outboard position, $M_\infty = 0.3$, $\alpha = 25^\circ$, $R_e = 1.25 \times 10^6$.

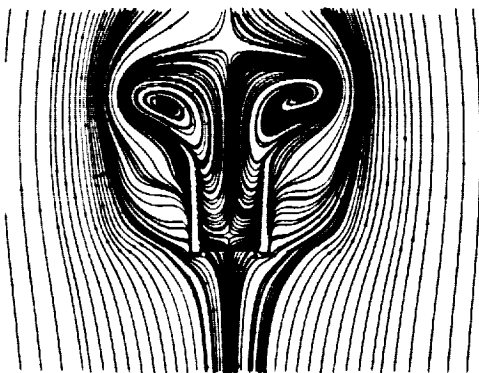


(a) $x = 1.03$

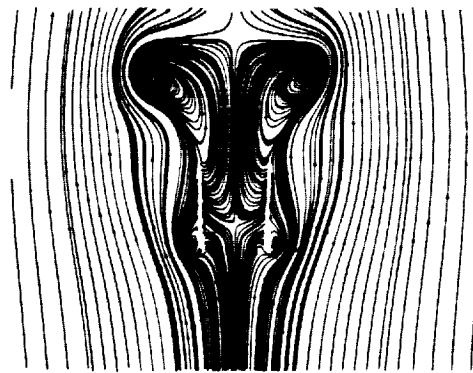


(b) $x = 1.22$

Figure 14: Snap shots of total pressure in a cross-flow planes, (Inboard position). $M_\infty = 0.3$, $\alpha = 40^\circ$, $R_e = 1.25 \times 10^6$.

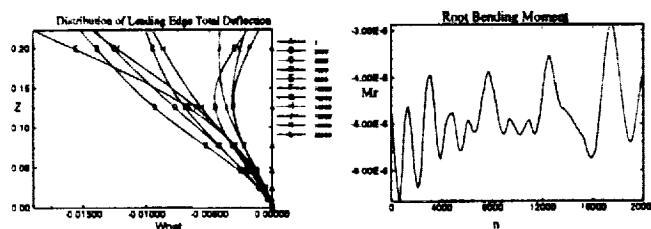


(a) $x = 1.03$

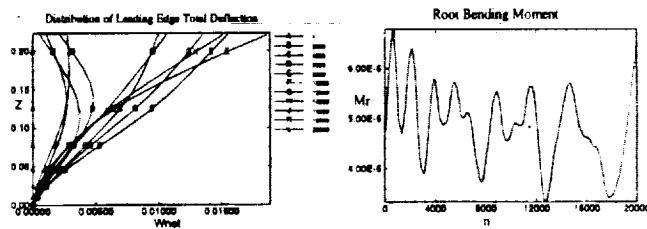


(b) $x = 1.22$

Figure 15: Snap shots of instantaneous streamlines in a cross-flow planes, (Inboard position). $M_\infty = 0.3$, $\alpha = 40^\circ$, $R_e = 1.25 \times 10^6$.

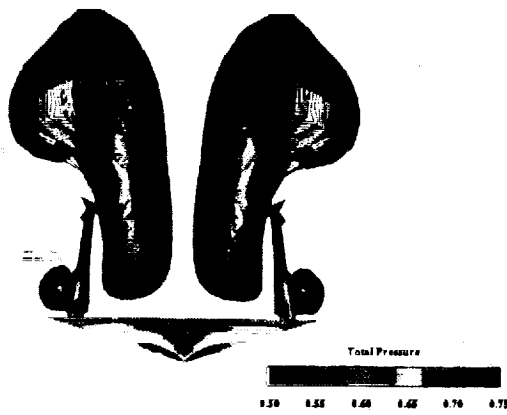


(a) Left tail

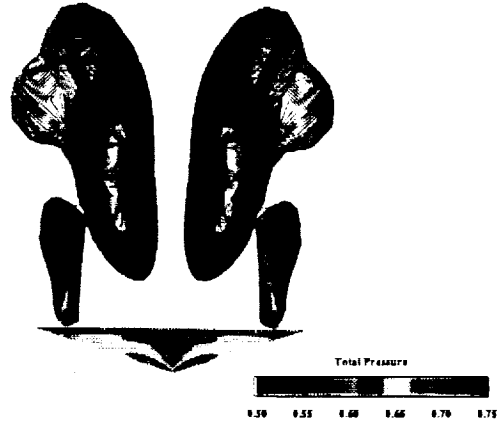


(b) Right tail

Figure 16: Total structural deflections and root bending moment for an uncoupled bending-torsion case. $M_\infty = 0.3$, $\alpha = 40^\circ$, $R_e = 1.25 \times 10^6$, (Inboard position).

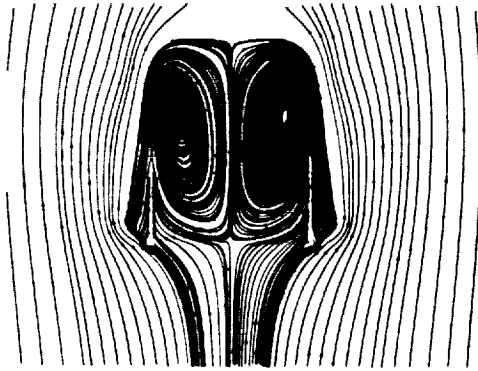


(a) $x = 1.03$

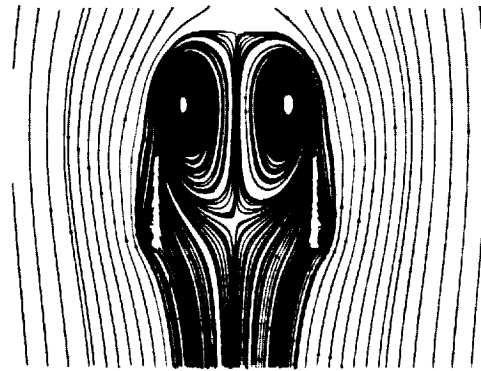


(b) $x = 1.22$

Figure 17: Snap shots of total pressure in a cross-flow planes, (Outboard position). $M_\infty = 0.3$, $\alpha = 40^\circ$, $R_e = 1.25 \times 10^6$.

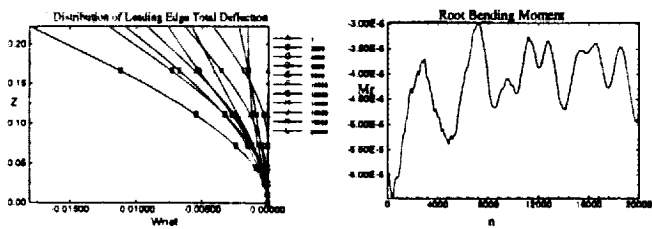


(a) $x = 1.03$

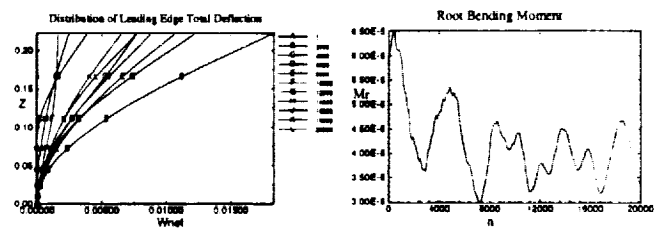


(b) $x = 1.22$

Figure 18: Snap shots of instantaneous streamlines in a cross-flow planes, (Outboard position). $M_\infty = 0.3$, $\alpha = 40^\circ$, $R_e = 1.25 \times 10^6$.

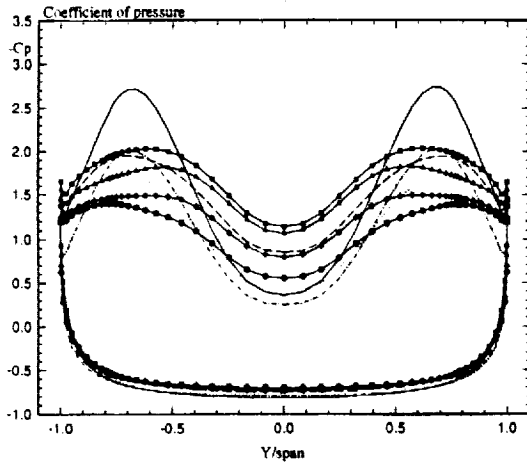


(a) Left tail

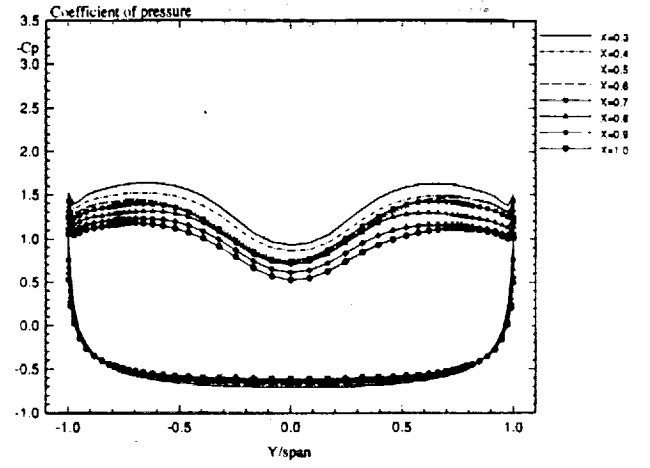


(b) Right tail

Figure 19: Total structural deflections and root bending moment for an uncoupled bending-torsion case. $M_\infty = 0.3$, $\alpha = 40^\circ$, $R_e = 1.25 \times 10^6$, (Outboard position).

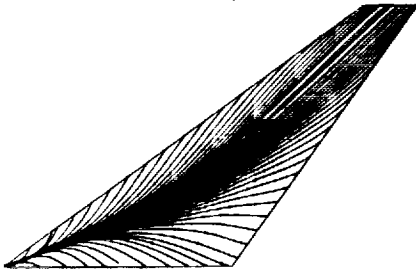


(a) Initial conditions

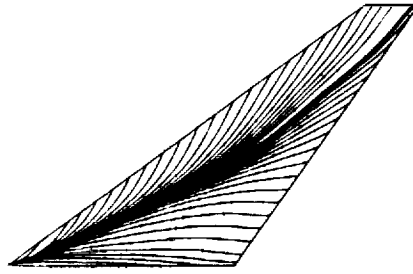


(b) Uncoupled case, after $it = 9,600$

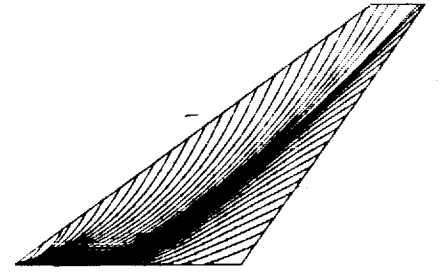
Figure 20: Distribution of Coefficient of pressure. Outboard position, $M_\infty = 0.3$, $\alpha = 40^\circ$, $R_e = 1.25 \times 10^6$.



(a) $\alpha = 20^\circ$

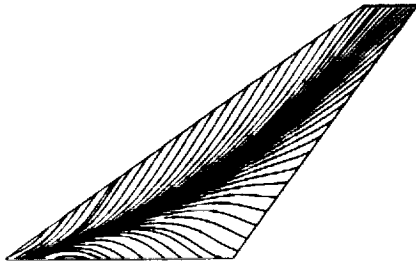


(b) $\alpha = 30^\circ$

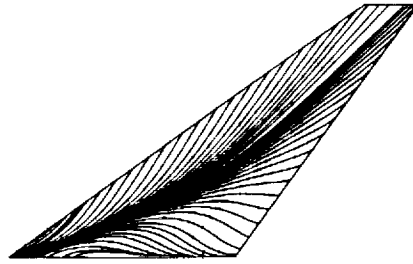


(c) $\alpha = 40^\circ$

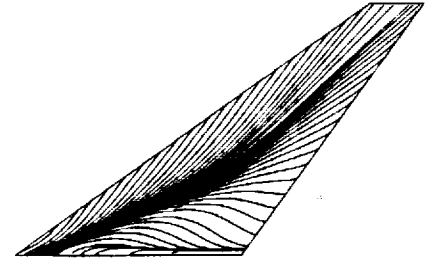
Figure 21: Tail surface flow, inner surface. Uncoupled case after $it = 9,600$, outboard tails.



(a) $\alpha = 20^\circ$



(b) $\alpha = 30^\circ$



(c) $\alpha = 40^\circ$

Figure 22: Tail surface flow, outer surface. Uncoupled case after $it = 9,600$, outboard tails.

SECOND SEMINAR ON RRDPAE'96

RECENT ADVANCES IN MULTIDISCIPLINARY AERONAUTICAL PROBLEMS OF FLUIDS/STRUCTURES/DYNAMICS INTERACTION

Osama A. Kandil*

Aerospace Engineering Department
Old Dominion University, Norfolk, Virginia 23529, USA

Abstract

Aeronautical problems and applications of multidisciplinary, time-dependent nature are addressed in this paper. Formulations of these problems, which include governing equations, boundary and initial conditions, are presented. For fluids/structures interaction problems, three sets of governing equations are used. These are the unsteady, Navier-Stokes (NS) equations, the aeroelastic equations of coupled or uncoupled bending and torsion equations and the grid displacement equations. The latter equations are used to move the computational grid due to the structural elastic deformations. For fluids/dynamics interaction problems, two sets of governing equations are used. These are the unsteady NS equations and the Euler equations of rigid-body dynamics. These sets of equations are sequentially solved time accurately using the upwind, flux-difference splitting scheme for the fluids equations and the four-stage Runge-Kutta scheme for the aeroelastic and dynamics equations. The grid displacement equations are algebraic equations which are solved to obtain the new grid coordinates.

Computational applications and validations cover delta wings/ twin tail configurations simulating the tail buffet problem and delta wings undergoing natural mode response in rolling oscillations simulating the wing rock problem. Validation of the computational results are also presented and discussed.

Introduction

The first multidisciplinary aeronautical problem is that of fluids/structures interaction. Vertical tails buffet represents a challenging aeronautical application in this area. Modern aircraft are designed to fly and maneuver high angles of attack and at high loading conditions. This is achieved, for example in the F/A-18 fighter, through the combination of a leading-edge extension (LEX) with a delta wing and the use of highly swept-back twin vertical tails. The LEX maintains lift at high angles of attack by generating a pair of vortices that trail aft over the top of the delta wings. The vortex entrains air over the vertical tails to maintain stability of the aircraft. This combination of LEX, delta wing and vertical tails leads to the aircraft excellent agility. However, at some flight conditions, the vortices emanating from the highly-swept LEX of the delta wing breakdown before reaching the vertical tails, which get bathed in a wake of unsteady highly-turbulent, swirling flow. The vortex-breakdown flow produces unsteady, unbalanced loads on the vertical tails which in turn produce severe buffet of the tails. The buffet loads result into premature fatigue failure of the tails.

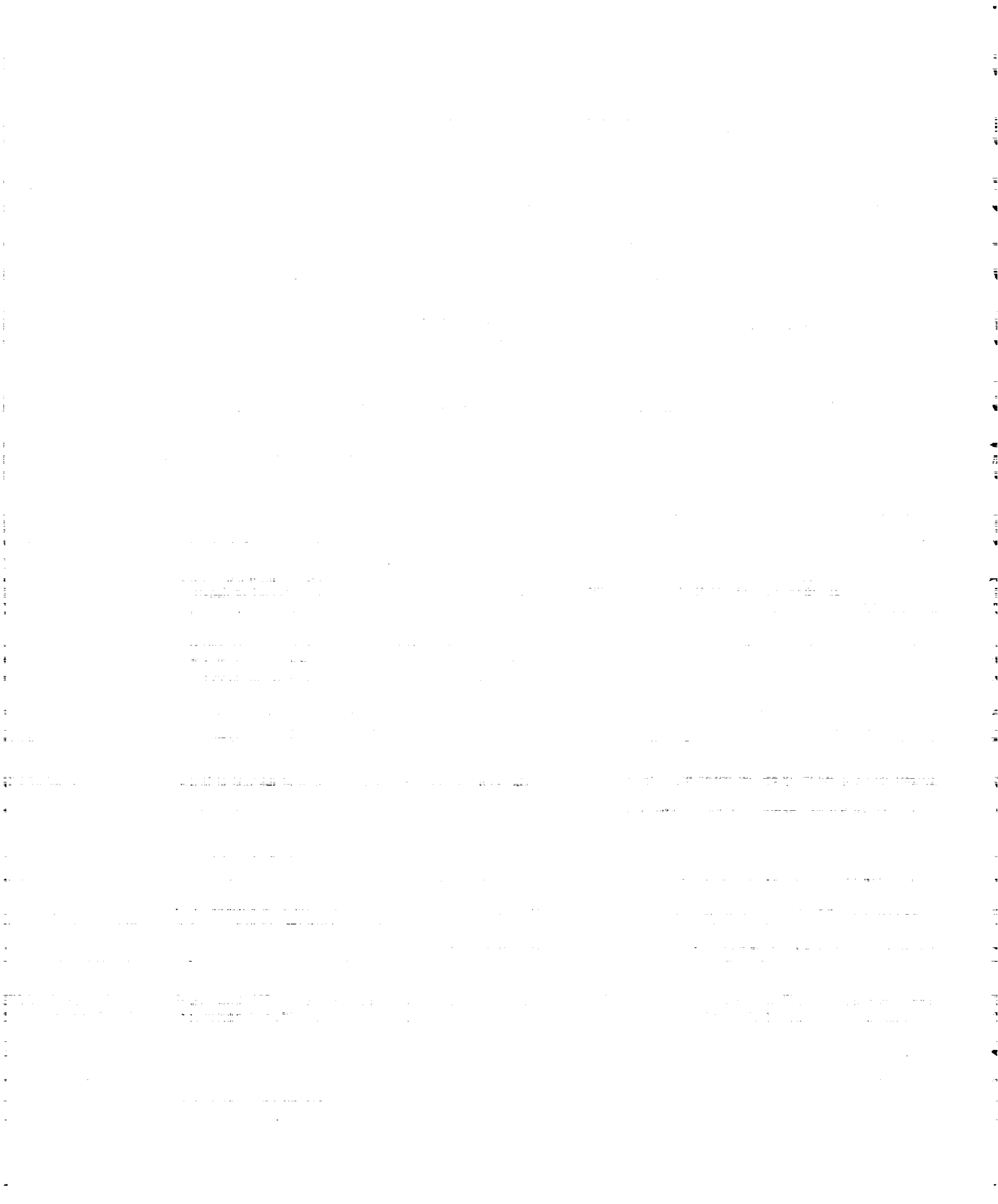
Experimental investigation of the vertical tail buffet of the F/A-18 models have been conducted by several investigators such as Sellers et al⁽¹⁾, Erickson et al⁽²⁾, Wentz⁽³⁾ and Lee and Brown⁽⁴⁾. These experiments showed that the vortex produced by the LEX of the wing breaks down ahead of the vertical tails at angles of attack of 25° and higher and that the breakdown flow produced unsteady loads on the vertical tails. Cole, Moss and Doggett⁽⁵⁾ tested a rigid, 1/6 size, full-span model of an F-18 airplane that was fitted with flexible vertical tails of two different stiffness. Vertical-tail buffet response results were obtained over the range of angle of attack from -10° to +40°, and over the range of Mach numbers from 0.3 to 0.95. Their results indicated that the buffet response occurred in the first bending mode, increased with increasing dynamic pressure and was larger at $M = 0.3$ than that at a higher Mach number.

An extensive experimental investigation has been conducted to study vortex-twin tail interaction on a 76° sharp-edged delta wing with vertical twin-tail configuration by Washburn, Jenkins and Ferman⁽⁶⁾. The vertical twin tails were placed at nine locations behind the wing. The experimental data showed that the aerodynamic loads are more sensitive to the chordwise tail location than its spanwise location. As the tails were moved toward the vortex core, the buffet response and excitation were reduced. Although the tail location did not affect the vortex core trajectories, it affected the location of vortex-core breakdown. Moreover, the investigation showed that the presence of a flexible tail can affect the unsteady pressures on the rigid tail on the opposite side of the model. In a recent study by Bean and Lee⁽⁷⁾ tests were performed on a rigid 6% scale F/A-18 in a trisonic blowdown wind tunnel over a range of angle of attack and Mach number. The flight data was reduced to a non-dimensional buffet excitation parameter, for each primary mode. It was found that buffeting in the torsional mode occurred at a lower angle of attack and at larger levels compared to the fundamental bending mode.

Tail buffet studies were also conducted on a full-scale, production model F/A-18 fighter aircraft in the 80-by-120 foot wind tunnel at NASA Ames Research Center by Meyn and James⁽⁸⁾ and Pettit, Brown and Pendleton⁽⁹⁾. The test matrix covered an angle of attack range of 18° to 50° and a side-slip range of -16° to 16° with wind speed up to 100 Knots. The maximum speed corresponds to a Reynolds number of 1.23×10^7 and a Mach number of 0.15.

Kandil, Kandil and Massey⁽¹⁰⁾ presented the first successful computational simulation of the vertical flexible tail buffet using a delta wing-vertical tail configuration. A 76° sharp-edged delta wing has been used along with a single rectangular vertical tail which was placed aft the wing along the plane of geometric symmetry. The flexible tail was allowed to oscillate in bending modes. The flow conditions and wing angle of attack have been selected to produce an unsteady vortex-breakdown flow. Unsteady vortex breakdown of leading-edge

*Professor, Eminent Scholar and Department Chairman



vortex cores was captured, and unsteady pressure forces were obtained on the tail.

Kandil, Massey and Kandil⁽¹¹⁾ extended the technique used in Ref. 10 to allow the vertical tail to oscillate in both bending and torsional modes. The total deflections and the frequencies of deflections and loads of the coupled bending-torsion case were found to be one order of magnitude higher than those of the bending case only. Also, it has been shown that the tail oscillations change the vortex breakdown locations and the unsteady aerodynamic loads on the wing and tail.

Kandil, Massey and Sheta⁽¹²⁾ studied the effect of coupling and uncoupling the bending and torsional modes for a long computational time, and the flow Reynolds number on the buffet response, of a single rectangular flexible tail. It has been shown that the coupled response produced higher deflection than that of the uncoupled response. Moreover, the response of the coupled case reached periodicity faster than that of the uncoupled case. It has also been shown that the deflections of the low-Reynolds number case were substantially lower than that of the high Reynolds number case.

In a recent paper by Kandil, Sheta and Massey⁽¹³⁾, the buffet response of a single swept-back vertical flexible tail in transonic flow at two angles of attack (20° , 28°) has been studied. It has been shown that the aerodynamic loads and bending-torsion deflections of the tail never reached periodic response and that the loads were one order of magnitude lower than those of Ref. 12 of the subsonic flow.

In a very recent paper by Kandil, Sheta and Massey⁽¹⁴⁾, the buffet response of the F/A-18 twin tails were considered. The configuration consisted of a 76° -swept back, sharp-edged delta wing and a trailing-edge-extension on which the F/A-18 twin tails were attached as cantilevers. A multi-block grid was used to solve the problem for two lateral locations of the twin tails: a midspan location and an inboard location.

The second multidisciplinary aeronautical problem is that of fluids/dynamics interaction. Wing rock of highly swept-back wings represents another challenging aeronautical application in this area.

One frequently encountered lateral instability which limits combat effectiveness for all fighter aircraft is the limit-cycle rolling oscillation phenomenon known as wing rock. In moderate to high angle-of-attack dynamic motion, wing rock is driven by strong, concentrated vortices originating from the leading edges of highly swept wings. Wing rock can occur at subsonic airspeeds at angles of attack in the vicinity of stall, and at moderate angles of attack in the transonic regime as a result of shock-wave/boundary-layer interactions on the wing. Generally, the onset of wing rock can be caused by a number of different aerodynamic phenomena and is attributed to a loss of stability in the lateral/directional mode.

To understand the wing rock phenomenon, experimental investigations have been carried out on simplified delta-wing geometries with a single degree of freedom in roll. By avoiding the complexity of complete aircraft geometries, research can focus on the relevant flow physics. Experimental data typically consists of flow visualization, time-dependent forces and moments and more recently, time-dependent surface pressure data. The time-dependent pressure data provides additional information that allows for more detailed understanding of the

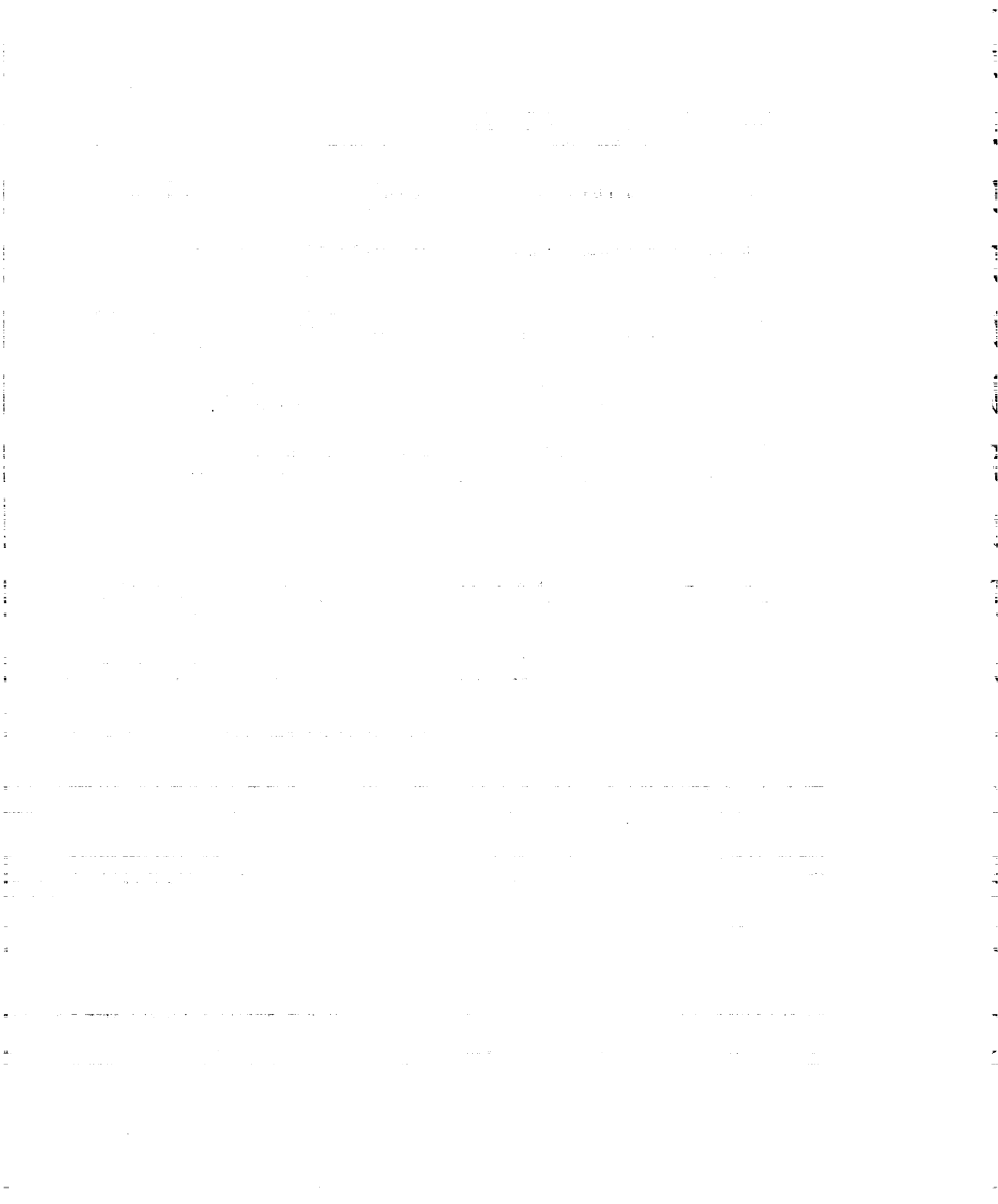
mechanisms involved with wing rock which have yet to be fully understood. However, these experimental results are limited by the difficulties encountered in taking measurements in a dynamic environment.

Computational fluid dynamics (CFD) plays an important role in the design process by providing detailed flowfield information at a relatively low cost that is unavailable with experiment alone. A few computational studies have been initiated to simulate the wing rock problem. However, due to large amounts of computational time, most of these studies have employed various limiting approximations to reduce the computational cost. Inherently, these simplifying flow assumptions restrict the applicability of the solution to steady or inviscid flows. For vortical flows where viscous effects dominate, computation based on the unsteady Navier-Stokes equations is vital. The Navier-Stokes equations can more accurately model flow separations, shock development and motion, and shock-boundary-layer interaction as well as vortex breakdown and vorticity evolution, convection and shedding.

In 1981, the phenomena of slender wing rock was first observed in experiments performed by Nguyen, *et al.*⁽¹⁵⁾. Using an 80° swept delta wing investigation showed that wing rock occurred simultaneously with the appearance of asymmetric leading-edge vortices. By 1984, Ericsson⁽¹⁶⁾ had shown that vortex asymmetry could generate wing rock but growth of the amplitude was limited by vortex breakdown. Arena⁽¹⁷⁾ conducted a thorough experimental investigation of the natural response of a slender wing rock in subsonic flow. He identified the envelope of damped and self sustaining motion for an 80° swept wing and qualitatively compared these results with computational results. Continuing investigation of wing rock, Ng, *et al.*⁽¹⁸⁾ used a water tunnel to compare forced rolling and free-to-roll oscillations of delta wings of various sweep angles with static conditions.

Various experimental attempts to control wing rock have also been investigated experimentally. Malcolm, *et al.*⁽¹⁹⁾ demonstrated a wing's rolling moment can be affected by mechanical or pneumatic manipulation of the strength or location of the leading-edge vortices. In 1993, Walton and Katz⁽²⁰⁾ exploited this idea and applied leading edge control flaps to a free-to-roll double-delta wing. In 1994, Ng, *et al.*⁽²¹⁾ demonstrated passive control of an 80° swept delta wing undergoing wing rock by using flow dividers. At angles of attack higher than 30° , suppression of wing rock was achieved. However, at lower angles of attack, the divider actually promoted the phenomenon. Using asymmetric tangential leading-edge blowing, Wong, *et al.*⁽²²⁾ demonstrated positive post-stall roll control for a delta wing at an angle of attack of 55° . With an active roll feedback control algorithm employing a proportional-derivative compensator, wing rock was stopped in less than one cycle of the limit-cycle motion.

As in experimental investigations of forced rolling oscillations, the focus of computational studies is to be able to predict and ultimately control the phenomenon of wing rock. In 1985, using an unsteady vortex-lattice method, Konstadinopoulos, *et al.*⁽²³⁾ numerically simulated the subsonic experimental work performed by Nguyen, *et al.*⁽¹⁵⁾. They determined that the leading-edge vortex system became unstable as the angle of attack was increased which caused a loss of roll damping at



small angle of roll. Improving the methods for numerical simulation, in 1989, Nayfeh, *et al.*⁽²⁴⁾ proceeded to construct phase planes which revealed the general global nature of wing rock by discussing stable limit cycles, unstable foci, and saddle points. This demonstrated the locations of equilibrium positions. By 1994, Chaderjian and Schiff *et al.*⁽²⁵⁾ had solved for flow over a 65° swept delta wing at 30° angle of attack and Mach of 0.27 that was both forced and free to roll under the influence of the instantaneous aerodynamic rolling moment.

Numerical simulation for the control of wing rock has been performed by various authors primarily, using Euler equations assuming locally conical flow. In 1991, after developing the Navier-Displacement equations for grid deformation, Kandil and Salman⁽²⁶⁾ effectively controlled the wing rock response of an 80° swept delta wing at 30° angle of attack and Mach number of 1.2 by using tuned antisymmetric leading-edge flap oscillations. They also applied the locally conical Euler equations to the same problem at Mach 1.4. The three-dimensional flow solution of Euler equations at Mach 0.3 were also considered.⁽²⁷⁾ Noting the loss of aerodynamic damping rolling moment at the zero angular velocity value, they determined that the hysteretic responses of position and strength of the asymmetric right and left primary vortices were responsible for wing rock and that the phenomenon could be actively controlled through the use of leading edge flaps. In 1991, Kandil and Salman⁽²⁸⁾ solved the thin-layer locally conical Navier-Stokes equations for delta wing at 35° angle of attack. It was again showed that the wing-rock phenomenon could be controlled by using tuned anti-symmetric leading-edge flap oscillations. Details of this work were published in Salman's dissertation.⁽²⁹⁾ In 1993, Lee-Rausch and Batina⁽³⁰⁾ also investigated control of wing rock using locally conical Euler equations using leading-edge flaps. Their study focused on a 75° swept sharp-edged delta wing at a free-stream Mach number of 1.2 at various angles of attack.

In Ref. (31), Menzies and Kandil presented three cases of computationally simulated natural rolling response of a delta wing in transonic and subsonic flow. This was the only known published study in the transonic flow regime using the NS equations. Transonic flow over a 65° swept, cropped delta wing with breakdown of the leading edge vortices demonstrated self sustained rolling oscillations until breakdown dominates the flow field. Two cases of subsonic flow over an 80° swept wing demonstrated either damped or self-sustained rolling oscillations as a function of angle of attack. A complete investigation of the aerodynamic response of the wing, the effects of Mach number, angle of attack, and vortex breakdown were presented.

In this paper, the formulation and method of solution of each multidisciplinary problem is presented. Computational results and validations are also presented and discussed for each problem. The computational applications are focused on the high-angle-of-attack aerodynamics of delta wings and delta wings/vertical tails configurations.

Formulations

Fluid/Structures Interaction

For fluids/structures interaction problems, the formulation consists of three sets of governing equations along with certain

initial and boundary conditions. The first set is the unsteady, compressible, full Navier-Stokes equations. The second set consists of the aeroelastic equations for bending and torsional modes. The third set consists of equations for deforming the grid due to the structure deflections. Next, the governing equations of each set along with the initial and boundary conditions are presented.

Fluid-Flow Equations

The conservative form of the dimensionless, unsteady, compressible, full Navier-Stokes equations in terms of time-dependent, body-conformed coordinates ξ^1 , ξ^2 and ξ^3 is given by

$$\frac{\partial \bar{Q}}{\partial t} + \frac{\partial \bar{E}_m}{\partial \xi^m} - \frac{\partial (\bar{E}_v)_s}{\partial \xi^s} = 0; \quad m = 1 - 3, \quad s = 1 - 3 \quad (1)$$

where

$$\xi^m = \xi^m(x_1, x_2, x_3, t) \quad (2)$$

$$\bar{Q} = \frac{1}{J} [\rho, \rho u_1, \rho u_2, \rho u_3, \rho e]^T, \quad (3)$$

\bar{E}_m and $(\bar{E}_v)_s$ are the ξ^m -inviscid flux and ξ^s -viscous and heat conduction flux, respectively. Details of these fluxes are given in Ref. 10.

Aeroelastic Equations

The dimensionless, linearized governing equations for coupled bending and torsional vibrations of a vertical tail, that is treated as a cantilevered beam, are considered. The tail bending and torsional deflections occur about an elastic axis that is displaced from the inertial axis. These equations for the bending deflection, w , and the twist angle, θ , are given by

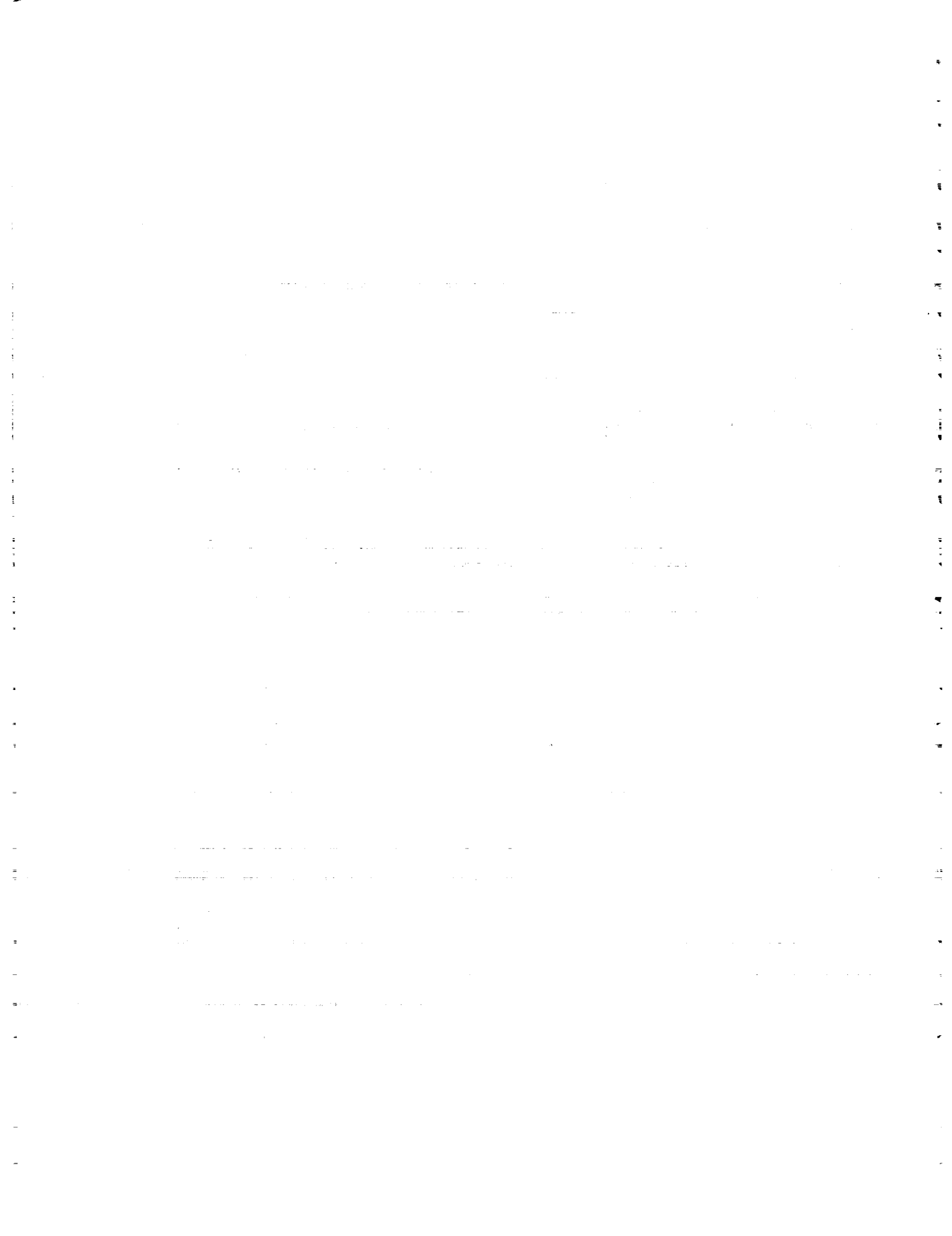
$$\begin{aligned} \frac{\partial^2}{\partial z^2} \left[EI(z) \frac{\partial^2 w}{\partial z^2}(z, t) \right] + m(z) \frac{\partial^2 w}{\partial t^2}(z, t) \\ + m(z) x_\theta(z) \frac{\partial^2 \theta}{\partial t^2}(z, t) = N(z, t) \end{aligned} \quad (4)$$

$$\begin{aligned} \frac{\partial}{\partial z} \left[GJ(z) \frac{\partial \theta}{\partial z}(z, t) \right] - m(z) x_\theta \frac{\partial^2 w}{\partial t^2}(z, t) \\ - I_\theta(z) \frac{\partial^2 \theta}{\partial t^2}(z, t) = -M_t(z, t) \end{aligned} \quad (5)$$

where z is the vertical distance from the fixed support along the tail length, l , EI and GJ the bending and torsional stiffness of the tail section, m the mass per unit length, I_θ the mass-moment of inertia per unit length about the elastic axis, x_θ the distance between the elastic axis and inertia axis, N the normal force per unit length and M_t the twisting moment per unit length. The characteristic parameters for the dimensionless equations are c^* , a_∞^* , ρ_∞^* and c^*/a_∞^* for the length, speed, density and time; where c^* is the delta wing root-chord length, a_∞^* the freestream speed of sound and ρ_∞^* the freestream air density. The geometrical and natural boundary conditions on w and θ are given by

$$\begin{aligned} w(0, t) = \frac{\partial w}{\partial z}(0, t) = \frac{\partial^2 w}{\partial z^2}(l, t) \\ = \frac{\partial}{\partial z} \left[EI(l) \frac{\partial^2 w}{\partial z^2}(l, t) \right] = 0 \end{aligned} \quad (6)$$

$$\theta(0, t) = \frac{\partial \theta}{\partial z}(l, t) = 0 \quad (7)$$



The solution of Eqs. (4) and (5) are given by

$$w(z, t) = \sum_{i=1}^I \phi_i(z) q_i(t) \quad (8)$$

$$\theta(z, t) = \sum_{j=I+1}^M \phi_j(z) q_j(t) \quad (9)$$

where ϕ_i and ϕ_j are comparison functions satisfying the free-vibration modes of bending and torsion, respectively, and q_i and q_j are generalized coordinates for bending and torsion, respectively. In this paper, the number of bending modes, \bar{I} , is six and the number of torsion modes, $M - \bar{I}$, is also six. Substituting Eqs. (8) and (9) into Eqs. (4) and (5) and using the Galerkin method along with integration by parts and the boundary conditions, Eqs (6) and (7), we get the following equation for the generalized coordinates q_i and q_j in matrix form:

$$\begin{bmatrix} M_{11} & M_{12} \\ M_{21} & M_{22} \end{bmatrix} \begin{pmatrix} \ddot{q}_i \\ \ddot{q}_j \end{pmatrix} + \begin{bmatrix} K_{11} & 0 \\ 0 & K_{22} \end{bmatrix} \begin{pmatrix} q_i \\ q_j \end{pmatrix} = \begin{pmatrix} \dot{N}_1 \\ \dot{N}_2 \end{pmatrix} \quad \begin{matrix} i = 1, 2, \dots, \bar{I} \\ j = \bar{I} + 1, \dots, M \end{matrix} \quad (10)$$

where

$$\left. \begin{aligned} M_{11} &= \int_0^l m \phi_i \phi_i dz \\ M_{12} &= M_{21} = \int_0^l m x \phi_i \phi_j dz \\ M_{22} &= \int_0^l I \phi_j \phi_j dz \end{aligned} \right\} \quad (11)$$

$$\left. \begin{aligned} K_{11} &= \int_0^l EI \frac{d^2 \phi_i}{dz^2} \frac{d^2 \phi_i}{dz^2} dz \\ K_{22} &= \int_0^l GJ \frac{d \phi_j}{dz} \frac{d \phi_j}{dz} dz \end{aligned} \right\} \quad (12)$$

$$\left. \begin{aligned} \dot{N}_1 &= \int_0^l \dot{\phi}_i N dz \\ \dot{N}_2 &= \int_0^l \dot{\phi}_j N dz \end{aligned} \right\} \quad (13)$$

The numerical integration of Eqs. (11)-(13) is obtained using the trapezoidal method with 125 points to improve the accuracy of integrations. The solution of Eq. (10), for q_i ; $i = 1, 2, \dots, \bar{I}$, and q_j ; $j = \bar{I} + 1, \dots, M$, is obtained using the Runge-Kutta scheme. Next, w , and θ are obtained from Eqs. (8) and (9).

Grid Displacement Equations

Once w and θ are obtained at the $n + 1$ time step, the new grid coordinates are obtained using simple interpolation equations. In these equations, the twin tail bending displacements, $w_{i,j,k}^{n+1}$, and their displacements through the torsion angle, $\theta_{i,j,k}^{n+1}$, are interpolated through cosine functions, with maximum displacements at the tail surface and zero displacements at the computational boundaries.

Boundary and Initial Conditions

Boundary conditions consist of conditions for the fluid flow and conditions for the aeroelastic bending and torsional deflections of the tails. For the fluid flow, the Riemann-invariant boundary conditions are enforced at the inflow and outflow boundaries of the computational domain. At the plane of geometric symmetry, periodic boundary conditions is specified with the exception of grid points on the tail. On the wing surface, the no-slip and no-penetration conditions are enforced and $\frac{\partial p}{\partial n} = 0$. On the tail surfaces, the no-slip and no-penetration conditions for the relative velocity components are enforced

(points on the tail surface are moving). The normal pressure gradient is no longer equal to zero due to the acceleration of the grid points on the tail surface. This equation becomes $\frac{\partial p}{\partial n} = -\rho \bar{a}_t \cdot \bar{n}$, where \bar{a}_t is the acceleration of a point on the tail and \bar{n} is the unit normal.

Initial conditions consist of conditions for the fluid flow and conditions for the aeroelastic deflections of the tails. For the fluid flow, the initial conditions correspond to the freestream conditions with no-slip and no-penetration conditions on the wing and tail. For the aeroelastic deflections of the tail, the initial conditions for any point on its surface are that the displacement and velocity are zero, $w(z, 0) = 0$, $\frac{\partial w}{\partial t}(z, 0) = 0$, $\theta(z, 0) = 0$ and $\frac{\partial \theta}{\partial t}(z, 0) = 0$.

Fluids/Dynamics Interaction

For fluids/dynamics interaction problems, the formulation consists of two sets of governing equations, and initial and boundary conditions. The first set is the unsteady, compressible, full Navier-Stokes equations. This set has already been given in Eqs. (1)-(3). The second set is the Euler equations of rigid body dynamics. In this paper, we consider only one-degree of freedom for the wing motion. For the natural rolling response, the resultant external aerodynamic rolling moment is equated to the time rate of change of the angular rolling moment about the axis of rolling motion. This equation is given by

$$C_{m, roll} = I_{xx} \dot{\omega}_x \quad (14)$$

where I_{xx} is the principal mass moment of inertia for the wing, and $\dot{\omega}_x$ is the roll acceleration.

Boundary and Initial Conditions and Grid Motion

Since the wing is undergoing rolling motion, the grid is moved with the same angular motion as that of the body. The grid speed, $\frac{\partial \bar{x}}{\partial t}$, and the metric coefficient, $\frac{\partial \bar{x}}{\partial x}$, are computed at each time step of the computational scheme. Consequently, the kinematic boundary conditions at the inflow-outflow boundaries and at the wing surface are expressed in terms of the relative velocities. Again, the dynamic boundary condition, $\frac{\partial p}{\partial n}$, on the wing surface is no longer equal to zero. This condition is modified for the oscillating wing as:

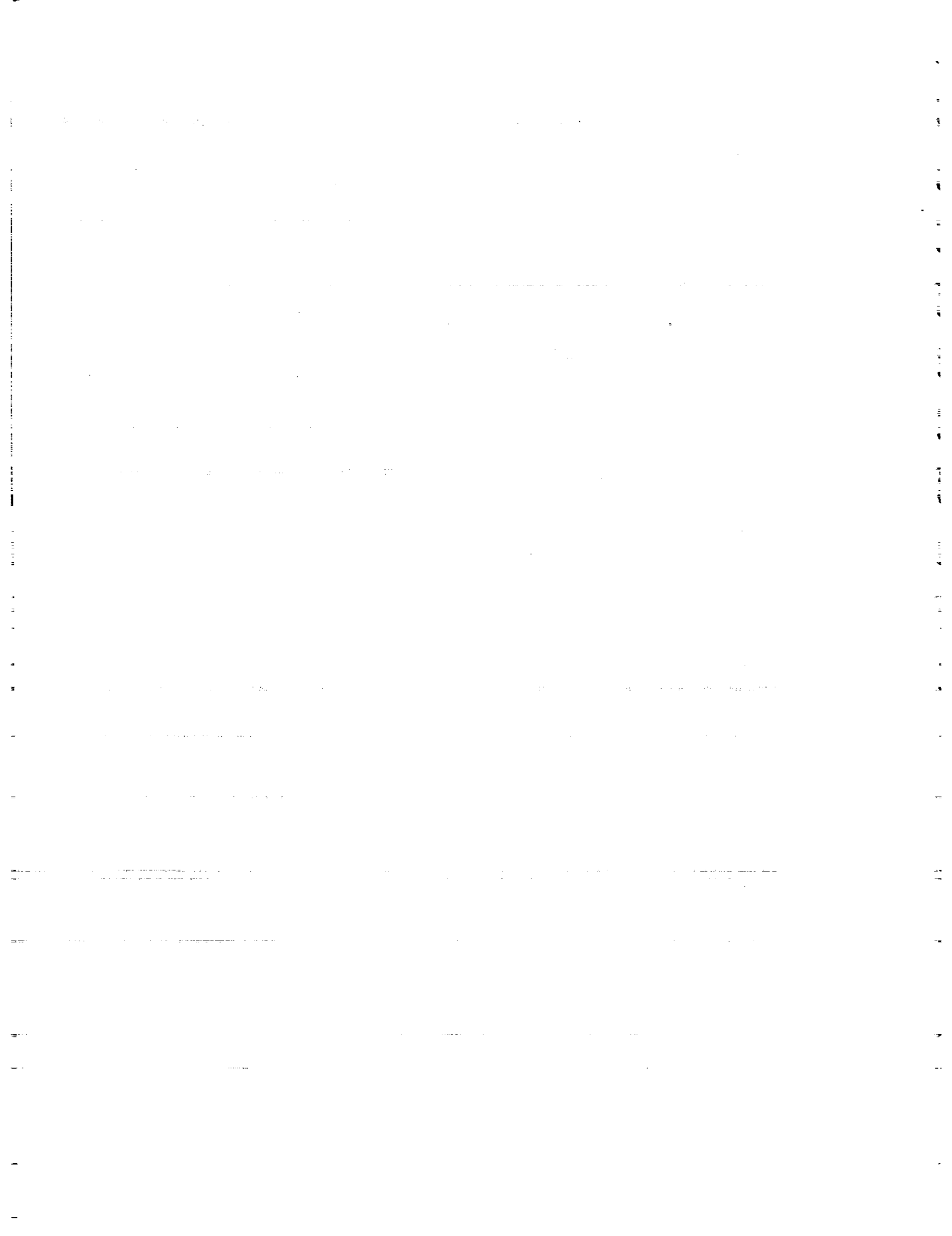
$$\frac{\partial p}{\partial n} \Big|_{wing} = -\rho \bar{a} \cdot \bar{n} \quad (15)$$

where \bar{a} is the acceleration of a point on the wing flat surface; \bar{n} , the unit normal to the wing surface. The acceleration is given by:

$$\bar{a} = \dot{\omega} \times \bar{r} + \omega \times (\omega \times \bar{r}) \quad (16)$$

where ω is the angular velocity. Notice that for a rigid body, the position vector \bar{r} , is not a function of time and hence, $\dot{\bar{r}} = \ddot{\bar{r}} = 0$. Finally, the boundary condition for the temperature is obtained from the adiabatic boundary condition and is given by:

$$\frac{\partial T}{\partial n} \Big|_{wing} = 0 \quad (17)$$



Method of Solution

Fluids/Structures Interaction

The first step is to solve for the fluid flow problem using vortex-breakdown conditions and keeping the tails rigid. The NS equations are solved with the grid speed set equal to zero. The implicit, upwind, flux-difference splitting, finite-volume scheme is used to solve the unsteady, compressible, full Navier-Stokes equations. This scheme uses the flux-difference splitting of Roe, and a smooth flux limiter is used to eliminate oscillation at locations of large flow gradients. The viscous and heat flux terms are linearized in time and the cross derivative terms are eliminated in the implicit operator and retained in the explicit terms. The viscous terms are differenced using second-order accurate central differencing. The resulting difference equation is approximately factored to solve the equations in three sweeps in the ξ^1 , ξ^2 , and ξ^3 , directions. The computational scheme is coded in the computer program "FTNS3D". This step provides the flow field solution along with the pressure difference across each of the tails. The pressure difference is used to generate the normal force and twisting moment per unit length of each tail. Next, the aeroelastic equations, Eqs. (4)-(13), are used to obtain the tails deflections, $w_{i,j,k}$ and $\theta_{i,j,k}$. The grid displacement equations are then used to compute the new grid coordinates. Once the tails are allowed to deform, the metric coefficients of the coordinate Jacobian matrix are updated as well as the grid speed, $\frac{\partial \xi}{\partial t}$. This computational cycle is repeated every time step.

Fluids/Dynamics Interaction

The method of solution consists of three steps. In the first step, the problem is solved for the stationary wing at 0° roll angle. This solution represents the initial conditions for the second step. In the second step, the dynamic initial conditions are specified. In this paper, we consider two types of flow regime; a transonic case and subsonic cases. For the transonic case, the wing is subjected to an initial velocity. For the subsonic cases, a quarter cycle of a sinusoidal function is specified to roll the wing to a 10° roll angle with zero angular velocity while the Navier-Stokes equations are solved accurately in time. Having specified the dynamic initial conditions, the third step proceeds. Applying a four-stage Runge-Kutta scheme and the specified dynamic initial conditions for θ and $\dot{\theta}$, Eq. (14) is explicitly integrated in time in sequence with the fluid dynamic equations.

Equation (14) is used to solve for θ , $\dot{\theta}$, and $\ddot{\theta}$ while the fluid dynamics equations provide the pressure distribution over the wing surface. The pressure distribution is integrated over the surface of the wing to determine $C_{m_{\text{roll}}}$, with respect to the axis of geometric symmetry. At each time step, the wing and the grid are rotated corresponding to θ and $\dot{\theta}$ resulting in the natural rolling response of the delta wing to the fluid flow. Due to the dynamic nature of the problem, the metric coefficients and the grid speed are computed at each time step. The computations proceed until periodic response is reached.

Computational Application And Discussion

Fluid-Structure Interaction; Twin-Tail Buffet

The twin tail-delta wing configuration used in this application consists of a 76° -swept back, sharp-edged delta wing (aspect ratio of one) and dynamically scaled flexible twin tails similar to those used by Washburn, et. al. (Ref 6). The vertical tails are oriented normal to the upper surface of the delta wing and have a centerline sweep of 53.5° . Each tail is made of a single Aluminum spar and Balsa wood covering. The Aluminum spar has a taper ratio of 0.3 and a constant thickness of 0.001736. The chord length at the root is 0.03889 and at the tip is 0.011667, with a span length of 0.22223. The Aluminum spar is constructed from 6061-T6 alloy with density, ρ , moduli of elasticity and rigidity, E and G of 2693 kg/m^3 , $6.896 \times 10^{10} \text{ N/m}^2$ and $2.5925 \times 10^{10} \text{ N/m}^2$, respectively. The Balsa wood covering has a taper ratio of 0.23 and aspect ratio of 1.4. The chord length at the root is 0.2527 and at the tip is 0.058, with a span length of 0.2223. The Balsa thickness decreases gradually from 0.0211 at the tail root to 0.0111 at the tail midspan and then constant thickness of 0.0111 is maintained to the tail tip. The tail cross section is a semi-diamond shape with bevel angle of 20° . The Balsa density, moduli of elasticity and rigidity, E and G , are 179.7 kg/m^3 , $6.896 \times 10^8 \text{ N/m}^2$ and $2.5925 \times 10^8 \text{ N/m}^2$, respectively. The tails are assumed to be magnetically suspended and the leading edge of the tail root is positioned at $x/c = 1.0$, measured from the wing apex. The configuration is pitched at an angle of attack of 30° and the freestream Mach number and Reynolds number are 0.3 and 1.25×10^6 , respectively.

A multi-block grid consisting of 4 blocks is used for the solution of the problem. The first block is a O-H grid for the wing and upstream region, with $101 \times 50 \times 54$ grid points in the wrap around, normal and axial directions, respectively. The second block is a H-H grid for the inboard region of the twin tails, with $23 \times 50 \times 13$ grid points in the wrap around, normal and axial directions, respectively. The third block is a H-H grid for the outboard region of the twin tails, with $79 \times 50 \times 13$ grid points in the wrap around, normal and axial directions, respectively. The fourth block is a O-H grid for the downstream region of the twin tails, with $101 \times 50 \times 25$ grid points in the wrap around, normal and axial directions, respectively. Figure 1 shows the grid topology and a blow-up of the twin tail-delta wing configuration.

The configuration is investigated for three spanwise positions of the twin tails; the inboard location, the midspan location and the outboard location corresponding to a separation distance between the twin tails of 33%, 56% and 78% of the wing span; respectively.

Inboard Location of Twin Tails (33% wing span)

The spanwise distance between the two tails is 33% of the wing span. Figure 2 shows three-dimensional and front views for the initial conditions with the surface total pressure contours and the streamlines of the vortex cores. Figure 3 shows the static pressure contours and the instantaneous streamlines in a cross flow plane at $x = 1.096$. The initial conditions are obtained after 10,000 time steps, $\Delta t = 0.001$, with the twin tails kept rigid. It is observed that the vortex cores experience an almost symmetric breakdown on the wing at about the 75% chordstation. Downstream of the wing, they are totally outside of the space between the twin tails. Smaller size vortex cores appear under the vortex breakdown flows and at the lower edges of the twin tails. These results exactly match

1. The first part of the document is a letter from the President of the United States to the Congress.

2. The second part is a report from the Secretary of the Treasury.

3.

4. The third part is a report from the Secretary of the Navy.

5. The fourth part is a report from the Secretary of the War.

6. The fifth part is a report from the Secretary of the Interior.

7. The sixth part is a report from the Secretary of the Agriculture.

8. The seventh part is a report from the Secretary of the Commerce.

9. The eighth part is a report from the Secretary of the Education.

10.

11. The ninth part is a report from the Secretary of the Health.

12.

13. The tenth part is a report from the Secretary of the Labor.

14. The eleventh part is a report from the Secretary of the Public Works.

15. The twelfth part is a report from the Secretary of the Public Health.

16. The thirteenth part is a report from the Secretary of the Public Education.

17.

18. The fourteenth part is a report from the Secretary of the Public Works.

19.

20. The fifteenth part is a report from the Secretary of the Public Health.

21. The sixteenth part is a report from the Secretary of the Public Education.

22. The seventeenth part is a report from the Secretary of the Public Works.

23.

24. The eighteenth part is a report from the Secretary of the Public Health.

25.

26. The nineteenth part is a report from the Secretary of the Public Education.

27.

28. The twentieth part is a report from the Secretary of the Public Works.

29.

30.

31.

32.

33.

34.

Washburn observations. Figures 4 and 5 show the results for the twin tails undergoing uncoupled bending-torsion responses after 9,600 time steps from the initial conditions. It is observed that the breakdown shapes and locations are affected by the twin tail oscillations. The vortex breakdown is now strongly asymmetric, and the vortex breakdown flows are still outside of the space between the twin tails. These results conclusively show the upstream as well as the spanwise effect of the twin tail oscillations on the vortex breakdown flow.

Figures 6–8 show the distribution of deflection and load responses along the left and right tails every 2 time units, the history of deflection and load responses versus time and the total structural deflections and root bending moment for the left and right tails. It is observed that the bending and torsion responses are in their first and second mode shapes. The frequencies of the bending deflections are less than one-half those of the torsion deflections. The normal forces are out of phase of the bending deflections while the torsion moments are in phase with the torsion deflections. The total tail responses are in first, second and third mode shapes. Periodic responses have not been reached within the computational time covered (20,000 time steps = 10 dimensionless time units).

Midspan Location of Twin Tails (56% wing span)

The results of this case are presented in Figs. 9–15. Figures 9–12 show that the tails cut through the vortex breakdown of the leading-edge vortex cores, which are also asymmetric. Figure 13 shows that the bending deflections are lower than those of the inboard case while the torsional deflections are substantially lower than those of the inboard case. Moreover, Fig. 13 shows that the bending and torsion deflections have a single sign for the left and right tails (all are positive or all are negative). Figure 14 shows that both bending and torsion deflections are out of phase of the normal force and twisting moment loads. The total deflections of Fig. 15 show the same trend. The root bending moments of Fig. 15 are also lower than those of the inboard case.

Outboard Location of Twin Tails (78% wing span)

Figures 16–20 show the results of this case. Figures 16 and 17 show that the space between the twin tails include larger portion of the vortex breakdown flow of the leading-edge vortex cores, than that of the midspan case. The vortex breakdown flow is also asymmetric. The vortical flow on the lower outside surfaces of the twin tails is larger than any of the above two cases. Figures 18–20 show that the bending and torsion deflections are lower than those of the midspan case. They also show that both bending and torsion deflections are out of phase of the bending and torsional loads. The frequencies of the bending deflections are still smaller than those of the torsion deflections. All these observations are in very good agreement with those of Washburn, et. al. (Ref 6). Figures 21–23 show the histories of the lift and drag coefficients versus time for the inboard, midspan and outboard locations, respectively. It is observed that the loss in CL is the largest for the inboard location case.

Table 1. shows a comparison of the present results of the mean root bending moment for flexible twin tails and the lift

coefficient with rigid twin tails with those of Washburn, et. al. (Ref 6), experimental data.

Parameter	Position	FTNS3D (present)	WASHBURN (6)
Mean Root Bending Moment With Flexible Tails	Inboard	5.62×10^{-5}	7.43×10^{-5}
	Midspan	4.22×10^{-5}	6.05×10^{-5}
	Outboard	3.62×10^{-5}	5.70×10^{-5}
Lift Coefficient With Rigid Tails	Inboard	1.0423	1.17
	Midspan	1.0515	1.12
	Outboard	1.0674	1.17

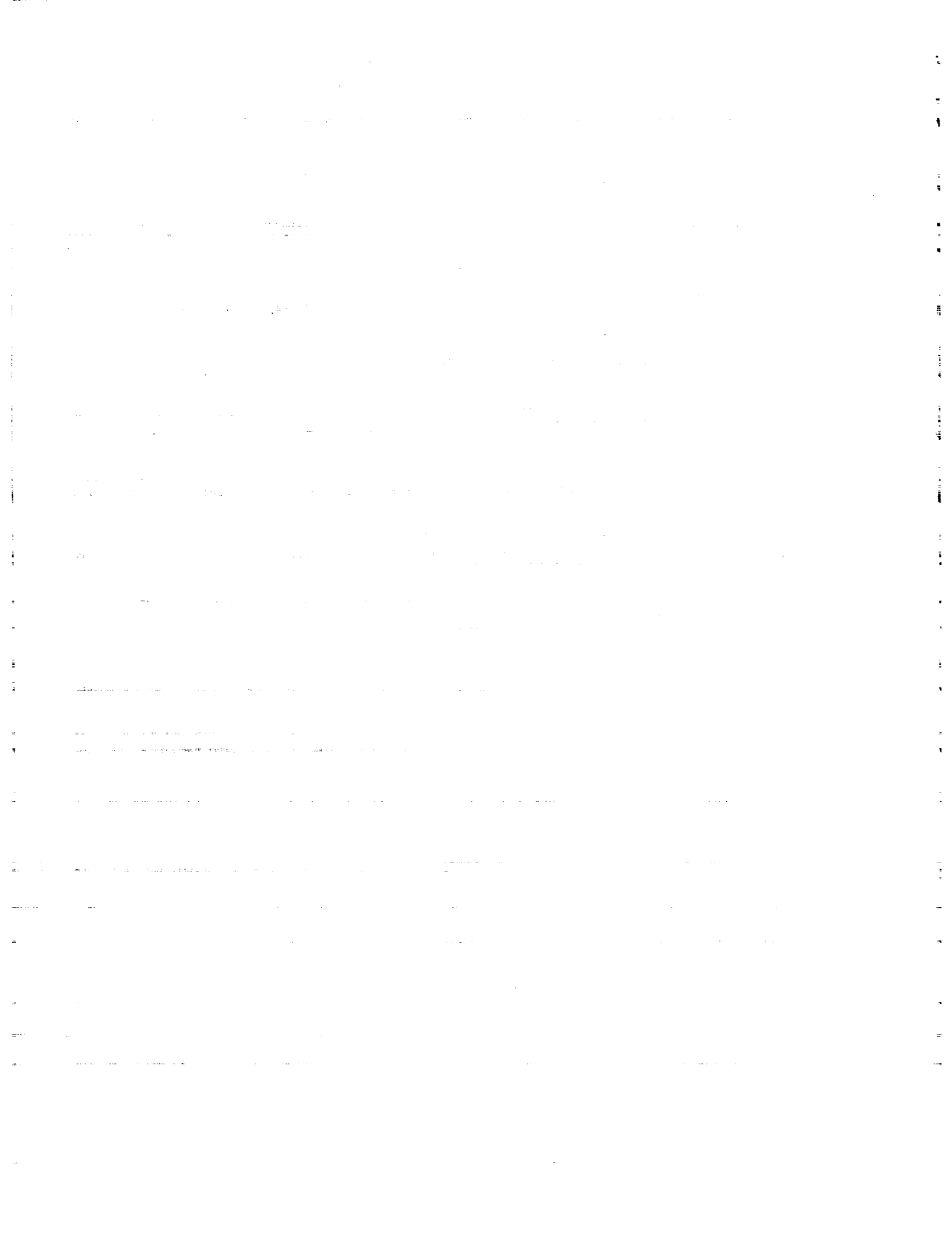
Fluids/Dynamics Interaction

Case I-Transonic Flow over a Cropped Delta Wing

A 65° swept-back, sharp edged, cropped delta wing of zero thickness is considered for the transonic flow solutions. The cropping ratio (tip length/root-chord length) is 0.15. An O-H grid of 65 x 43 x 105 in the wrap-around, normal, and axial directions, respectively, is used. The computational domain extends two chord lengths forward and five chord lengths downstream of the wing trailing edge. The radius of the computational domain is four chord lengths. The minimum grid size in the normal direction to the wing surface is 5×10^{-4} from the leading edge to the plane of symmetry. The initial conditions correspond to the solution of the wing held at 20° angle of attack and 0° roll angle after 18,000 time steps at a Mach number and Reynolds number of 0.85 and 3.23×10^6 , respectively.

Plots of the initial condition depict a solution characterized by weak oblique shocks beneath the primary vortices and a strong, transverse terminating shock located at approximately $x = 0.86$ (See Fig. 24). These shocks bound a substantial supersonic pocket. Outboard of the oblique shocks, a subsonic, separated region depicts a secondary vortex which exists until $x = 0.91$. The primary vortex interacts with the terminating shock and enlarges indicating vortex breakdown. The plots of the Mach number contours, instantaneous streamlines, and surface of constant entropy shown in Fig. 24 depict clearly a bubble type vortex breakdown and the flow appears to be completely symmetric.

From the initial conditions, the wing is given an instantaneous roll velocity of $\dot{\theta} = +0.925 \times 10^{-4}$. For convention, a positive roll velocity indicate that the right hand side of the wing when looking in the upstream direction is moving upward. With a dimensionless mass moment of inertia of $I_{xx} = 2.88 \times 10^{-3}$, the wing is free to respond to the rolling moment induced by the fluid flow. Figure 25 shows the time history of the resultant motion and lift coefficient curve. While the motion appears somewhat periodic after $t = 30$, there is a chaotic behavior in the cyclic response due to the vortex breakdown which leads to divergence of the motion after five cycles of rolling. The highly unsteady nature of the shock induced vortex breakdown promotes very irregular motion and aerodynamic response histories. The lift coefficient indicates an initial loss after the onset of motion and fluctuates between 0.36 and 0.40 during the quasi-periodic response. After $t =$



120 when the wing motion diverges to approximately 24° , the lift drops considerably.

Figure 26 shows snapshots of the Mach contours near the wing surface and surfaces of constant entropy depicting the primary vortex core and breakdown. During the quasi-periodic response, the terminating shock and vortex breakdown location oscillate laterally as shown in views a) to d). In contrast to subsonic flow where the breakdown and restructuring of the vortex serves to dampen the motion;⁽¹⁷⁾ in transonic flow, the sustained oscillation of the wing appears to be caused by the asymmetric motion of the breakdown location. However, as time progresses, the frequency of oscillation is slightly increased. In Ref. 32, it was shown that when forced to roll at a reduced frequency of 2π , the transverse shock was weakened as a result of the motion and the breakdown washes downstream. In this case, after $t = 120$, (shown in view e), the shock on the upward moving side appears to weaken as a result of the increased rolling frequency and the breakdown washes downstream. On the downward moving side, the breakdown location advances to apex of the wing which results in a significant drop in the lift. Without breakdown on the right side, the wing rolls until equilibrium is reached at a positive mean roll angle of 24.2° . Small amplitude fluctuations of this roll angle are observed due to the unsteady nature of the complete breakdown on the left side of the wing.

Case II-Subsonic Flow over a Delta Wing undergoing Damped Rolling Oscillations

In order to compare with available experimental data, an 80° swept-back, sharp-edged delta wing of zero thickness is considered for the subsonic flow solutions. This wing was modeled after the experimental model used by Arena.⁽¹⁷⁾ An O-H grid of $65 \times 43 \times 84$ in the wrap-around, normal, and axial directions, respectively, is used. The computational domain extends two chord lengths forward and five chord lengths backward from the wing trailing edge. The radius of the computational domain is four chord lengths. The minimum grid size in the normal direction to the wing surface is 5×10^{-4} from the leading edge to the plane of symmetry. The initial conditions correspond to the solution of the wing held at 10° angle of attack and 0° roll angle after 17,500 time steps at a Mach number and Reynolds number of 0.1 and 0.4×10^6 respectively. The flowfield has no observable vortex breakdown.

From the initial conditions, the wing is forced to roll to an initial roll angle of $\theta = 10.0^\circ$. Again, by convention, a positive roll angle indicates that the right hand side of the wing when looking in the upstream direction is rolled upward. The wing is then released to respond to the fluid flow with a mass moment of inertia about the x - axis of $I_{xx} = 2.253 \times 10^{-2}$. Figure 27 shows the time history of the resultant motion and lift coefficient curve. This plot characterizes the damped rolling oscillations observed of wing at relatively low angles of attack in a subsonic freestream. At an angle of attack of 10° and $M_\infty = 0.1$, an 80° swept delta wing will not undergo self sustained wing rock. From the initial displacement of 10° roll angle, the wing rolls to a minimum of -3.11° in overshoot and returns to a positive roll angle before reaching the steady state response at $\theta = 0^\circ$. Meanwhile, the lift coefficient increases by 8.4%.

Figure 28 shows a comparison of the Mach number contours and instantaneous streamlines of the initial conditions when the wing is released at $\theta = 10^\circ$ and the steady state response when the wing is at rest at $\theta = 0^\circ$. Notice that there is very little motion of the vortex cores. As a result, the variation of the pressure distribution is extremely small. Without large pressure differences between the left and right sides of the wing, the angular velocity remains small and the motion of the wing subsides. There is no noticeable lagging of the motion of the fluid with respect to the motion of the wing.

Case III-Subsonic Flow over a Delta Wing undergoing Self-sustained Rolling Oscillations

The same 80° swept-back, sharp-edged delta wing of zero thickness is considered for this case. To duplicate the experimental investigation by Arena,⁽¹⁷⁾ the initial conditions correspond to the solution of the wing held at 30° angle of attack and 0° roll angle after 17,500 time steps at a Mach number and Reynolds number of 0.1 and 0.4×10^6 respectively.

From the initial conditions, this wing is also forced to roll to an initial roll angle of $\theta = 10.0^\circ$ as in the previous case. The wing is then released to respond to the fluid flow with a mass moment of inertia about the x - axis of $I_{xx} = 2.253 \times 10^{-2}$. Figure 29 shows the phase and time history of the resultant motion. From the initial displacement of $\theta = 10^\circ$, the wing oscillated in roll with a growing amplitude until periodicity is reached three cycles later. By $t = 60$, the motion is completely periodic with a maximum limit-cycle amplitude of 41.2° . For comparison, the experimental results for the same wing performed by Arena⁽¹⁷⁾ showed a steady state amplitude of 41° at the same Reynolds number. Viewing the time histories of all three rotational properties, it is clear that the angular acceleration and roll angle are exactly 180° out of phase, while the angular velocity is nearly 90° out of phase.

Figure 30 shows the time history of the lift coefficient and the phase of the periodic response of the rolling moment coefficient. Notice that the lift coefficient curve oscillates at twice the frequency of the wing motion. In the phase plot of the rolling moment coefficient, it is interesting to note the three lobes of the periodic response. These lobes represent the energy shift from the wing to the fluid in the outer two lobes as indicated by the "+" and from the fluid to the wing in the middle lobe as indicated by the "-". These outer lobes are referred to as damping lobes. In the plot of the time history of the angular acceleration (Fig. 29), irregularities due to the damping lobes are noted near the peaks of the curve. Since these lobes are not present in the damped oscillation case, careful study of the flowfield at these points may provide insight into the wing rock phenomenon.

Figure 31 shows snapshots of a complete cycle of rolling depicting the total pressure contours at key points labeled in Figs. 29 and 30. As the wing is approaching the maximum angular velocity, points g) to h) and j) to k), the footprint of the vortex core on the upward moving side appears to bow outward toward the leading edge of the wing. It appears that the uneven movement of the vortex core with respect to the leading edge is a result of the lagging movement of the fluid in response to the motion of the wing. Near the trailing edge, this effect is more pronounced due to the increased absolute velocity of the wing near the outer edges of the surface. When the fluid

motion catches up to the motion of the wing, the energy flows from the fluid to the wing promoting the rolling motion, and stimulating wing rock. As the wing rolls, the angular velocity increases until the wing exceeds $\theta = \pm 27^\circ$. Near the trailing edge, the absolute velocity of the wing exceeds the limit of the motion that the fluid can maintain. The flowfield reflects this lag by the bowed appearance of the vortex core. When the fluid flow motion lags the wing motion, energy is absorbed by the fluid providing damping to the system as indicated by the "+" in rolling moment phase diagram of Fig. 30. As the wing slows, the cores appear to straighten and snap back. This effectively rolls the wing in the opposite direction.

In Figure 32, a plot of the core positions at $x = 0.77$ is shown to demonstrate the symmetric motion of the vortex cores. Note that the cubic splines connecting the individual points do not represent the path taken but are merely shown for connectivity. During the energy transfer from the wing to the fluid, from points f) to g) and i) to j), the position of the vortex cores exhibits a more vertical motion. When the energy is transferred from the fluid to the wing, the position of the vortex cores shift in a lateral direction paralleling the surface of the wing. This motion is coincident with the lagging motion of the fluid with respect to the wing.

Concluding Remarks

Recent advances in aeronautical multidisciplinary problems have been presented. Two problems are considered in this paper. The first is that of fluids/structures interaction with applications to the twin vertical tail buffet of a generic aircraft. The second is that of fluids/dynamics interaction with applications to the natural rolling response of delta wings.

For the buffet responses of the twin-tail configuration of the generic model, three sets of equations have been used for the aerodynamic loads, the bending and torsional deflections and the grid displacements due to the twin tail deflections. The leading-edge vortex breakdown flow has been generated using a 76° -swept back sharp-edged delta wing which is pitched at 30° angle of attack. The twin tails are cantilevered without a trailing edge extension. Only, uncoupled bending-torsion response cases are considered in this study.

The present computational results of the generic model are in very good agreement with the experimental data of Washburn, et. al. generic model. It is concluded that the inboard location of the twin tails produces the largest bending-torsion loads, deflections, frequencies and root bending moments when compared with the midspan and outboard locations. The outboard location produces the least of these responses. When the twin tails cut through the vortex breakdown flow, they produce less responses due to the compensating damping effect produced by the left and right parts of the vortex breakdown flow on each tail.

For the natural rolling response of delta wing, transonic and subsonic flow-regime cases are considered. The first case demonstrates the effects of vortex breakdown in the transonic regime. With the shock induced vortex breakdown, the derivatives of the motion and the aerodynamic properties show a very high frequency, low amplitude disturbance resulting from the shock-vortex interaction. Oscillations in the location of the shock and vortex breakdown location induces the wing to

roll, however, the wing is unable to remain in a stable limit cycle. Divergence of the motion is observed when the rolling frequency is sufficient to cause the transverse shock to weaken on the upward moving side. The wing responds by continuing to roll until an equilibrium point is reached.

The second and third cases are presented to provide a comparison with available experimental data. Case II demonstrates at a relatively low angle of attack, that an 80° swept delta wing will not undergo self-sustained oscillations. Within one cycle, the wing resumes the steady state position of 0° roll angle. The motion of the wing and vortex cores is very slight. With the relatively small angular velocity of the wing, the fluid motion does not lag the motion of the wing. The flowfield then dampens the wing response and prevents self-sustained oscillations.

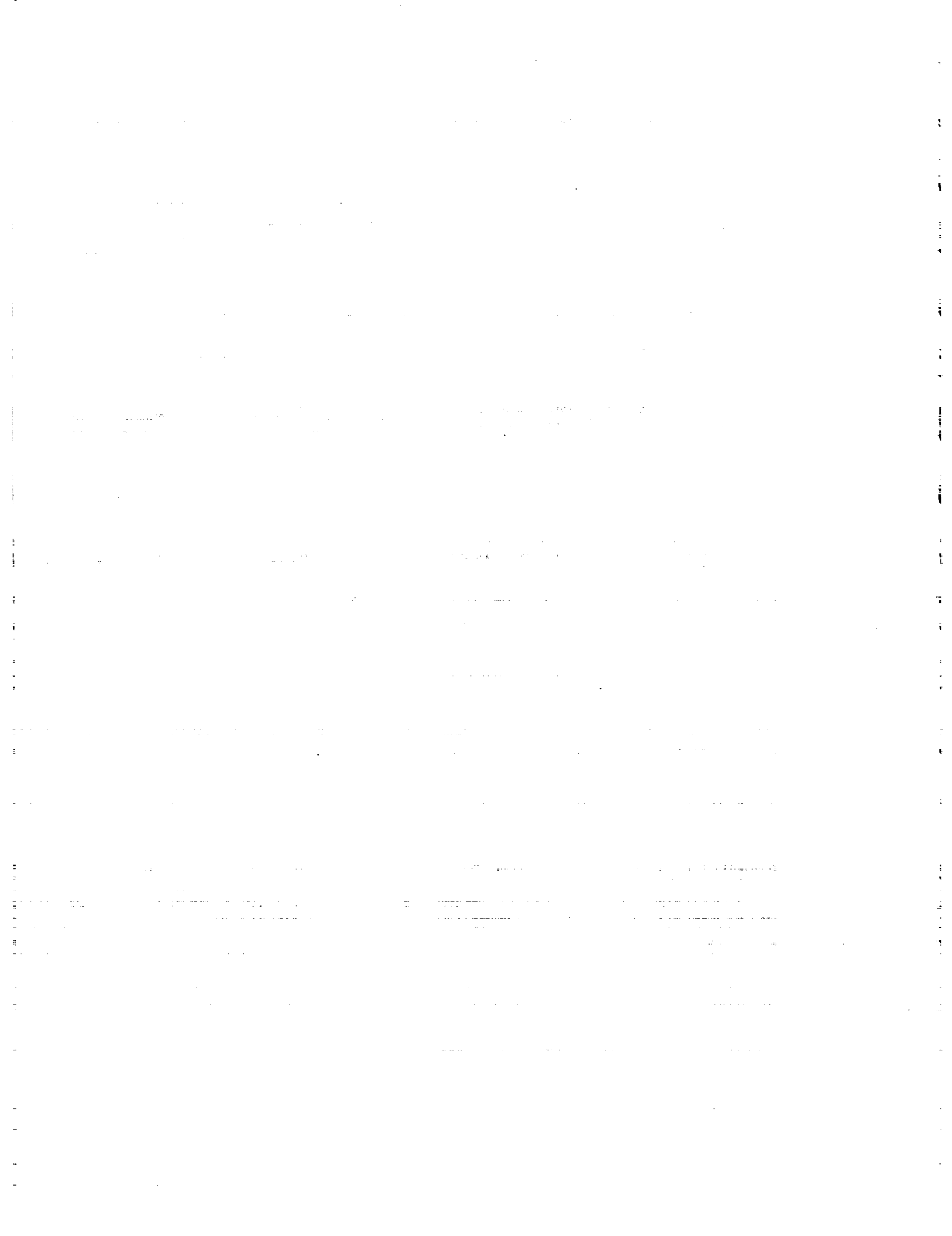
In contrast, the third case of the delta wing at an angle of attack of 30° does exhibit the self-sustained limit-cycle rolling oscillation known as wing rock. Within three cycles of oscillation, the wing motion sustains a roll amplitude of 41.2° and a period of oscillation of 23.1 nondimensional time. The phase diagram of the rolling-moment coefficient shows three distinct lobes which represent the energy shift from the fluid to the wing and vice versa. When the wing is first released to respond to the fluid, the pressure distribution shows a much stronger asymmetry than in the previous case due to the higher angle of attack, this results in a faster roll velocity. Instead of the motion damping as in the first case, the increased velocity causes the motion to overshoot. It appears that the velocity of the wing near the trailing edge exceeds the ability of the fluid to respond. Since the motion of the vortex core is inhibited near the trailing edge, the core exhibits a distinctive bowed shape. While the motion of the fluid lags the wing response, energy is stored in the vortex cores. The wing motion slows as a result of the damping provided by the energy transfer to the fluid and reverses roll direction. With the slowing of the roll rate, the motion of the fluid ceases to lag the motion of the wing. The vortex cores appear to snap back. On doing so, the energy stored in the fluid is imparted to the wing causing the roll velocity to increase. This cyclic motion builds until the energy transfer of the system is balanced and the periodic response is maintained.

Acknowledgment

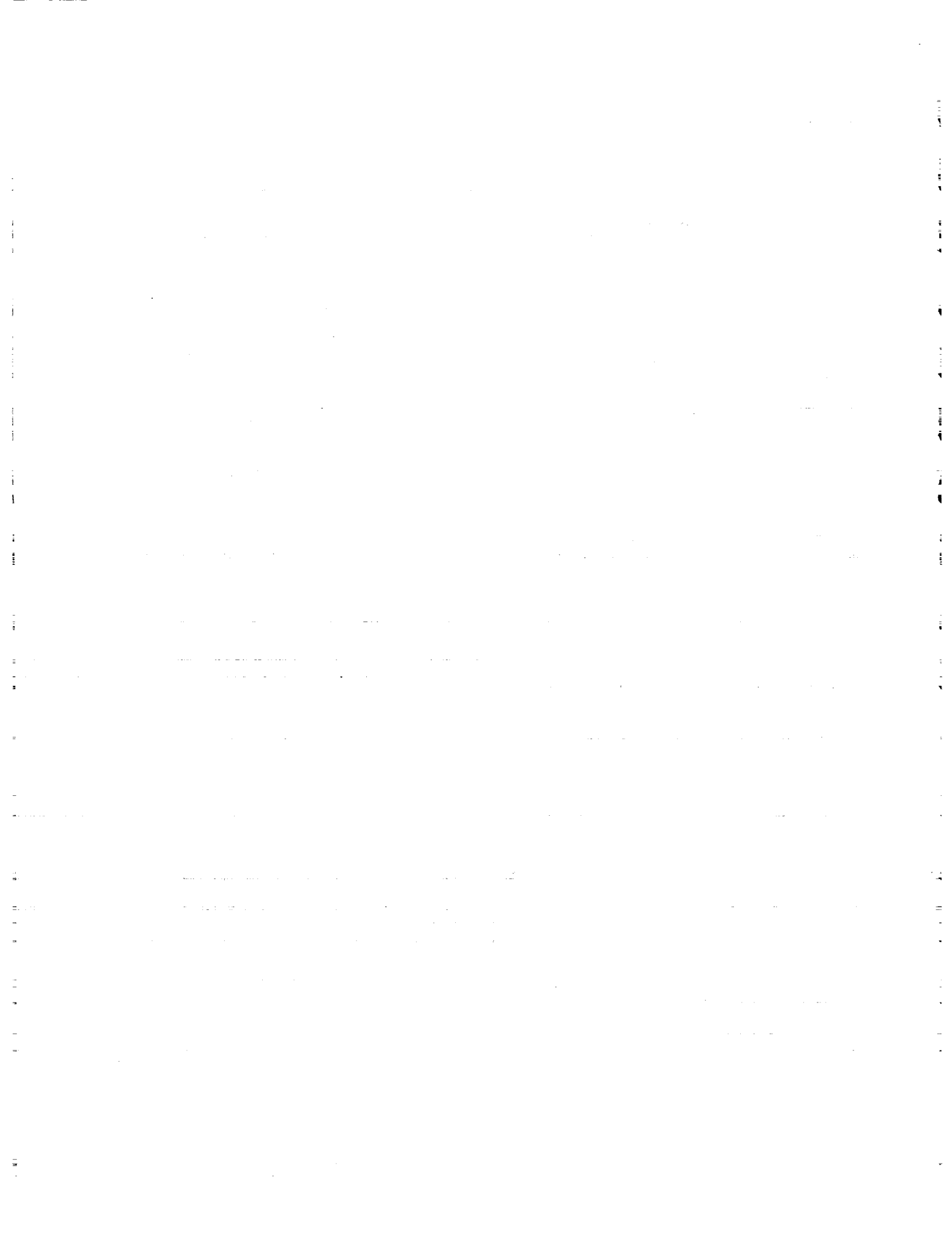
This research work is supported under Grants No. NAG-1-994 and NAG-1-648 by the NASA Langley Research Center. This paper is based on several previously published papers by the author and his Graduate Research Assistants; Mr. Steven J. Massey, Mr. Essam F. Sheta and Ms. Margaret Menzies. The author would like to recognize the computational resources provided by the NAS facilities at Ames Research Center and the NASA Langley Research Center.

References

1. Sellers, W. L. III, Meyers, J. F. and Hepner, T. E., "LDV Survey Over a Fighter Model at Moderate to High Angle of Attack," SAE Paper 88-1448, 1988.
2. Erickson, G. E., Hall, R. M., Banks, D. W., Del Frate, J. H., Shreiner, J. A., Hanley, R. J. and Pulley, C. T., "Experimental Investigation of the F/A-18 Vortex Flows at Subsonic Through Transonic Speeds," AIAA 89-2222, 1989.



3. Wentz, W. H., "Vortex-Fin Interaction on a Fighter Aircraft," AIAA 87-2474, AIAA Fifth Applied Aerodynamics Conference, Monterey, CA August 1987.
4. Lee, B. and Brown, D., "Wind Tunnel Studies of F/A-18 Tail Buffet," AIAA 90-1432, 1990.
5. Cole, S. R., Moss, S. W. and Dogget, R. V., Jr., "Some Buffet Response Characteristics of a Twin-Vertical-Tail Configuration," NASA TM-102749, October 1990.
6. Washburn, A. E., Jenkins, L. N. and Ferman, M. A., "Experimental Investigation of Vortex-Fin Interaction," AIAA 93-0050, AIAA 31st ASM, Reno, NV, January 1993.
7. Bean, D. E. and Lee, B. H. K., "Correlation of Wind Tunnel and Flight Test Data for F/A-18 Vertical Tail Buffet," AIAA 94-1800-CP, 1994.
8. Meyn, L. A. and James, K. D., "Full Scale Wind Tunnel Studies of F/A-18 Tail Buffet," AIAA 93-3519-CP, AIAA Applied Aerodynamics Conference, Monterey, CA, August 9-11, 1993.
9. Pettit, C. L., Brown, D. L. and Pendleton, E., "Wind Tunnel Test of Full-Scale F/A-18 Twin Tail Buffet: A summary of pressure and Response Measurements," AIAA 94-3476-CP, AIAA Applied Aerodynamics Conference, Colorado Springs, CO, June 1994, pp. 207-218.
10. Kandil, O. A., Kandil, H. A. and Massey, S. J., "Simulation of Tail Buffet Using Delta Wing-Vertical Tail Configuration," AIAA 93-3688-CP, AIAA Atmospheric Flight Mechanics Conference, Monterey, CA August 1993, pp. 566-577.
11. Kandil, O. A., Massey, S. J., and Kandil, H. A., "Computations of Vortex-Breakdown Induced Tail Buffet Undergoing Bending and Torsional Vibrations," AIAA 94-1428-CP, AIAA/ASME/ASCE/ASC Structural, Structural Dynamics and Material Conference, SC April 1994, pp. 977-993.
12. Kandil, O. A., Massey, S. J. and Sheta, E. F., "Structural Dynamics/CFD Interaction for computation of Vertical Tail Buffet," International Forum on Aeroelasticity and Structural Dynamics, Royal Aeronautical Society, Manchester, U.K., June 26-28, 1995, pp. 52.1-52.14. Also published in Royal Aeronautical Journal, August/September 1996, pp. 297-303.
13. Kandil, O. A., Sheta, E. F. and Massey, S. J., "Buffet Responses of a Vertical Tail in Vortex Breakdown Flows," AIAA 95-3464-CP, AIAA Atmospheric Flight Mechanics Conference, Baltimore, MD, August 7-9, 1995, pp. 345-360.
14. Kandil, O. A., Sheta, E. F. and Massey, S. J., "Twin Tail/Delta Wing Configuration Buffet Due to Unsteady Vortex Breakdown Flow," AIAA 96-2517-CP, 14th AIAA Applied Aerodynamics Conference, New Orleans, LA, June 18-20, 1996, pp. 1136-1150.
15. Nguyen, L. E., Yip, L. P., and Chambers, J. R., "Self Induced wing Rock of Slender Delta Wings," AIAA Paper No. 81-1883, August, 1981.
16. Ericsson, L. E., "Third Fluid Mechanics of Slender wing Rick," *Journal of Aircraft*, Vol. 21, No. 5, 1984, pp. 322-328.
17. Arena, A. S., *An Experimental and Computational Investigation of Slender Wings Undergoing Wing Rock*, Ph.D. Dissertation, University of Notre Dame, April, 1992.
18. Ng, T. T., Malcolm, G. N., and Lewis, L. C., "Experimental Study of Vortex Flows over Delta Wings in Wing-Rock Motion," *Journal of Aircraft*, Vol. 29, No. 4, July-August, 1992.
19. Malcolm, G. N., Ng, T. T., Lewis, L., and Murri, D. G., "Development of Non-Conventional Control Methods for High Angle of Attack Flight Usingortex Manipulation," AIAA Paper No. 89-2192, July, 1989.
20. Walton, J. and Katz, J., "Application of Leading-Edge Vortex Manipulations to Reduce Wing Rock Amplitudes," *Journal of Aircraft*, Vol. 30, No. 4, July-August 1993.
21. Ng, T. T., Scaff, T., and Kountz, J., "Effect of Leeward Flow Divider on the Wing Rock of a Delta Wing," *Journal of Aircraft*, Vol. 31, No. 6, November-December, 1994.
22. Wong, G. S., Rock, S. M., Wood, N. J., and Roberts, L., "Active Control of Wing Rock Using Tangential Leading-Edge Blowing," *Journal of Aircraft*, Vol. 31, No. 3, May-June, 1994.
23. Konstantinopoulos, P., Mook, D. T., and Nayfeh, A. H., "Subsonic Wing Rock of Slender Delta wings," *Journal of Aircraft*, Vol. 22, No. 3, March, 1985.
24. Nayfeh, A. H., Elzebe, J. M., and Mook, D. T., "Analytical Study of the Subsonic Wing-Rock Phenomenon for Slender Delta Wings," *Journal of Aircraft*, Vol. 26, No. 9, September, 1989.
25. Chaderjian, N. M. and Schiff, L. B., "Navier-Stokes Prediction of Large-Amplitude Forced and Free-to Roll Delta-Wing Oscillations," AIAA Paper No. 94-1884-CP, 1994.
26. Kandil, O. A. and Salman, A. A., "Effects of Leading-Edge Flap Oscillation of Unsteady Delta Wing Flow and Rock Control," AIAA Paper No. 91-1796, June, 1991.
27. Kandil, O. A. and Salman, A. A., "Prediction and Control of slender Wing Rock," ICAS 92-4.7.2, 1992, pp. 1430-1441.
28. Kandil, O. A. and Salman, A. A., "Recent Advances in Unsteady Computations and Applications of Vortex Dominated Flows," 4th International Symposium on Computational Fluid Dynamics, Davis, CA, September, 1991, pp. 570-575.
29. Salman, A. A., *Unsteady Euler and Navier-Stokes Computations Around Oscillating Delta Wing including dynamics*, Ph.D. Dissertation, Old Dominion University, April, 1992.
30. Lee-Rausch, E. M. and Batina, J. T., "Conical Euler Analysis and Active Roll Suppression for Unsteady Vortical Flows about Rolling Delta Wings," NASA Technical Paper 3259, 1993.
31. Menzies, M. A. and Kandil, O. A., "Natural Rolling Responses of a Delta wing in Transonic and Subsonic Flows," AIAA-96-3391-CP AIAA Atmospheric Flight Mechanics Conference, San Diego, CA, July 29-31, 1996, pp. 246-254.
32. Menzies, M. A., Kandil, O. A., and Kandil, H. A., "Forced Rolling Oscillation of a 65°-Delta Wing in Transonic Vortex-Breakdown Flow," AIAA Paper No. 95-1771-CP, June, 1995.



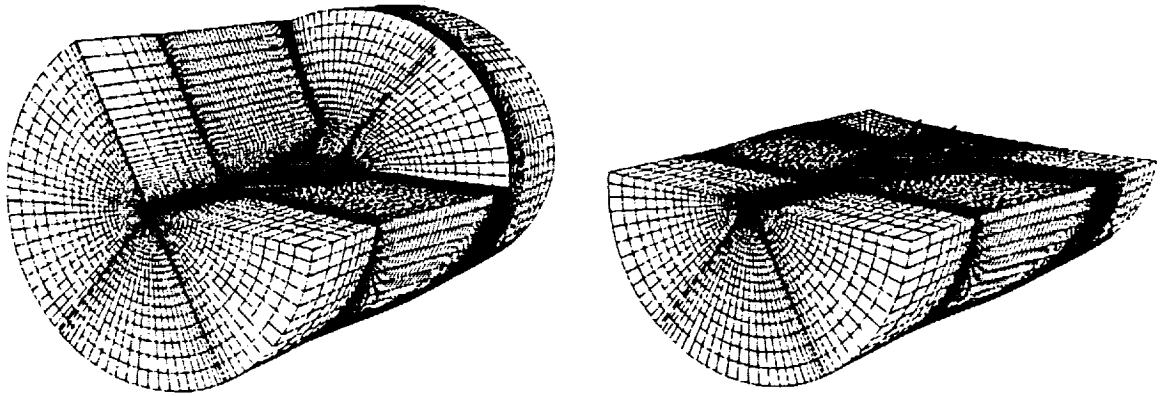


Figure 1. Three-dimensional grid topology of the twin tail-delta wing configuration (Midspan).

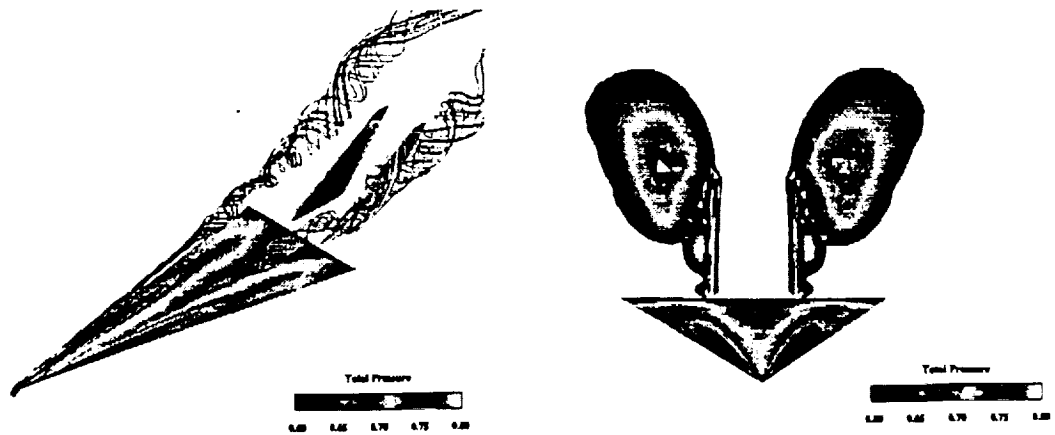


Figure 2. Three-dimensional and front views showing the total pressure on the surfaces, and the vortex-core streamlines. Initial conditions (Inboard position).

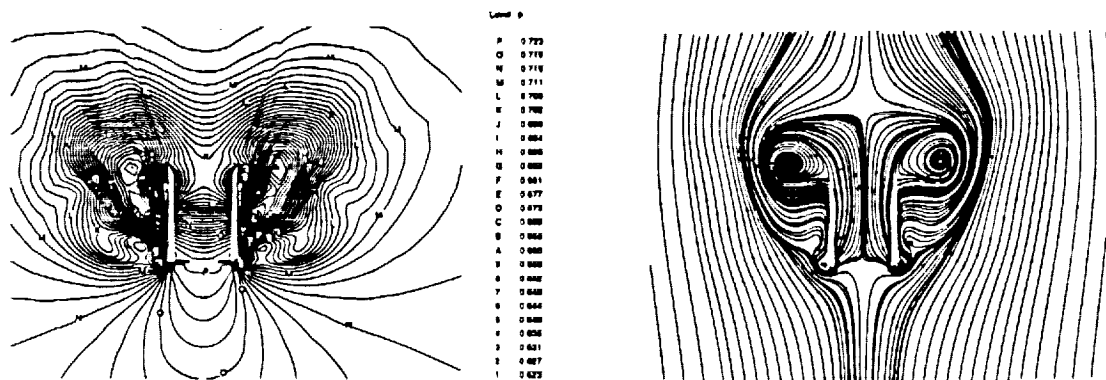


Figure 3. Initial conditions for static pressure and instantaneous streamlines in a cross-flow plane, $x = 1.096$ (Inboard position).

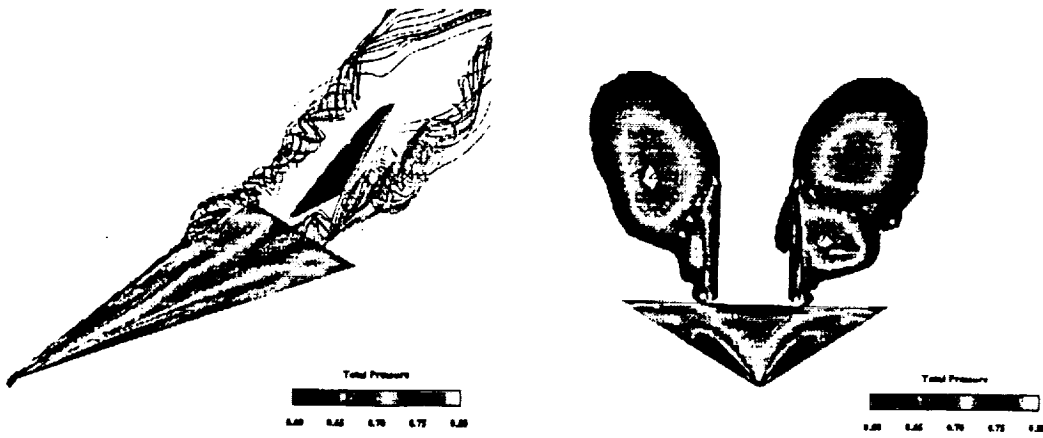


Figure 4. Three-dimensional and front views showing the total pressure on the surfaces, and the vortex-core streamlines. Uncoupled case after $it = 9,600$ (Inboard position).

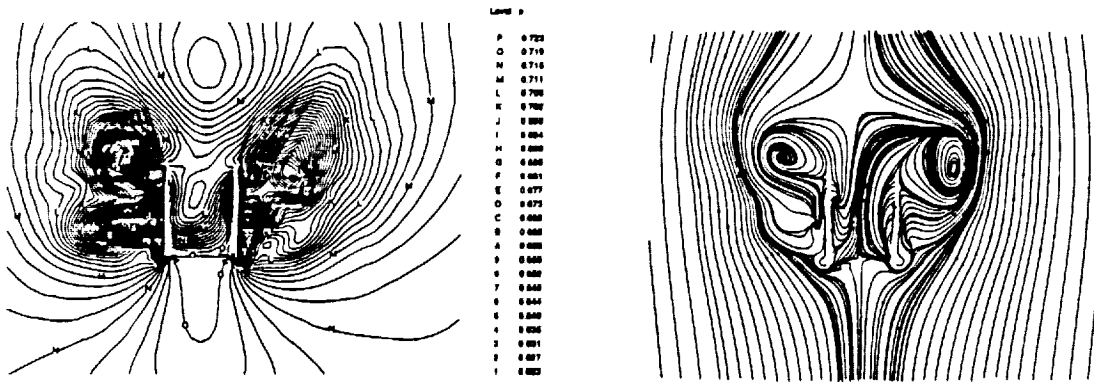


Figure 5. Snap shots of static pressure and instantaneous streamlines in a cross-flow plane, $x = 1.096$. Uncoupled case after $it = 9,600$ (Inboard position).

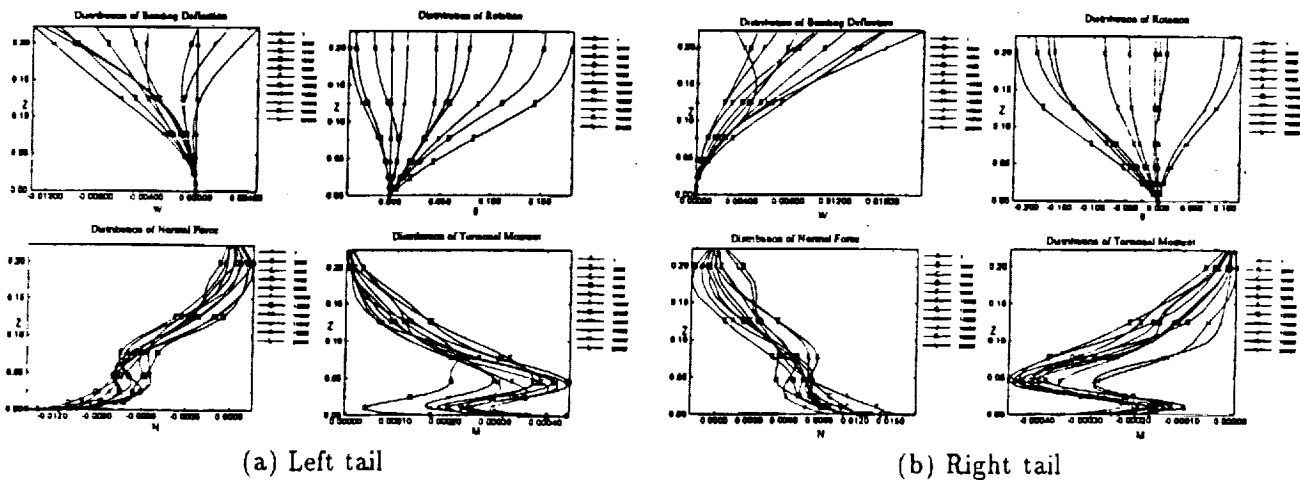


Figure 6. Distribution of the deflection and load responses for an uncoupled bending-torsion case. $M_\infty = 0.3$, $\alpha = 30^\circ$, $R_p = 1.25 \times 10^6$, (Inboard position).

1. The first part of the document discusses the importance of maintaining accurate records of all transactions and the role of the accounting department in ensuring the integrity of the financial statements.

2. The second part of the document outlines the various methods used to collect and analyze data, including the use of statistical software and the importance of sample size and representativeness.

3. The third part of the document describes the various techniques used to interpret the results of the data analysis, including the use of regression analysis and the importance of understanding the limitations of the data.

4. The fourth part of the document discusses the various factors that can influence the results of the data analysis, including the quality of the data and the skill of the analyst.

5. The fifth part of the document describes the various methods used to communicate the results of the data analysis, including the use of written reports and the importance of clear and concise communication.

6. The sixth part of the document discusses the various factors that can influence the results of the data analysis, including the quality of the data and the skill of the analyst.

7. The seventh part of the document describes the various methods used to communicate the results of the data analysis, including the use of written reports and the importance of clear and concise communication.

8. The eighth part of the document discusses the various factors that can influence the results of the data analysis, including the quality of the data and the skill of the analyst.

9. The ninth part of the document describes the various methods used to communicate the results of the data analysis, including the use of written reports and the importance of clear and concise communication.

10. The tenth part of the document discusses the various factors that can influence the results of the data analysis, including the quality of the data and the skill of the analyst.

11. The eleventh part of the document describes the various methods used to communicate the results of the data analysis, including the use of written reports and the importance of clear and concise communication.

12. The twelfth part of the document discusses the various factors that can influence the results of the data analysis, including the quality of the data and the skill of the analyst.

13. The thirteenth part of the document describes the various methods used to communicate the results of the data analysis, including the use of written reports and the importance of clear and concise communication.

14. The fourteenth part of the document discusses the various factors that can influence the results of the data analysis, including the quality of the data and the skill of the analyst.

15. The fifteenth part of the document describes the various methods used to communicate the results of the data analysis, including the use of written reports and the importance of clear and concise communication.

16. The sixteenth part of the document discusses the various factors that can influence the results of the data analysis, including the quality of the data and the skill of the analyst.

17. The seventeenth part of the document describes the various methods used to communicate the results of the data analysis, including the use of written reports and the importance of clear and concise communication.

18. The eighteenth part of the document discusses the various factors that can influence the results of the data analysis, including the quality of the data and the skill of the analyst.

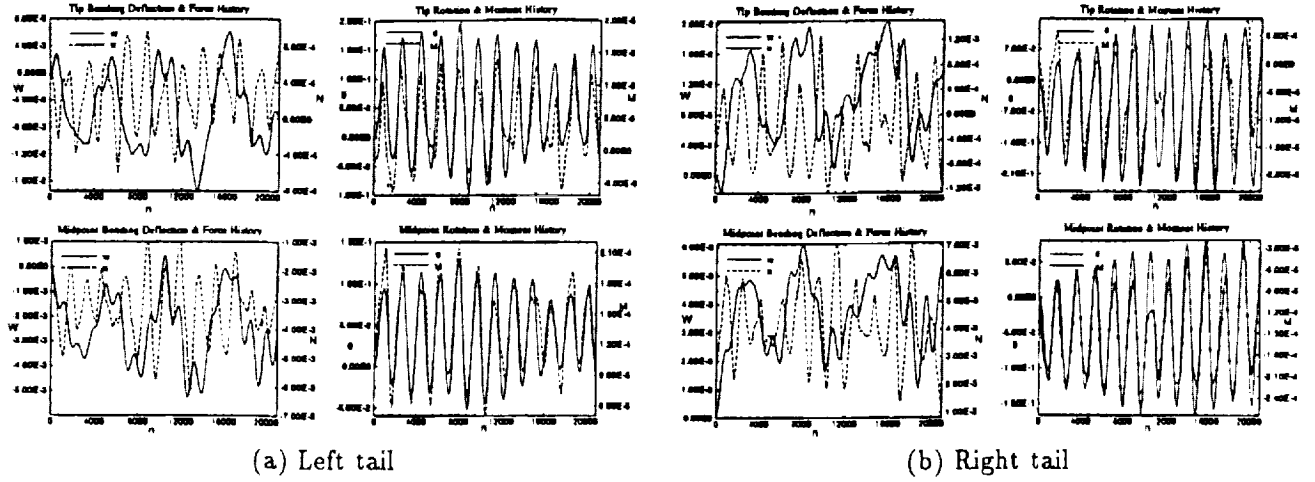


Figure 7. History of the deflection and load responses for an uncoupled bending-torsion case. $M_\infty = 0.3, \alpha = 30^\circ, R_\epsilon = 1.25 \times 10^6$, (Inboard position).

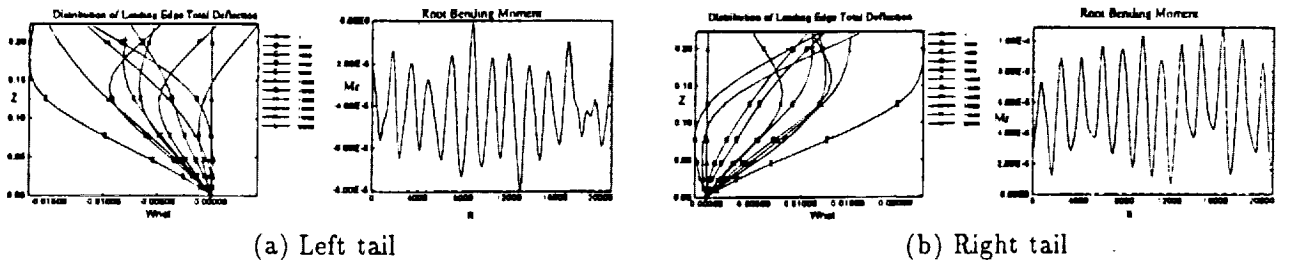


Figure 8. Total structural deflections and root bending moment for an uncoupled bending-torsion case $M_\infty = 0.3, \alpha = 30^\circ, R_\epsilon = 1.25 \times 10^6$, (Inboard position).

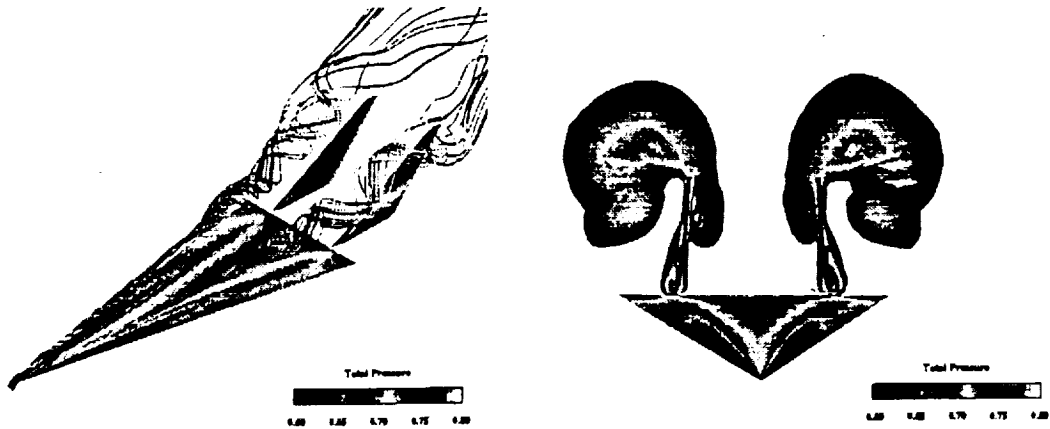


Figure 9. Three-dimensional and front views showing the total pressure on the surfaces, and the vortex-core streamlines. Initial conditions (Midspan position).



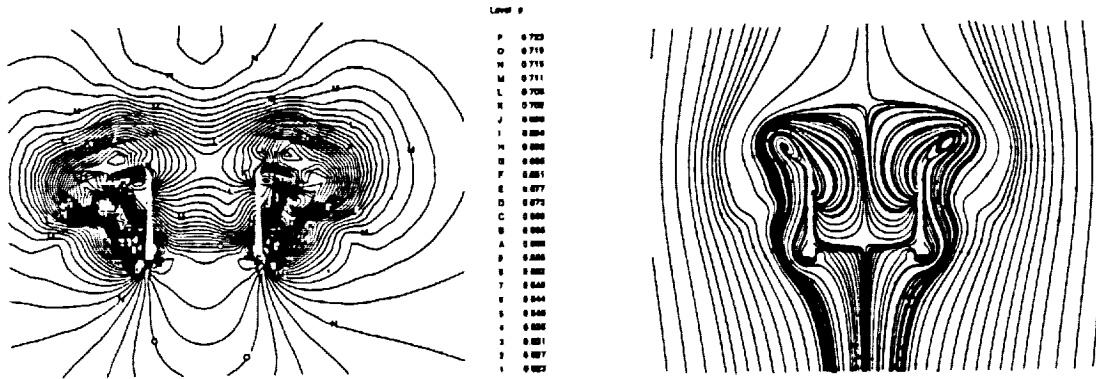


Figure 10. Initial conditions for static pressure and instantaneous streamlines in a cross-flow plane, $x = 1.096$ (Midspan position).

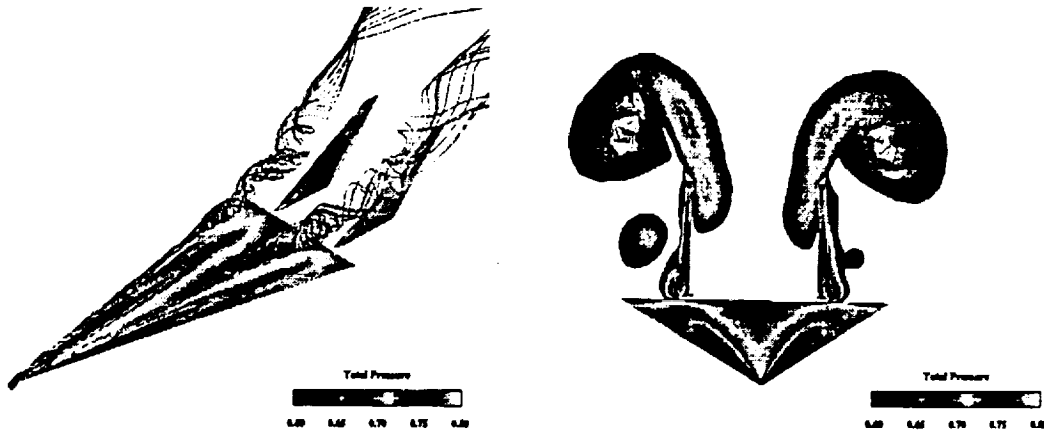


Figure 11. Three-dimensional and front views showing the total pressure on the surfaces, and the vortex-core streamlines. Uncoupled case after $it = 9,600$ (Midspan position).

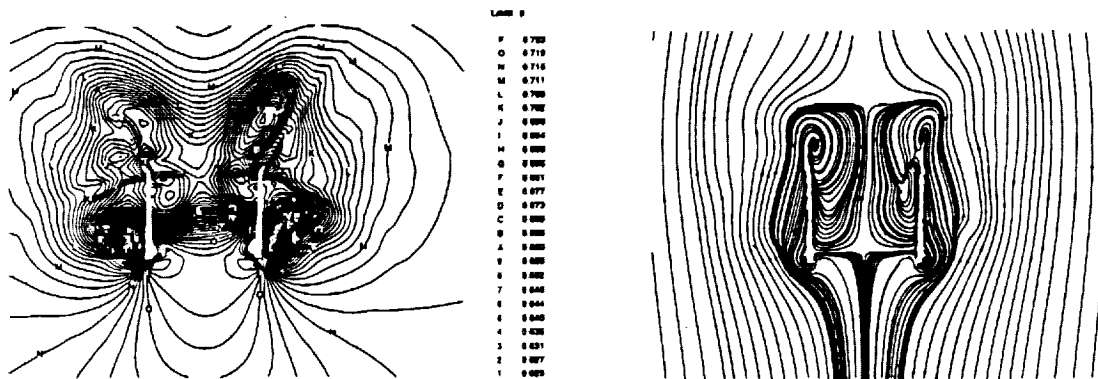
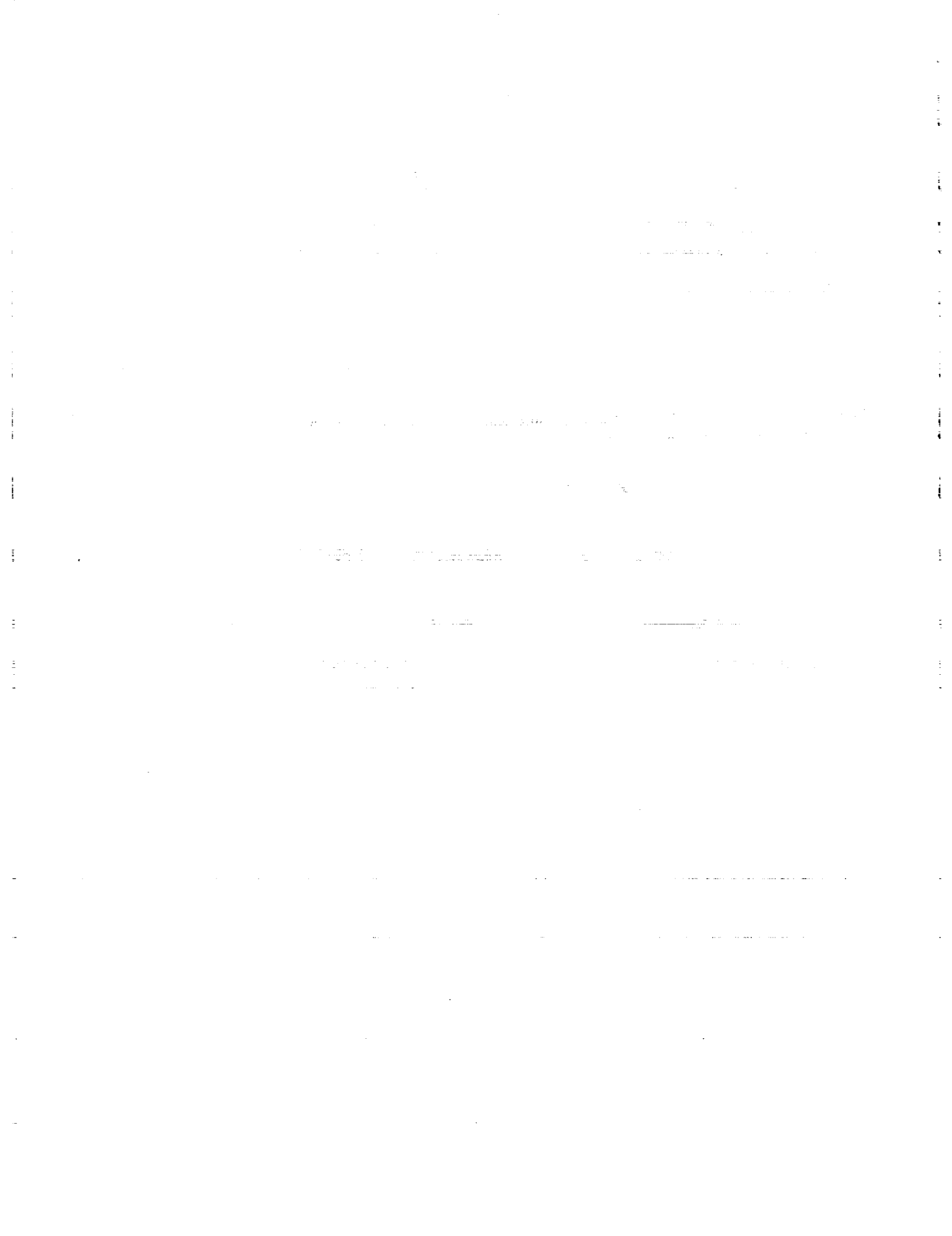


Figure 12. Snap shots of static pressure and instantaneous streamlines in a cross-flow plane, $x = 1.096$. Uncoupled case after $it = 9,600$ (Midspan position).



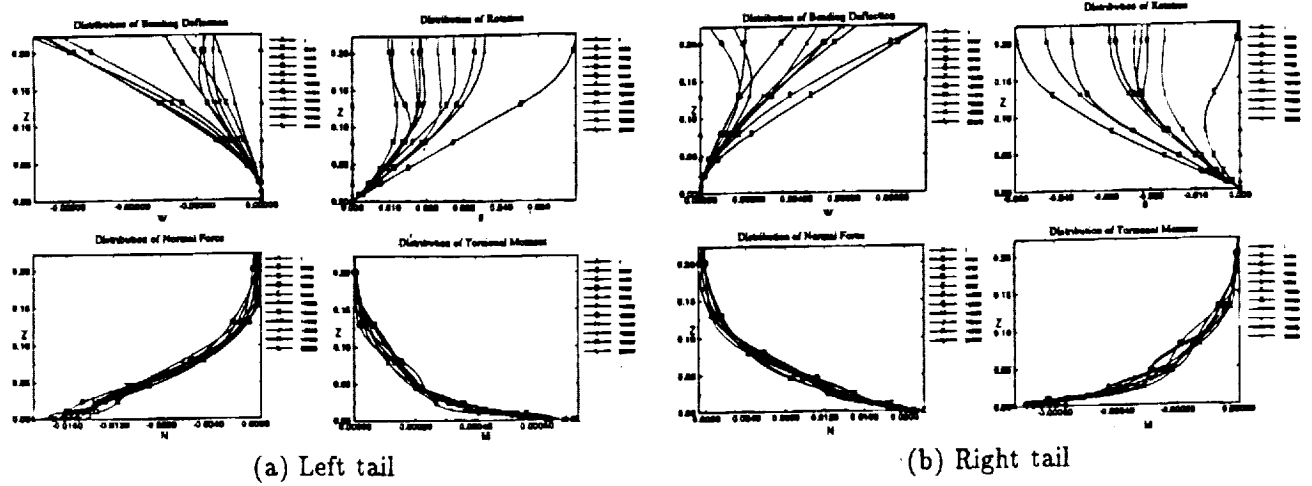


Figure 13. Distribution of the deflection and load responses for an uncoupled bending-torsion case. $M_\infty = 0.3, \alpha = 30^\circ, R_e = 1.25 \times 10^6$, (Midspan position).

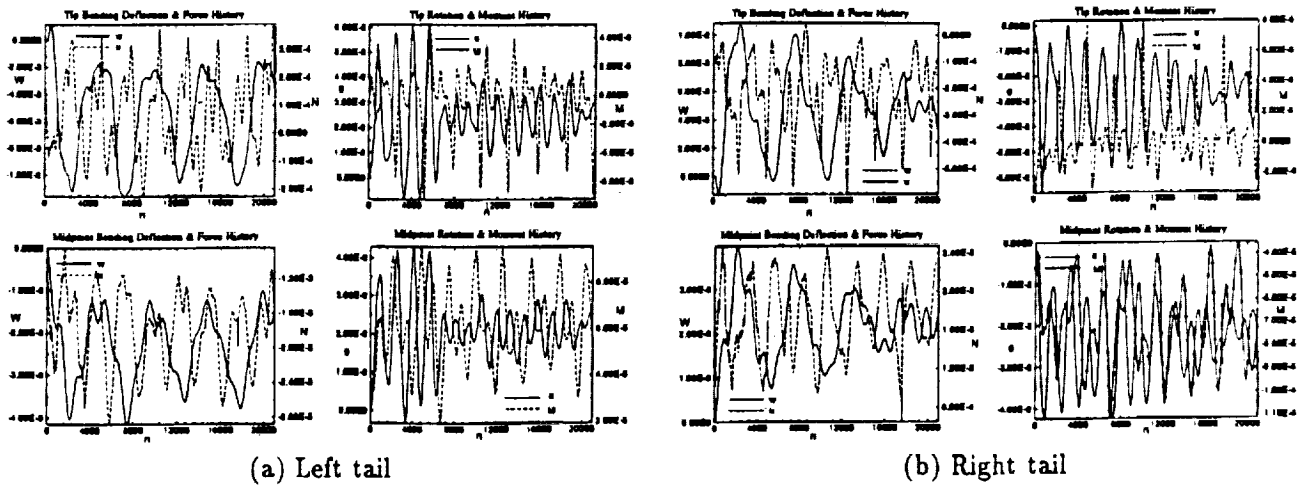


Figure 14. History of the deflection and load responses for an uncoupled bending-torsion case. $M_\infty = 0.3, \alpha = 30^\circ, R_e = 1.25 \times 10^6$, (Midspan position).

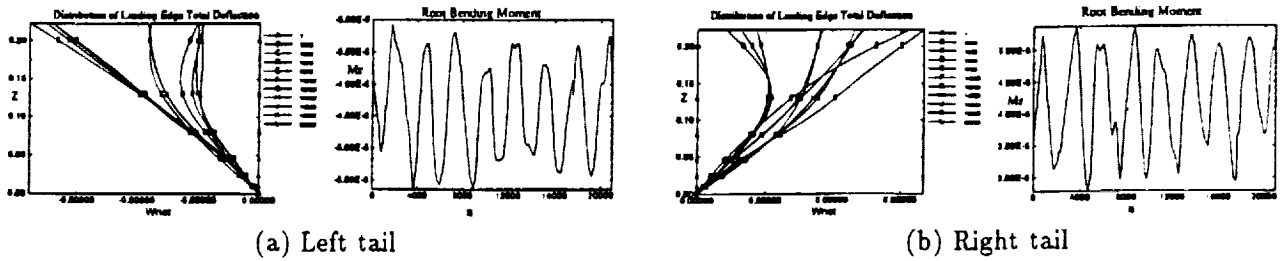


Figure 15. Total structural deflections and root bending moment for an uncoupled bending-torsion case. $M_\infty = 0.3, \alpha = 30^\circ, R_e = 1.25 \times 10^6$, (Midspan position).

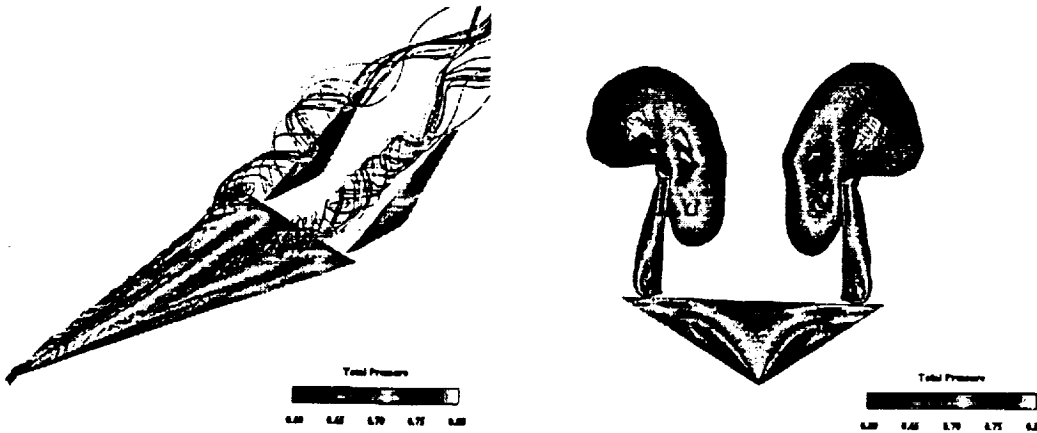


Figure 16. Three-dimensional and front views showing the total pressure on the surfaces, and the vortex-core streamlines. Uncoupled case after $it = 9,600$ (Outboard position).

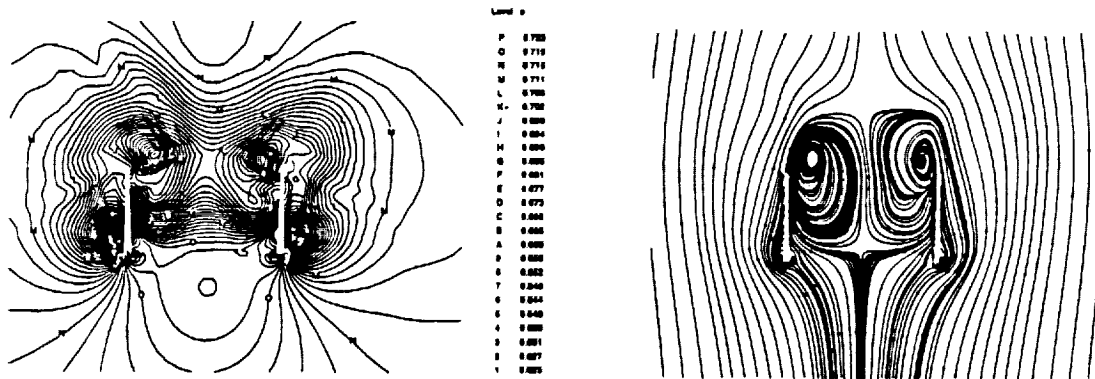
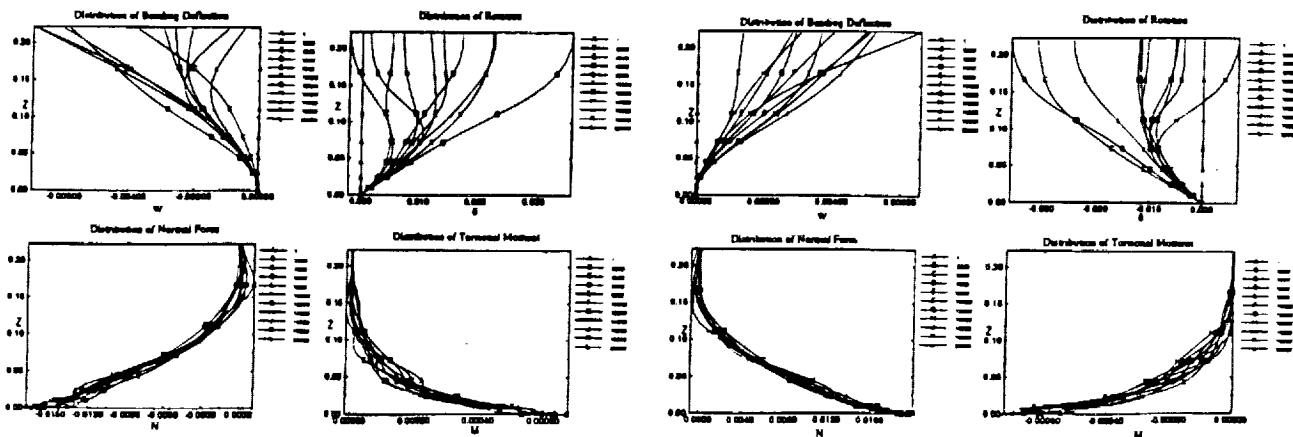


Figure 17. Snap shots of static pressure and instantaneous streamlines in a cross-flow plane, $x = 1.096$. Uncoupled case after $it = 9,600$ (Outboard position).



(a) Left tail

(b) Right tail

Figure 18. Distribution of the deflection and load responses for an uncoupled bending-torsion case. $M_\infty = 0.3$, $\alpha = 30^\circ$, $Re = 1.25 \times 10^6$, (Outboard position).

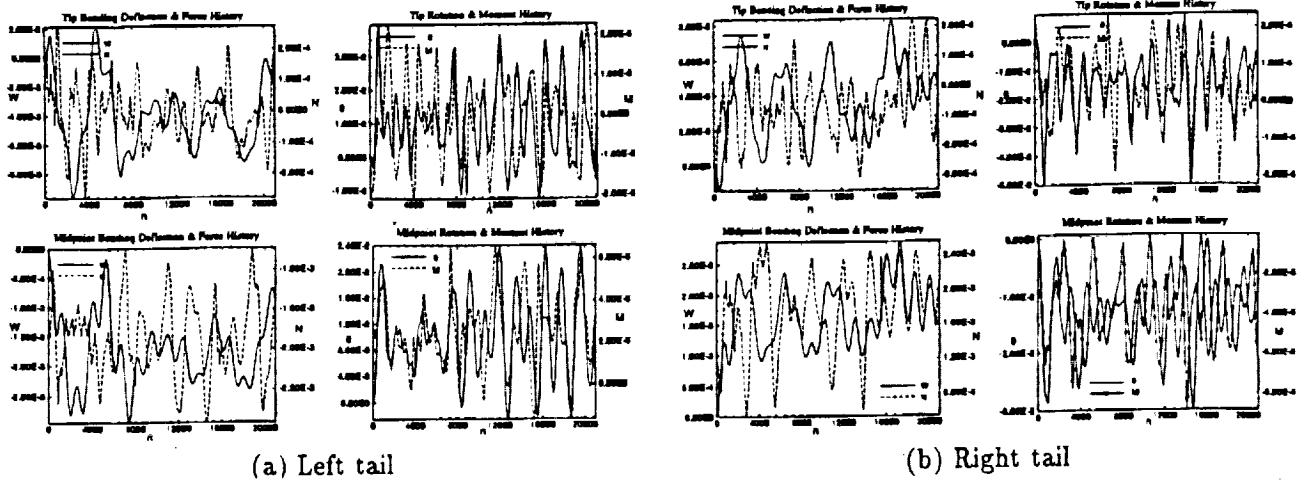


Figure 19. History of the deflection and load responses for an uncoupled bending-torsion case. $M_\infty = 0.3, \alpha = 30^\circ, R_e = 1.25 \times 10^6$, (Outboard position).

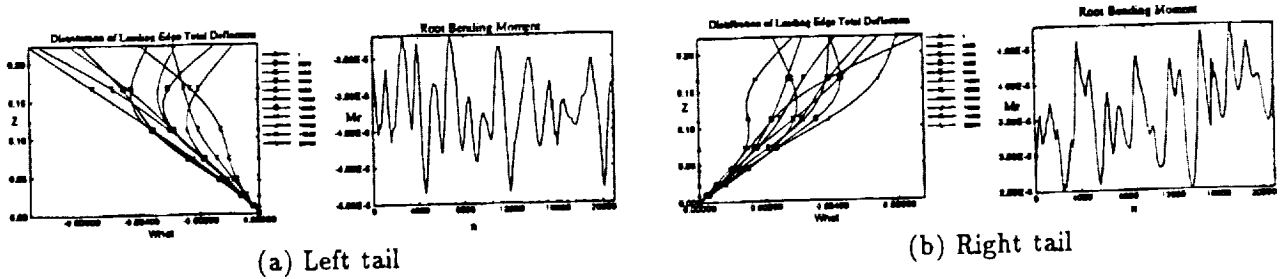


Figure 20. Total structural deflections and root bending moment for an uncoupled bending-torsion case. $M_\infty = 0.3, \alpha = 30^\circ, R_e = 1.25 \times 10^6$, (Outboard position).

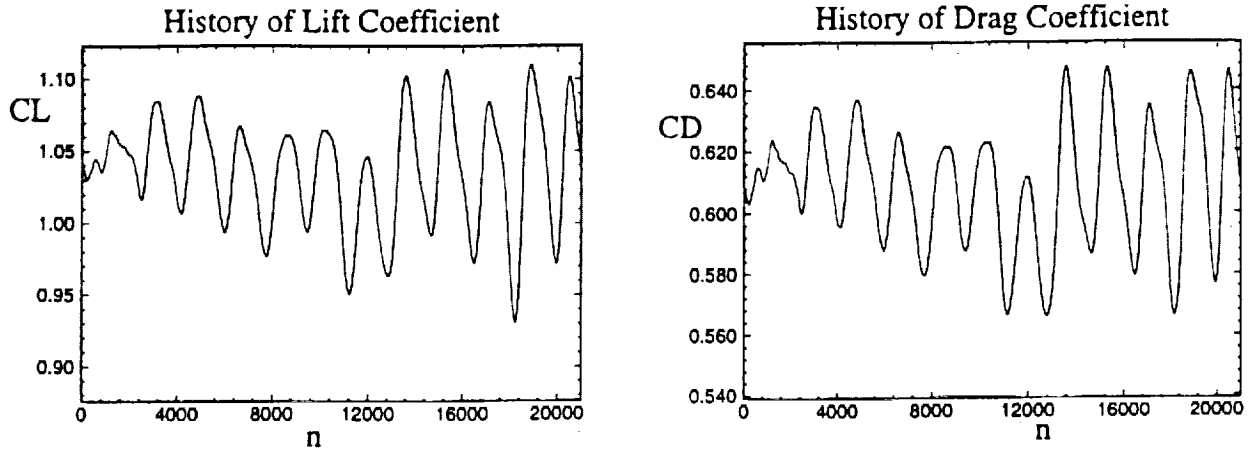


Figure 21. History of the forces on the wing/twin-tail configuration. $M_\infty = 0.3, \alpha = 30^\circ, R_e = 1.25 \times 10^6$, (Inboard position).

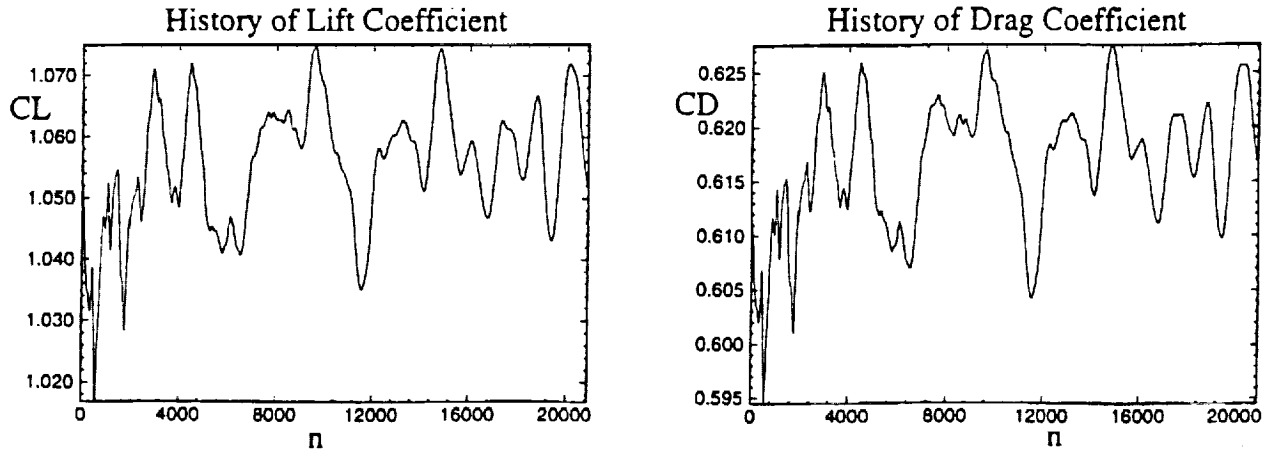


Figure 22. History of the forces on the wing/twin-tail configuration. $M_\infty = 0.3$, $\alpha = 30^\circ$, $R_t = 1.25 \times 10^6$, (Midspan position).

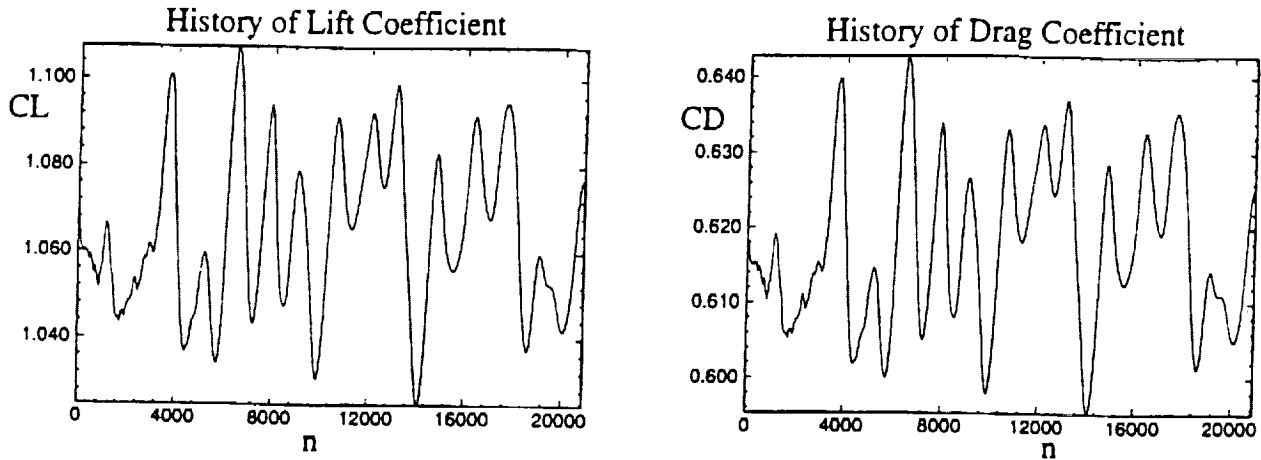


Figure 23. History of the forces on the wing/twin-tail configuration. $M_\infty = 0.3$, $\alpha = 30^\circ$, $R_t = 1.25 \times 10^6$, (Outboard position).

Transonic Flow-Initial Conditions

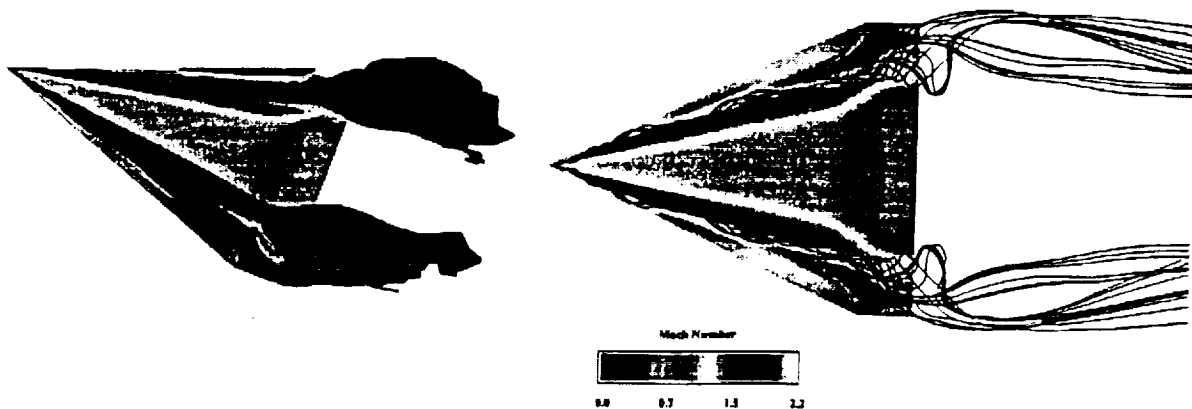


Figure 24. Mach Contours near the Wing Surface with Surfaces of Constant Entropy ($s = 0.5$) and Instantaneous Streamlines; $\alpha = 20.0^\circ$, $\theta = 0.0^\circ$.

Transonic Flow-Divergent Oscillations

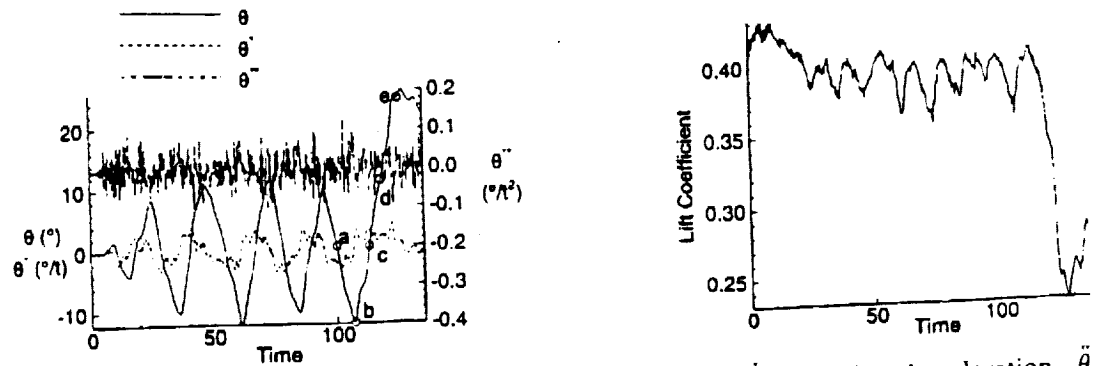


Figure 25. Time History of Roll Angle, θ , Angular Velocity, $\dot{\theta}$, Angular Acceleration, $\ddot{\theta}$, and Lift Coefficient; $M_\infty = 0.85$, $R_e = 3.23 \times 10^6$, $\alpha = 20.0^\circ$, $\theta_{ic} = 0.0^\circ$, $\dot{\theta}_{ic} = 0.5336^\circ/t$ (points of interest annotated).

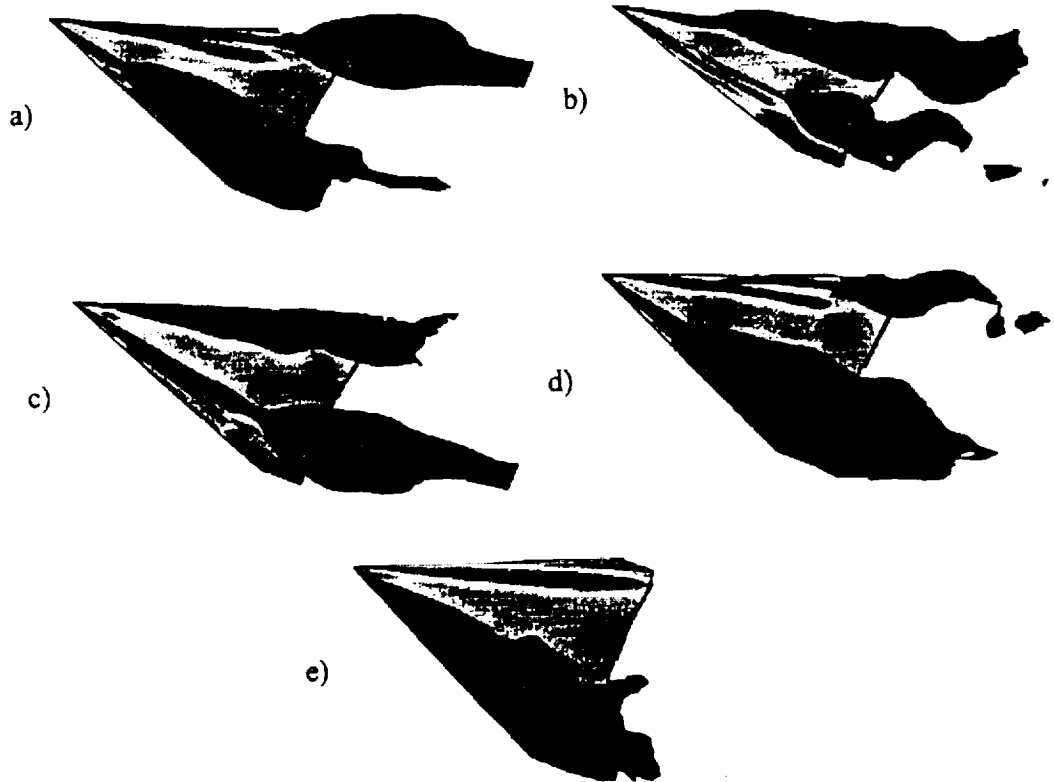


Figure 26. Snapshots of the Mach Contours near the Wing Surface with Surfaces of Constant Entropy ($s = 0.5$) at Points of Interest at a) $\theta = -0.47^\circ$, b) $\theta = -12.10^\circ$, c) $\theta = 0.44^\circ$, d) $\theta = 11.08^\circ$, e) $\theta = 24.27^\circ$.



Subsonic Flow-Damped Oscillations

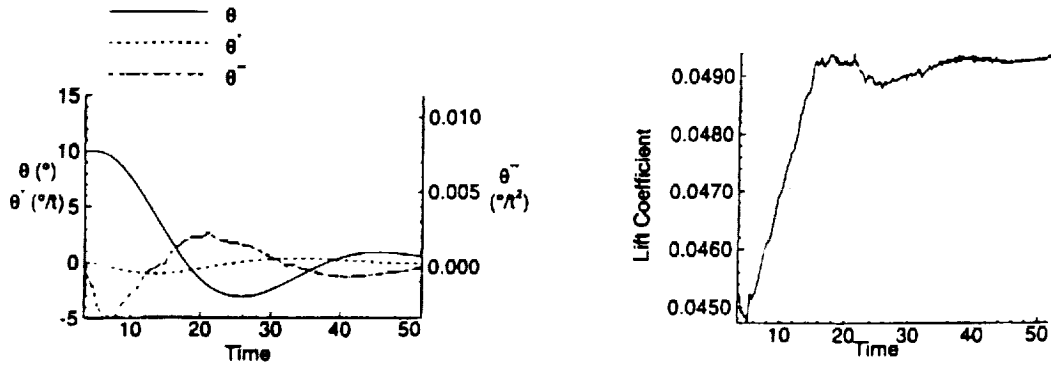


Figure 27. Time History of Roll Angle, θ , Angular Velocity, $\dot{\theta}$, Angular Acceleration, $\ddot{\theta}$ and Lift Coefficient; $M_\infty = 0.1$, $R_e = 0.4 \times 10^6$, $\alpha = 20.0^\circ$, $\theta_{ic} = 10.0^\circ$, $\dot{\theta}_{ic} = 0.0^\circ/t$.

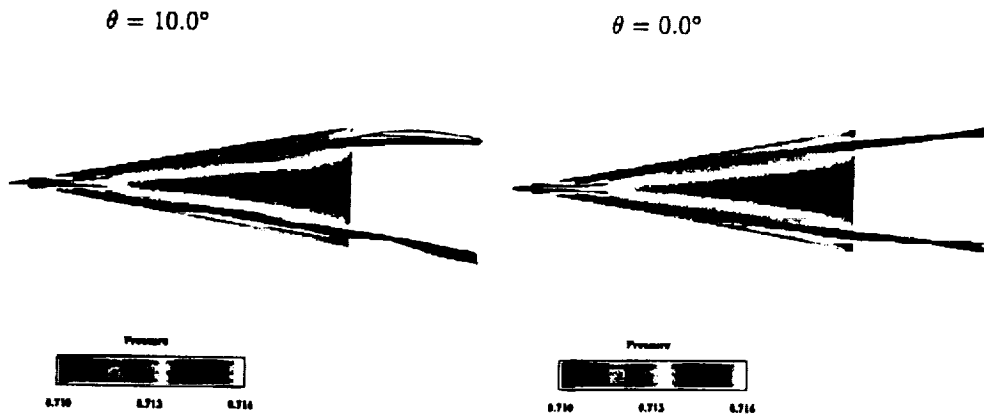


Figure 28. Comparison of Mach number Contours and Instantaneous Streamlines of Initial Conditions ($\theta = 10.0^\circ$) and Steady State Response ($\theta = 0.0^\circ$).

Subsonic Flow-Self-Sustained Limit-Cycle Oscillations

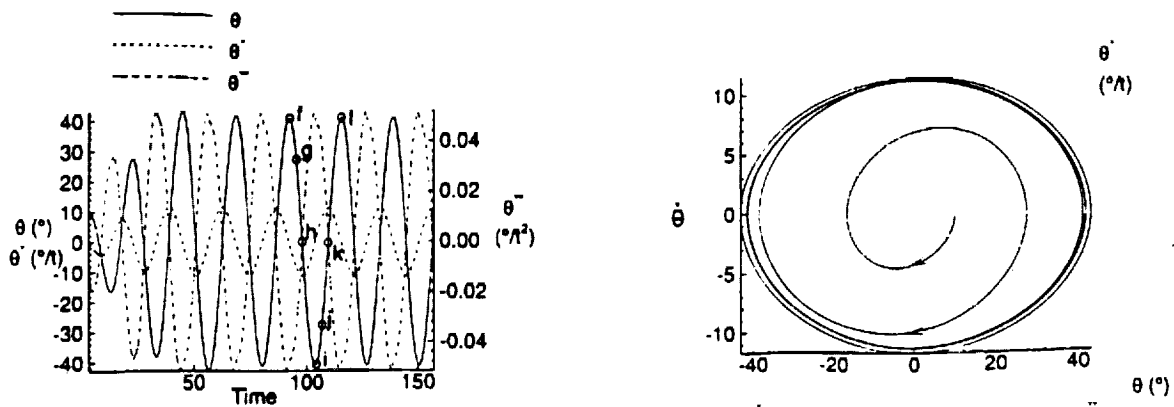


Figure 29. Time History of Roll Angle, θ , Angular Velocity, $\dot{\theta}$, Angular Acceleration, $\ddot{\theta}$ and Phase of Angular Velocity, $\dot{\theta}$; $M_\infty = 0.1$, $R_e = 0.4 \times 10^6$, $\alpha = 30.0^\circ$, $\theta_{ic} = 10.0^\circ$, $\dot{\theta}_{ic} = 0.0^\circ/t$ (with points of interest annotated).

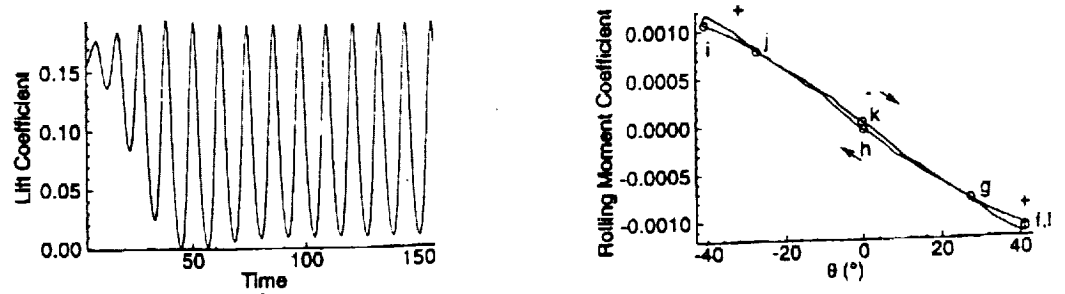


Figure 30. Time History of Lift Coefficient and Phase of Rolling Moment Coefficient indicating Energy Transfer Lobes. (with points of interest annotated).

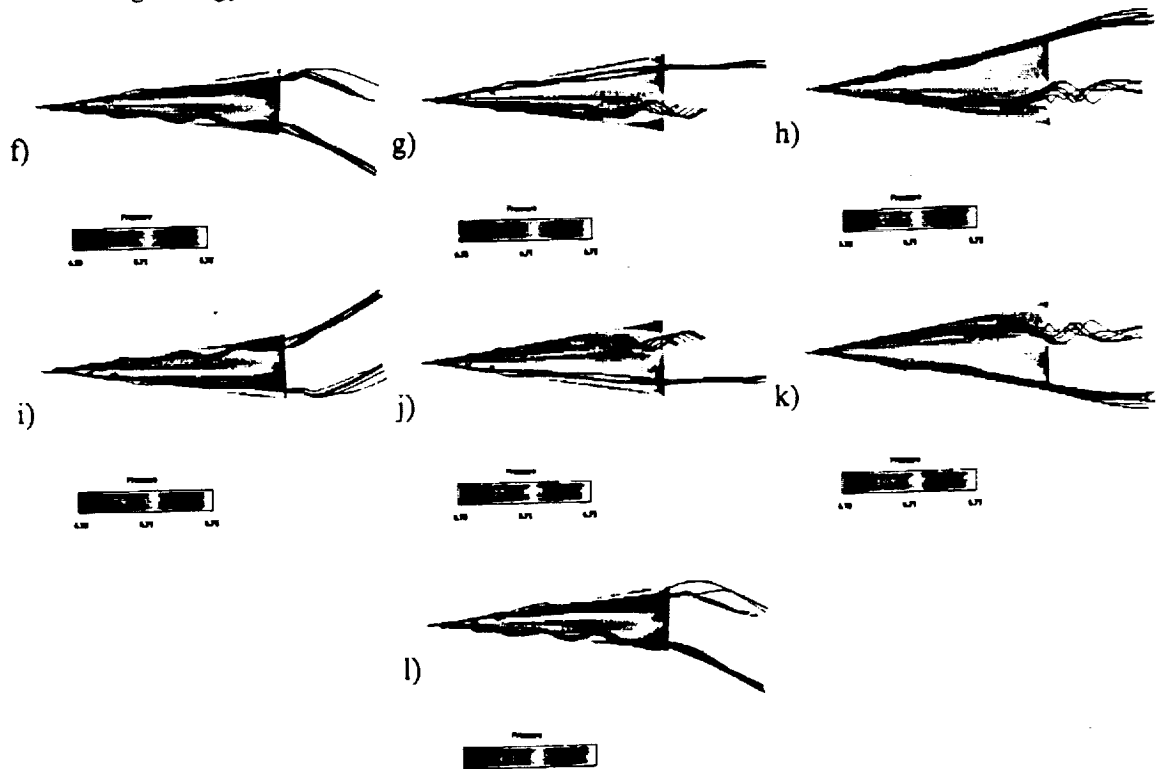


Figure 31. Snapshots of a Complete Cycle of Rolling Oscillation depicting the Total Pressure Contours at Points of Interest at f) $\theta = -41.1^\circ$, g) $\theta = -27.3^\circ$, h) $\theta = 0.0^\circ$, i) $\theta = 40.8^\circ$, j) $\theta = 27.5^\circ$, k) $\theta = 0.2^\circ$, l) $\theta = -41.2^\circ$.

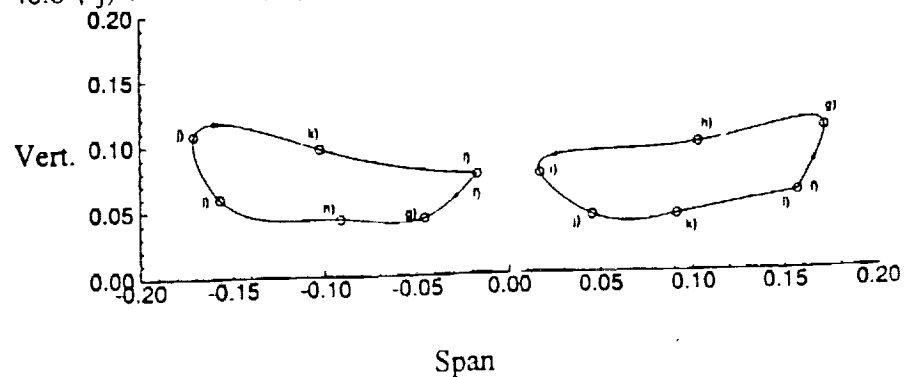


Figure 32. Plot of the Vortex Cores Positions at $x = 0.77$ at points of interest.

DEVELOPMENT OF A COUPLED FLUID/STRUCTURE
AEROELASTIC SOLVER WITH APPLICATIONS TO VORTEX
BREAKDOWN INDUCED TWIN TAIL BUFFETING

by

Steven J. Massey

B.S. May 1990, Virginia Polytechnic Institute & State University, Blacksburg, VA

M.S. May 1994, Old Dominion University, Norfolk, VA

A Dissertation Submitted to the Faculty of
Old Dominion University in Partial Fulfillment of the
Requirement for the Degree of

DOCTOR OF PHILOSOPHY

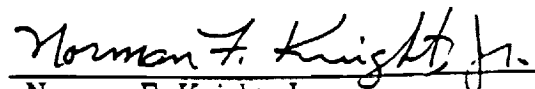
AEROSPACE ENGINEERING

OLD DOMINION UNIVERSITY

December 1997


Approved by:

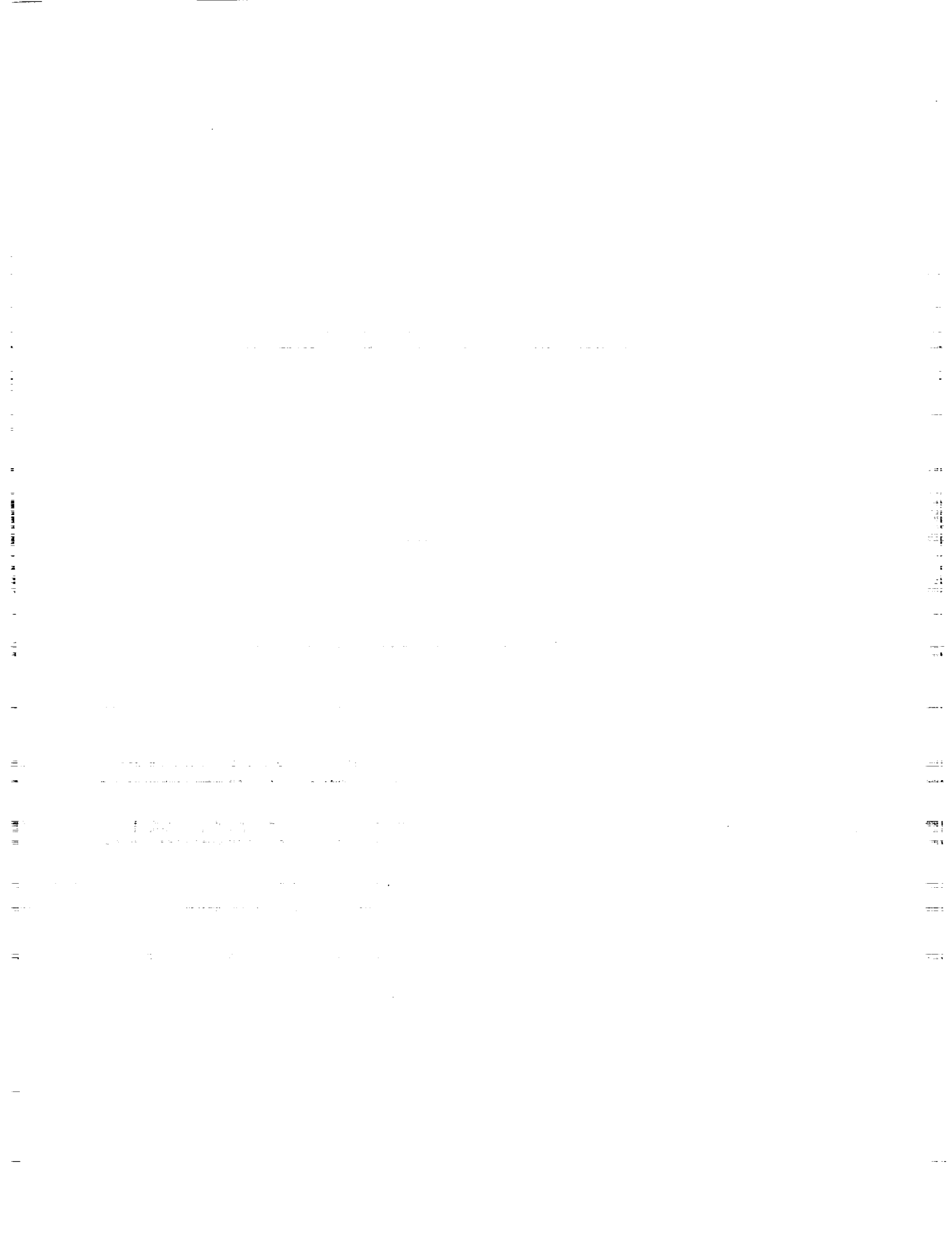

Osama A. Kandil (Director)


Norman F. Knight, Jr.


Colin P. Britcher


Robert Bennett (LaRC)


Woodrow Whitlow, Jr. (LaRC)



ABSTRACT

DEVELOPMENT OF A COUPLED FLUID/STRUCTURE AEROELASTIC SOLVER WITH APPLICATIONS TO VORTEX BREAKDOWN INDUCED TWIN TAIL BUFFETING

Steven J. Massey
Old Dominion University
Director: Dr. Osama A. Kandil

Simulation of tail buffet is studied for several delta wing-vertical tail configurations. Flow conditions are chosen such that the wing primary-vortex cores experience vortex breakdown and the resulting turbulent wake flow impinges on the vertical tail. The dimensions and material properties of the vertical tails are chosen such that the deflections are large enough to insure interaction with the flow, and the natural frequencies are high enough to facilitate a practical computational solution. This multi-disciplinary problem is solved sequentially for the fluid flow, the elastic deformations and the grid displacements. The flow is simulated by time accurately solving the laminar, unsteady, compressible, Navier-Stokes equations using an implicit, upwind, flux-difference splitting, finite volume scheme. The elastic vibrations of the tail are modeled by coupled bending and torsion beam equations. These equations are solved accurately in time using the Galerkin method and a five-stage, Runge-Kutta-Verner scheme. The grid for the fluid dynamics calculations is continuously deformed using interpolation functions to smoothly disperse the displacements throughout the computational domain. Tail buffet problems are solved for single tail cases, twin F/A-18 tail cases and twin highly swept generic tail cases. The use of an apex flap for buffet control is also computationally studied. The results demonstrate the effects of inertial structural coupling, Reynolds number, aft

fuselage geometry and spanwise tail location on the tail buffet loads and response. Favorable comparisons with experimental data indicate that the present aeroelastic method is well suited to providing qualitative insight into the tail buffet problem, as well as quantitative data for refined long duration simulations.
